Hydrate Forming Emulsion: A Rheological, Thermodynamic and Morphological Study

by

Genti Zylyftari

advisor: Jeffrey F. Morris

A Dissertation Submitted for the Degree of Doctor of Philosophy

Department of Chemical Engineering

The City College

of

The City University of New York

2014

ProQuest LLC.
789 East Eisenhower Parkway
P.O. Box 1346
Ann Arbor, MI 48106 - 1346

This manuscript has been read and accepted for the
Graduate Faculty in Engineering in satisfaction of the
dissertation requirement for the degree of Doctor of Philosophy.

Jeffrey F. Morris

Date	Chair of Examining Committee

Ardie D. Walser

Date	Executive Officer

Alexander Couzis / Professor / The City College of New York
Charles Maldarelli / Professor / The City College of New York
William J. Blanford / Assistant Professor / Queens College
Hariprasad J. Subramani / Flow Assurance Engineer / Chevron
Examination Committee

THE CITY COLLEGE OF NEW YORK

Abstract

Pipeline blockage by clathrate hydrate formation is a major problem encountered in the oil and gas industry. Hydrate induced plug formation causes product flow interruption, severe equipment damage, environmental pollution and personnel fatalities. In order to efficiently and economically prevent hydrate formation, understanding of the underlying physical principles leading to hydrate blockage is required. This work addresses correlation of rheological properties of cyclopentane hydrate-forming emulsions with thermodynamics, nucleation by ice and morphology. Cyclopentane, used as hydrate-former in the model emulsion under atmospheric conditions, forms the same natural gas hydrate structure found in the oil and gas industry.

The effect of aqueous phase salinity on density-matched 40% (v/v) hydrate-forming emulsion are reported in Chapter 2. Using micro-differential scanning calorimetry and rheometry, a correlation of the rheological properties to thermodynamic driving forces is obtained. The cyclopentane hydrate-brine system liquidus line is determined from the calorimetric study. Equilibrium temperature and thermodynamically-allowed conversion of water to hydrate are computed from the hydrate-brine phase diagram. Good agreement was found between the experiments and calculations by an established thermodynamic simulation tool. Rheological properties, including the viscosity evolution time, final viscosity and its shear rate dependence, and yield stress of the hydrate-forming emulsion are determined; the material viscosity increases markedly as hydrate forms and the mixture develops a yield stress. The viscosity evolution time is smaller at lower temperature, i.e., at higher subcooling relative to the hydrate equilibrium dissociation temperature. The final hydrate slurry exhibits shear thinning effects describable by the Ostwald-de Waele model, and displays very little hysteresis in the shear rate dependence. Maximum viscosity is attained when the thermodynamic water to hydrate conversion is 61-85% while the yield stress was found to be a maximum at about 80% conversion; this non-

monotonic rheological property dependence on the thermodynamically-allowed water to hydrate conversion demonstrates that both liquid (residual brine) and solid hydrate content are important to the mechanical properties of the network structure developed when hydrate is present.

In Chapter 3, the effects of heterogeneous nucleation of cyclopentane hydrate by ice on the morphological properties of hydrate formed on a single aqueous drop immersed in cyclopentane and the rheological properties of density-matched 40% (v/v) aqueous fraction hydrate-forming emulsions are reported. Experimental observations indicate that the ice-oil-aqueous phase contact line is the hydrate heterogeneous nucleation site. A novel observation showing the critical nature of heterogeneous nucleation is reported: the heterogeneous nucleation of hydrate from ice is found to be qualitatively controlled by the temperature ramp rate in the experiment. Apparently, a low temperature ramp rate results in more heterogeneous nucleation sites for hydrate, and thus a higher surface area crystal structure than a rapid heating rate. The viscosity of a metastable hydrate-forming emulsion evolves rapidly when the emulsion is seeded with ice, although more slowly than when seeded with the hydrate itself. The critical time, defined as the time (measured from the seeding time) when an abrupt jump in viscosity is observed, decreases with higher subcooling; for hydrate-seeded emulsions this time varies from about 15 minutes to three hours as the subcooling is decreased from 7.3 °C to 4.3 °C; the slower growth with ice relative to hydrate seeding is seen in the larger critical time for ice seeding, as the critical time for ice seeding lags approximately one hour when compared to hydrate-seeded hydrate-forming emulsions, over this same range of subcoolings.

A comparison of cyclopentane hydrate- and ice-forming emulsions is reported in Chapter 4. Density-matched 40% (v/v) water emulsions are studied at various salt concentrations using experimental tools of rheometry and direct visualization of the morphology under formation of hydrate or ice from the liquid water. Viscosity and yield stress were measured at similar subcoolings (temperature differential between dissociation or melting

temperature and the system temperature, with the latter lower) and water conversions, which was controlled by the initial salt concentration in the aqueous phase of the emulsions at a fixed temperature. Large differences in viscosity and yield stress of the final structure were observed between the hydrate- and ice-forming emulsions. At water conversions of X_w = 58-81%, the ratio of final relative viscosity (final slurry viscosity relative to continuous phase viscosity) of hydrate- to ice-forming emulsion is $\frac{\eta_{rel-hyd}}{\eta_{rel-ice}} = O(10^2)$; at complete water conversion $X_w = 100\%$, the ratio is $\frac{\eta_{rel-hyd}}{\eta_{rel-ice}} = O(10)$. At water conversion of $X_w \geq 58\%$, the yield stress ratio of hydrate- to ice-forming emulsions is $\frac{\tau_{y-hyd}}{\tau_{y-ice}} \geq O(10^2)$. Morphological results show that with no salt, the hydrate seed surface punctures the drop in the hydrate-forming emulsion, consequently as the drop wets the seed, hydrate is formed; whereas in the ice-forming emulsion, the whole water drop freezes as a bulk and its spherical shape is retained. When brine is present, in the hydrate-forming emulsion, hydrate crystals form at the oil-aqueous phase interface of the drop and as they grow they puncture adjacent drops causing coalescence and wetting of the newly generated hydrate; in the ice-forming emulsion, ice growth occurs inside the drop and the growing ice remains completely wetted by residual brine, thus no significant change in the oil-aqueous phase interface is observed. These observations indicate that the ice-forming emulsions do not capture the rheological properties and mechanism of morphology evolution of hydrate-forming emulsions.

Contents

List of Figures

List of Tables

1 Introduction

1.1 Motivation

At the beginning of the 20^{th} century, frequent blockages in pipelines caused economical losses in the gas and oil industry. The crystalline plugging material inside the pipeline was initially thought to be ice. However, in 1934, Hammerschmidt found that clathrate hydrate, not ice, was the main cause of pipeline blockage [3]. Following hydrate blockage of flow, huge pressure may build up and cause bursting of the pipeline. The cost of flow lines is about 38% of an offshore investment, which often exceeds $1 billion [4]. Thus, flow assurance is considered the most critical technical problem encountered by the oil and gas companies [4, 5]

Hydrate forms when water and a hydrate-forming component such as light hydrocarbon are present under high pressure and low temperature [4, 5, 6, 7]. Therefore, hydrate plug occurrence is favored in areas along the pipelines where water is accumulated by condensation, or the flow direction is altered such as in jumpers and risers [5]. Flow failure is the undesired consequence of hydrate plugging. Rupture of the pipeline may further lead to severe equipment and environmental pollution [5]. In cases where the operation remediation is not done properly, e.g., by depressurizing only one side of the plug, the hydrate mass may eject as a projectile reaching speeds as high as 270 ft sec^{-1} [6, 5]. Fatal injuries have been reported in the field by high momentum hydrate masses. Following blockage, the remediation period my last from several days to weeks, thus

posing a serious financial burden on gas and oil companies.

The oil and gas industry has adopted several methods to prevent and remediate hydrate formation: chemical, mechanical and thermal processes. Thermodynamic inhibitors such as methanol [5, 8, 9, 10, 11, 12] and ethylene glycol [5, 4, 10, 11, 13, 14, 15] have been widely used in field operation. These chemicals shift the equilibrium condition of hydrate to lower temperatures and higher pressures by competing for hydrogen bond formation with water. This method is very effective but a large amount of additives is required to be injected in water (about 60% (w/w) [7]) making them financially unattractive. Recovery of the material from water is often difficult and costly. Alternatively, kinetic hydrate inhibitors (KHIs) are a class of low dosage polymer additives, which are injected in the pipelines. KHIs mitigate plug formation by slowing down hydrate nucleation and growth [16, 17, 18]. KHIs compete with the hydrate-forming hydrocarbon by occupying the hydrogen-bonded water cage cavity [5]. Therefore, the KHI inhibition of hydrate is only temporary. Ultimately, the hydrocarbon occupation of the hydrate cages takes over due to higher thermodynamical stability. Anti-agglomerants are another set of attractive chemicals. They prevent agglomeration by adsorbing onto the surface of the particle and changing their hydrophilicity [19, 20], thus interfering with capillary bridge formation [5, 21, 22]. Flow-driven pipeline pigging is a mechanical removal of hydrate deposition formed within a pipeline [7, 5]. Depressurization method involves shifting to low enough pressure to cause dissociation of hydrate [5]. Heating of pipes to decompose the hydrate is another method used in the industry. Challenges associated with this method involve proper location and maintaining uniform temperature throughout the length of hydrate plug [7, 5]. If temperature is not kept uniform, high pressure gas pockets may burst the pipeline.

Classical hydrate prevention methods are expensive. The amount of hydrate inhibitor in the pipeline is intrinsically dependent on the amount of water present and pose a financial burden as high as $1 million per 8 days as reported by Canyon Express [5].

Therefore, newer, more economically attractive hydrate plugging prevention methods are needed. Current research is focusing on risk management, i.e. prevention of plugging and not necessarily hydrate formation. Attaining a better understanding of the mechanism involved in hydrate formation and hydrate particle interaction will lead to reliable cost-effective flow assurance management.

1.2 Background

Clathrate hydrates are crystalline compounds in which hydrogen-bonded water cages are stabilized by a small molecule (e.g. light hydrocarbon) residing in their center. The hydrocarbon and water molecule do not form any chemical bond [19]. The size range of molecules that interact with the water cage spans from nitrogen to pentane (3.5-9 Å) [23, 5]. Molecules with size larger than the hydrogen-bonded water cavity dimensions do not enter the cages and do not form hydrates. Three major hydrate crystal structures are known: cubic I (sI), cubic II (sII), hexagonal H (sH) [23, 5, 20]. Recently a much denser trigonal structure T (sT) characterized by a low number of empty small cavities and higher ratio of number of large to small cavities was found [24]. The basic building blocks of structure I and II are the small pentagonal dodecahedral cage, 5^{12} (12 pentagonal faces) and the large tetrakaidecahedral cage, $5^{12}6^2$ (12 pentagonal and 2 hexagonal faces). Structure I is formed by combination of two small cages (5^{12}) and six large cages ($5^{12}6^2$), containing a total of 46 water molecules. Structure II is composed of sixteen small cages (5^{12}) and eight large cages ($5^{12}6^2$), consisting of a total of 136 water molecules. The third structure, sH is formed of three small cages (5^{12}), two midsize cage ($4^35^66^3$) and a large icosahedral cage ($5^{12}6^8$), containing 34 water molecules. Relatively heavier molecules such as ethane, propane, pentane fit only in the large cavities and form structure II. If no light molecules are present to occupy the small cages, sII crystals are formed with vacant small cavities, 5^{12}. Light molecules such as methane and nitrogen can fill both small and large

cages. Whether structure I or II is formed by small guest molecules is mainly dependent on the ability of the small molecule to stabilize large cages. If large cage stabilization is not achievable, *s*I is the predominant crystal structure [23]. In this work we will be concerned with *s*II hydrates.

Although hydrates are mostly composed of water [6, 2] and have similar physical properties to ice [25], the mechanism of hydrate formation is intrinsically different from ice. Ice formation is a bulk phase change of water from liquid to solid. In comparison, hydrate crystallization involves another guest molecule in addition to water. In most cases, when the two components are immiscible, hydrate formation rate is limited by mass transfer to the interface. Thus, mass transfer of the hydrate-forming water-immiscible component to the water becomes critical in hydrate formation.

Hydrate research interests span from environmental concerns to energy and technology applications. The energy of natural gas stored as hydrate, which ranges from 10^3 to 10^6 trillion cubic meters, is estimated to be twice that of the global fossil fuel, approximately 10,000 Gigatons [25, 7, 26]. The molar amount of methane stored in hydrate is 164 times the amount of methane found in an equivalent volume as gas at standard temperature and pressure. As fossil fuel sources become scarce, hydrate sediments may be utilized to meet our future energy demands. New ways to harness the energy in the hydrate are under investigation.

In addition to hydrate sediments potentially providing energy in the future, they also pose a serious threat to global climate. The amount of methane present as hydrate in the arctic regions and oceans, if released in the atmosphere by decomposition, may adversely affect global climate [27, 28]. Methane has the ability to absorb 24 times more infrared radiation than carbon dioxide, presenting a serious greenhouse effect concern [29]. Englezos and Hatzikiriakos [19] predict that hydrate depositions below the permafrost may start to melt in the next 100 years, but suboceanic hydrates will not be affected for another 1000 years [28]. Nevertheless, hydrate also offers a venue for carbon dioxide

sequestration as suggested by several studies [19, 28, 30]. Carbon dioxide injection into methane hydrate (to displace the hydrate as carbon dioxide hydrate is thermodynamically preferred state of water under certain conditions) has been suggested as a method of carbon hydrate sequestration and methane capturing [31].

Gas separation is also achievable through use of processes involving hydrate. Under high pressure and low temperature, hydrate-forming gases can be separated from a gas mixture and sequestered as a solid phase. The cost required to achieve high pressures is often the most challenging aspect of commercializing hydrate gas separation technology. Promising studies have shown that promoters reduce the pressure required to form hydrates [32, 33, 34, 35, 36]. Another favorable feature of separating gas by forming hydrate is the fact that it can be safely and densely packed as solid. For example, methane hydrates are metastable at moderately low temperatures and atmospheric pressures [37]. Therefore, storage of gas may be achieved more safely in hydrate formation than classical high pressure cylinders.

In addition to being an energy source, hydrate can also be a source of clean fresh water. Due to the rapid growth of world population and scarce resources, shortage of fresh water is a threat for the well-being of humanity [38]. Salt is not incorporated into hydrate, thus water can be concentrated as hydrate solid and then melted providing high purity water. In areas where fresh water sources are rare, hydrate can be useful in providing fresh water by desalination of seawater [39, 19]. Furthermore, desalination through hydrate rather than ice is not limited to temperatures below the freezing point of ice.

The high latent heat and thermodynamic stability above ice melting temperature make hydrate a candidate in phase change material (PCM) slurries [40, 41, 42, 43, 44, 45, 46]. PCM slurries serve as heat transfer and storage fluids, finding application in cooling systems such as refrigerators and air conditioners. Currently, ice slurries are the most widespread method. However, some hydrate slurries such as CO_2 hydrates have intrinsic advantages, i.e., higher latent heat than ice slurries. The latent heat of CO_2 hydrate is

507 kJ kg^{-1}, while that of ice is 333 kJ kg^{-1} [47]. Hydrate slurry is appropriate for air conditioning because it can form in temperature range of 5-12 °C, while ice slurry lowers its efficiency due to the fact that phase change occurs at a lower temperature, 0°C [43]. Nevertheless, agglomeration occurrence leading to plugging hinders full implementation of hydrate based PCM technologies [41]. In order to have the highest heat transfer efficiency, hydrate slurries are required to fully flow in the device. Thus, assurance of flow is necessary to have economical and efficient hydrate based refrigerators. The focus of this work is a mechanistic understanding of the process involved in hydrate formation in slurries.

1.3 Outline

This thesis is arranged in five self-contained chapters. Figure 1.1 provides an overview of the main topics discussed in this thesis. Chapter 2 describes an experimental analysis on the salt effect on thermodynamic and rheological properties of cyclopentane hydrate-forming emulsions. Using calorimetry we devised a novel method of measuring the equilibrium temperature of hydrate at various salt concentrations in the aqueous phase and cyclopentane concentrations in the oil phase. Since oil and water are immiscible, a hydrate shell forms at the oil-aqueous phase interface, which acts as mass transfer barrier between the two phases and inhibits the reaction. Since hydrate formation is limited by mass diffusion, there is negligible change in the salt and cyclopentane concentration. Equilibrium temperature can be measured when the hydrate shell melts in contact with known salt and cyclopentane concentrations. Experimental data compare well with thermodynamic simulations. Hydrate-forming rheological properties, including viscosity critical time (time when an abrupt jump in viscosity is observed), the viscosity evolution time (time from critical time to achieve final viscosity), final viscosity and its shear rate dependence, and yield stress are determined. The rheological properties are correlated

to the thermodynamic driving forces. The viscosity evolution time is smaller at lower temperature, i.e., at higher subcooling relative to the hydrate equilibrium dissociation temperature. The final hydrate slurry viscosity is shear thinning. At thermodynamic water to hydrate conversion of 61-85%, a peak in final viscosity is observed. The maximum yield stress is achieved at 80% conversion. The viscosity and yield stress behavior indicate that liquid (brine) may form capillary bridges between the hydrate particles.

The importance of the ice-oil-aqueous phase (IOA) contact line in hydrate nucleation and growth is discussed in Chapter 3. Morphological experiments show that heterogeneous nucleation by ice and hydrate growth occurs at the oil-aqueous phase interface. In single drop experiments, hydrate conversion rate increases with more IOA contact line. A novel experiment where ice is in contact with three regions, aqueous phase, oil and oil-aqueous phase, indicates that the hydrate nucleation occurs at IOA followed by hydrate growth at the interface. Rheological experiments show that when an otherwise metastable hydrate-forming emulsion is seeded with ice, an abrupt increase in viscosity is observed. Thermodynamic conditions such as temperature and salt concentration are specifically designed in this study to eliminate or minimize water to ice conversions; thus the observed mechanical properties are unambiguously related to hydrate formation only. As the abrupt increase in viscosity occurs faster at lower temperatures, this study elucidates the fact that both nucleation and hydrate growth rate are dependent on subcooling. A larger critical time for ice seeding compared to hydrate seeding is observed.

In Chapter 4, modeling oilfield emulsions under low pressure conditions is discussed. An experimental comparison of the rheological and morphological properties of cyclopentane hydrate- and ice-forming emulsions is given. Final viscosity and yield stress were measured at similar subcoolings and water conversions. The water conversion was controlled by varying salt concentration at a fixed temperature. Hydrate-forming emulsion final and yield stress is orders of magnitude higher compared to ice slurry at moderate and full water conversions. Morphological results showed that at no salt conditions, the hydrate

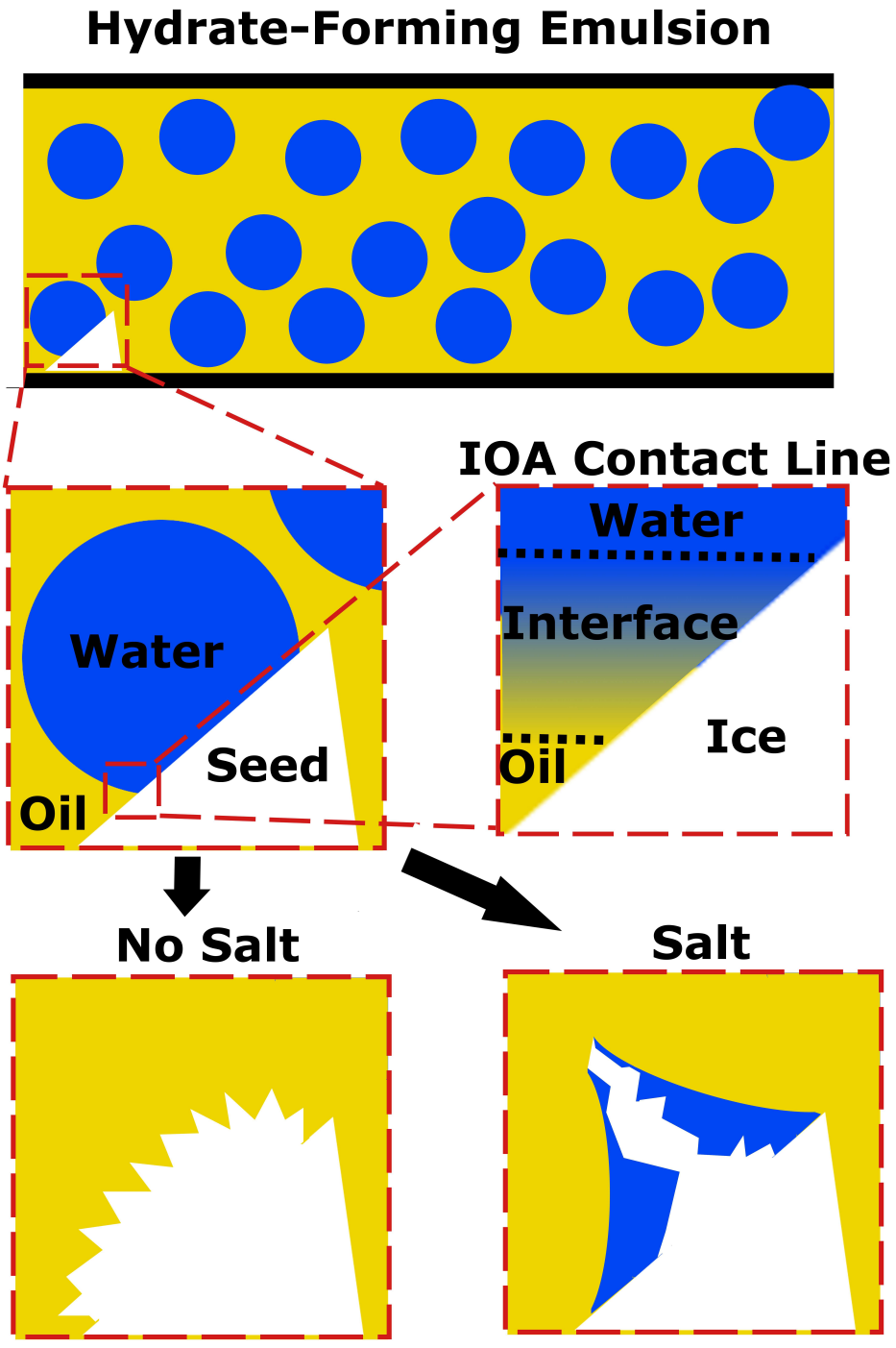

Figure 1.1: A schematic depiction of thesis topics: hydrate-forming emulsion rheological properties, nucleation at the ice-oil-aqueous (IOA) phase contact line and the morphology of hydrate forming emulsion without and with salt.

seed punctures the drop and a mushy/hairy morphology is observed; such puncturing mechanism is not present in ice-forming emulsion and the whole drop freezes as bulk and retains a spherical shape. In the presence of brine, hydrate forming at the interface punctures the other drops and coalesces them causing wetting of the newly generated hydrate; in the ice-forming emulsion, ice growth occurs inside the drop and is fully wetted by brine, thus no significant change if oil-aqueous phase interface occurs.

In Chapter 5 a summary of the main thesis conclusion is given. Based on these conclusions, future topics of interest are proposed. Possible ways to approach future investigations are discussed.

2 Salt effects on thermodynamic and rheological properties of hydrate forming emulsions*

2.1 Introduction

Due to the fact that offshore petroleum wells occur under the seafloor, the effect of the salinity of the aqueous phase in water produced with petroleum is an important factor to be considered for the formation of hydrate. Here, we consider the case of water-in-oil emulsions, modeling the case of produced water (or brine) emulsified with crude oil, considering only NaCl solutions although numerous other ionic species may generally be present in produced water. Salt is a thermodynamic inhibitor of hydrate formation. At the simplest level, the presence of dissolved salt results in an increase in ionic strength in the water, and causes a colligative effect that lowers the equilibrium temperature of hydrate; this is the same phenomenon as the well-known freezing point depression of water by addition of salt. In addition, the salt ions have more specific effects, as they interact with the water molecules preventing formation of hydrate cages [5]. Note that the hydrate lattice does not incorporate ions, and thus the chemical potential of water embedded in the hydrate structure is not affected by the presence of salt [49]. Salt does, however,

*The contents of this chapter are published as a paper in *Chemical Engineering Science* [48].

affect the chemical potential of the aqueous phase [49, 50].The chemical potential model of water in the form of hydrate was developed by van der Waals and Platteeuw [51, 52]. A few models [49, 50] incorporate the effect of electrolytes in the aqueous solution to calculate hydrate equilibrium conditions and salt precipitation.

As noted, increase of salt concentration in the aqueous phase lowers the equilibrium temperature for hydrate stability (effectively the melting point of the hydrate). Regardless of the salt concentration of the aqueous phase, the dominant factor affecting morphology of hydrate crystals appears to be the level of subcooling $\Delta T = T_{eq} - T$; at higher subcooling, crystal size is decreased [53, 54]. Maeda *et al.* [55] reported that after nucleation, hydrate growth rate (for chlorodifluoromethane gas hydrates) is independent of the salt concentration in the aqueous phase. However, in an emulsion studied here, the concentration of salt inside the water droplet increases with hydrate formation and consumption of water, and this impacts on the growth rate. As salt concentration rises, the equilibrium temperature is further shifted to lower values, consequently resulting in less subcooling, slowing hydrate growth [56] and limiting the ultimate conversion.

Rheological properties are essential in understanding the flow behavior of hydrate suspensions and avoiding plugging of pipelines. In the case of a water-in-oil emulsion, viscosity generally increases and a yield stress may develop as hydrate forms at the water-oil interface. Colombel *et al.* [57] and Sinquin *et al.* [58] developed a model describing the viscosity of hydrate suspensions (assuming the water drops to convert to hydrate particles) in oil as a function of effective volume of hydrate agglomerates. This approach is based on the theoretical model of Mills [59] for flocculated suspensions. In the model, viscosity is dependent on the initial water fraction [57], and this indicates that an important factor in determining the mechanical properties of a hydrate-forming emulsion, which needs to be carefully considered when salt is present in the aqueous phase, is the extent of conversion of water into hydrate.

In order to assess the importance of conversion in determining rheological properties, an

experimental investigation of density-matched cyclopentane hydrate-forming emulsions in the presence of salt is performed here. Cyclopentane, the hydrate forming component in the oil system, forms the cubic hydrate structure II (sII) [6], as does natural gas, but cyclopentane hydrate is stable under atmospheric pressure. Thus cyclopentane hydrate provides a model for natural gas hydrate behavior in an emulsion system, without the need for pressurized experimental environments. In this work, a binary phase diagram for cyclopentane hydrate-brine system is constructed employing calorimetric data. At the salt concentrations and temperature range studied here, no precipitation of salt was visually observed by Kishimoto *et al.* [54]; simulated data (employing the package PVTsim; Calsep) further confirm the absence of solid salt phase for our experimental conditions. Equilibrium temperature and theoretical hydrate conversion are extracted from the binary phase diagram. The correlation of rheological data measured at varying conversion levels of water to hydrate elucidates underlying physical principles involved in the mechanical properties of hydrate-forming emulsions.

2.2 Experimental

2.2.1 Materials

Sodium chloride (99+% pure, Fisher Scientific) is dissolved at various concentrations in deionized water obtained from a Millipore QTM system to form the aqueous phase. For the calorimetric experiments, two oil phases were examined: 1) a simpler oil phase containing only light mineral oil (NF/FCC Fisher Scientific) and cyclopentane (99+% pure, Fisher Scientific) and 2) the density-matched emulsion oil phase composed of halocarbon 27 (polychlorotrifluoroethylene polymer, Halocarbon Products Corporation), light mineral oil and cyclopentane. The oil phases containing 37, 50 and 100% (v/v) cyclopentane were investigated in the micro-differential scanning calorimeter (μDSC) experiments

where hydrate formation occurs between the aqueous and oil bulk phases. Additional experiments were carried out for the case of 100% (v/v) cyclopentane concentration by adding sorbitan monooleate (Span 80 from Sigma-Aldrich) at a concentration of 0.05% (v/v on the organic component); agitation was not performed on the calorimetric experiments. Equivalent volumes of 50 μL of the aqueous and oil phases were used to measure the equilibrium temperature of hydrate formed at the interface in a segregated system at various cyclopentane and salt concentrations.

Hydrate-forming emulsions with various salt concentrations are investigated in the rheological experiments. The oil phase of hydrate-forming emulsion is composed of 50% (v/v) cyclopentane. The rest of the oil phase is a mixture of light mineral oil and halocarbon 27 used to match the density of the oil and aqueous phase in order to minimize sedimentation of the droplets in the emulsion (or 'creaming', given that the drops rise in this mixture). Span 80 is used as a surfactant to stabilize the emulsion at a concentration of 0.05% (v/v) in the oil phase. Span 80 is a non-ionic surfactant with a hydrophilic-lipophilic balance (HLB) of 4.3 [60]. Due to high hydrophobicity, Span 80 does not form stable lipid bilayers in the aqueous phase [61]. The measured critical micelle concentration of Span 80 in the emulsion oil phase is 0.027% (v/v), which closely agrees with previously reported values [62]. Relevant physical properties of the materials are provided in Table 4.1.

Table 2.1: Materials physical properties

Material	Chemical Formula	Mol. Weight (g mol^{-1})	Density (g cm^{-3})	Viscosity (cP)
Cyclopentane	C_5H_{10}	70.1	0.751 (25 °C)	0.44 (20 °C)
Halocarbon 27	$(C_2ClF_3)_n$	-	1.96 (37 °C)	51 (37.8 °C)
Light mineral oil	-	-	0.83 (15.6 °C)	46 (25 °C)
Span 80	$C_{24}H_{44}O_6$	428.6	0.986 (25 °C)	1200-2000 (20 °C)
Water	H_2O	18.0	1.00 (4 °C)	1.00 (20 °C)
Sodium Chloride	NaCl	58.4	2.16 (25 °C)	-

2.2.2 Micro-differential scanning calorimeter (μDSC)

A micro-differential scanning calorimeter (μDSC VII; Setaram) is used to measure the equilibrium temperature and the cumulative dissociation heat of the cyclopentane hydrate and brine system. The μDSC measures the heat flux required in the sample vessel to match the temperature of the reference vessel as the temperature is raised at a specified rate. The heat flux resolution is 0.02 μW. A more detailed setup of the apparatus is described by Le Parlouër *et al.* [63]. The procedure in the μDSC experiments involves lowering the temperature to -40°C to form ice. Thereafter, the temperature is raised above the equilibrium temperature of ice, but below the equilibrium temperature of hydrate formation (both of which are dependent on the concentration of salt in the aqueous phase) following a protocol described by Karanjkar *et al.* [64]. The temperature is kept steady for one hour, to provide time for hydrate formation to occur. The temperature is then steadily increased at 0.2°C min^{-1} in order to detect hydrate dissociation as shown in figure 2.3.

2.2.3 Interfacial tension

An optical tensiometer (Theta; KSV Instruments) was employed to measure the interfacial tension between the oil and aqueous phases. To dispense the oil drop in the bulk aqueous phase, a 16 gauge inverted needle (Ramé-Hart Instrument Co.) was used. The Young-Laplace equation is applied to the acquired image to find the interfacial tension between the two phases. The critical micelle concentration (CMC) for the oil phase (light mineral oil, halocarbon 27, and cyclopentane; hereafter called oil mixture) similar to the emulsion but slightly density mismatched (ρ = 0.91 g ml^{-1}) to allow pendant drop formation, was determined experimentally at 0.027% (v/v) Span 80 concentration. The interfacial tension of the aqueous droplet formed in the oil mixture is $O(10^{-3}$ N/m) as plotted in figure 2.1 for various salt concentrations. Salt does not affect interfacial ten-

sion between the aqueous and oil mixture phases in the presence of 0.05% (v/v) Span 80 as shown in figure 2.1. The interfacial tension of the oil mixture containing no Span 80 and aqueous phase is also shown in figure 2.1; at salt concentrations of 7.5, 10 and 12.5% (w/w), the interfacial tensions between the oil mixtures and aqueous phases are the same whether Span 80 is absent or present. At salt concentrations of 0, 3.4, 5 and 15 % (w/w), absence of Span 80 causes a larger interfacial tension between the oil mixture and aqueous phases. Apparently, salt concentration causes interfacial tension in the oil mixture without Span 80 to change. In order to further investigate the effect of salt on the interfacial tension between the oil mixture and aqueous phase, the interfacial tension of individual components in oil mixture (light mineral oil, halocarbon 27, cyclopentane) and aqueous phase at specified salt concentrations were measured. In comparison with light mineral oil and cyclopentane, halocarbon 27 interfacial tension with aqueous phase is lower; with addition of salt in the aqueous phase, the interfacial tension between halocarbon 27 and aqueous phases approaches the interfacial tension of the oil mixture and aqueous phase at 0.05% (v/v) Span 80, indicating the presence of surface active agents in halocarbon 27 oil.

The presence of salt ions (Na^+ and Cl^-) is known to decrease the interaction between the polar head of Span 80 and water in the aqueous phase [65, 66]. Salt ions interact with water molecules; they exist in the hydrated form in the aqueous phase [66]. Thus, due to water molecules interacting strongly with the salt ions, a diminished non-ionic surfactant-water interaction referred to as a salting out is observed [65, 67]. In figure 2.1, the interfacial tension between the aqueous phase, and the pure oil phase components, cyclopentane and light mineral oil, initially decreases reaching a minimum value followed by an increase at higher salt concentration. In figure 2.1 the small decrease in interfacial tension of light mineral oil at salt concentration in brine of $X_s \leq 3.4\%$ (w/w) and cyclopentane at $X_s \leq 5.0\%$ (w/w) may be associated with impurities in the oil phase which partition to the aqueous phase [67]. In the presence of salt, surface active impu-

rities tend to accumulate in the interface region rather than in the bulk aqueous phase due to the salting out phenomena, resulting in a decrease in interfacial tension. At high salt concentration, at $X_s \geq 3.4\%$ (w/w) for light mineral oil and $X_s \geq 5.0\%$ (w/w) for cyclopentane there is an increase of interfacial tension which is due to additional energy needed to create an ion free zone in the interface [68]. In the case of halocarbon 27, a small concentration of unsaturated alkenes is present (information provided from Halocarbon Products Corporation brochure and representative correspondence). Unsaturated alkenes react with water resulting in acidic components which may behave as surfactants.

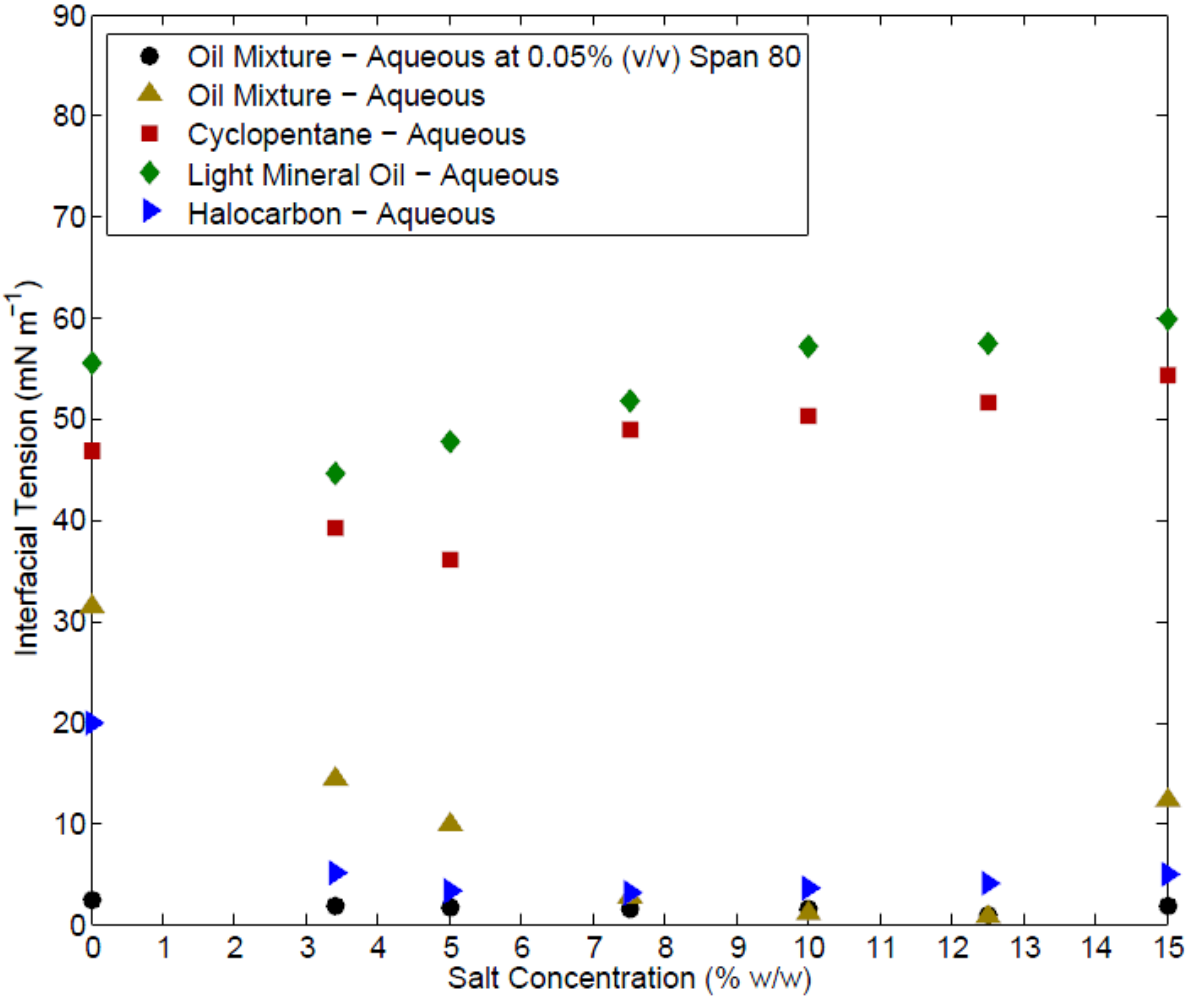

Figure 2.1: Interfacial tension between oil and aqueous phases at various salt concentrations. Oil mixture ($\rho = 0.91$ g ml^{-1}) is similar to the emulsion oil phase.

2.2.4 Rheology

Rheometric analysis was performed on density-matched 40% (v/v) aqueous fraction emulsions. Mixing of a total volume of 50 ml of water and oil to form a water-in-oil emulsion is achieved using the IKA T25 Digital Ultra-Turrax at an intensity of 7000 rpm for a duration of 5 minutes. To estimate the numerical average mean and volume mean diameter, 700 droplets for each condition were measured under microscope following emulsification. Photomicrographs are shown in figure 2.2. The droplet size is $O(10^{-5}$ m) as shown in Table 3.2. The droplet size numerical average and volume mean diameter have the lowest value at 3.4% (w/w) salt concentration and the highest value at 15% (w/w) salt concentration. The ratio of the highest and lowest numerical average mean size is 2.4, while for the volume mean diameter it is 2.5.

Table 2.2: Hydrate-forming emulsion droplet size

Salt Concentration % (w/w)	Numerical Average Mean $\frac{\sum n_i d_i}{\sum n_i}$ (μm)	Standard Deviation (μm)	Volume Mean Diameter $\frac{\sum n_i d_i^4}{\sum n_i d_i^3}$ (μm)
0.0	11.7	10.9	44.9
3.4	9.7	6.9	29.1
5.0	10.9	11.1	53.5
7.5	13.3	10.2	45.9
10.0	13.3	8.6	40.0
12.5	18.4	14.0	47.6
15.0	23.2	16.0	71.4

In all experimental conditions the maximum capillary number, the ratio between the viscosity forces and the capillary forces, is estimated to be $Ca_{max} = \frac{\eta_c \dot{\gamma} d}{\sigma} = O\left(10^{-2}\right)$, where $\eta_c = 0.0055$ Pa s is the continuous fluid viscosity of the emulsion, $\dot{\gamma}$ is the shear rate, d is the droplet diameter and σ is the interfacial tension between the two phases. Therefore, negligible droplet deformation is expected for the conditions of the experiments [69].

The emulsions do not coalesce for several days. However, flocculation and sedimentation have been observed under quiescent conditions after a few hours. Hydrate-forming

emulsions at 40% (v/v) aqueous fraction are shear thinning [62]. Disruption of flocs of drops formed under quiescent conditions may be responsible for shear thinning behavior [70]. Matching oil and aqueous phase densities at room temperature reduces separation, but matching densities at all temperatures is not possible; thus, sedimentation of droplets (or 'creaming', the term often used when the drops rise as in our case) is slowed but not eliminated. We estimate the effects of segregation due to density difference by computing the time for hydrate particles (which will generally contain liquid aqueous phase when salt is present) to move a distance necessary to affect the rheometric measurements, namely a fraction of the Couette bob length, l: for simplicity we will take the distance to be l so that the time estimate is $t_s = l/U$, where U is the settling (rising in this case) velocity. At low conversions of water to hydrate, sedimentation can be considered negligible due to small density differences between the oil and hydrate particles, which are still mostly liquid aqueous phase. The density difference is at its maximum at highest conversion, achieved at the lowest temperature, T = -13°C. Sedimentation is hindered by the presence of other particles and liquid back flow [71, 72, 73]. The settling velocity of a particle in suspension is $U = U_0(1-\phi)^n$, with $n = 4.65$, $U_0 = \frac{g(\rho-\rho_p)d^2}{18\eta_c}$ is Stokes settling velocity for a single particle in infinite fluid [72], and ϕ is the volume fraction of the suspension[71, 72, 73]. The volume fraction of hydrate suspension after conversion is assumed to be the aqueous phase fraction, $\phi = 40\%$. The continuous phase density, ρ, is estimated after hydrate conversion, with the remaining mixture density of the Halocarbon 27, light mineral oil and the unconverted cyclopentane. The particle phase density, ρ_p, is estimated from the remaining aqueous phase and hydrate. Particles are assumed to have the diameter of the numerical average droplet diameter given in Table 3.2. Density of the cyclopentane-hydrate has previously been estimated as 0.965 g cm^{-3} [64]. Estimated suspension settling velocity and time for the highest conversion at each salt concentration are given in Table 2.3.

Experiments are started immediately following mixing to attenuate the effects of floccu-

Table 2.3: Estimated settling velocity and time of hydrate suspension

Salt Concentration % (w/w)	Maximum Conversion (T = -13°C) %	Density Difference $\rho - \rho_p$ (kg m^{-3})	Settling Velocity U (μm s^{-1})	Settling Time t_s (hours)
0.0	100	98.9	0.124	74.6
3.4	87.4	91.6	0.0794	117
5.0	81.2	87.4	0.0957	97.3
7.5	71.2	79.9	0.130	71.5
10.0	60.6	70.8	0.115	80.6
12.5	49.5	60.1	0.187	49.6
15.0	37.8	47.8	0.237	39.3

lation and sedimentation; depending on the specified condition experiments may last from 1/2 to 12 hours. Since the dominant conversion takes place at shorter times, the resulting increase in viscosity and eventual development of a porous network will significantly decrease the segregation velocity. It should also be noted that for lower conversions, time required for settling is larger due to lower density differences. The experimental times are thus well below the estimated settling times, and suspension settling is not believed to affect the flow properties significantly.

A volume of 15 mL emulsion is transferred to the Couette cup of the rheometer at room temperature (T $\approx$ 25°C). The cup is placed inside a fluid bath in the rheometer, where it is quickly quenched to a lower temperature. Two approaches are used in crystal nucleation. The first approach is to allow nucleation to occur on its own; this method is used in the investigation of critical time of hydrate formation (figure 2.8). The second method involves seeding the emulsion at $t = 90$ s (shearing starts at $t = 0$) with a hydrate crystal of approximately 1 mm in diameter placed on the upper surface of the emulsion, specifically on the layer covering the inner cylinder in the Couette geometry; this method is used for the investigation of the viscosity evolution time and final viscosity (figure 2.8).

A strain controlled rheometer (ARES Rheometrics) is used to measure the rheological properties of the hydrate-forming emulsion. This rheometer is equipped with a dual-range force rebalance transducer (2K FRTN1). The software automatically switches between the lower range (2×10^{-6} to 2×10^{-2} N m) and higher range (2×10^{-4} to 2×10^{-1} N

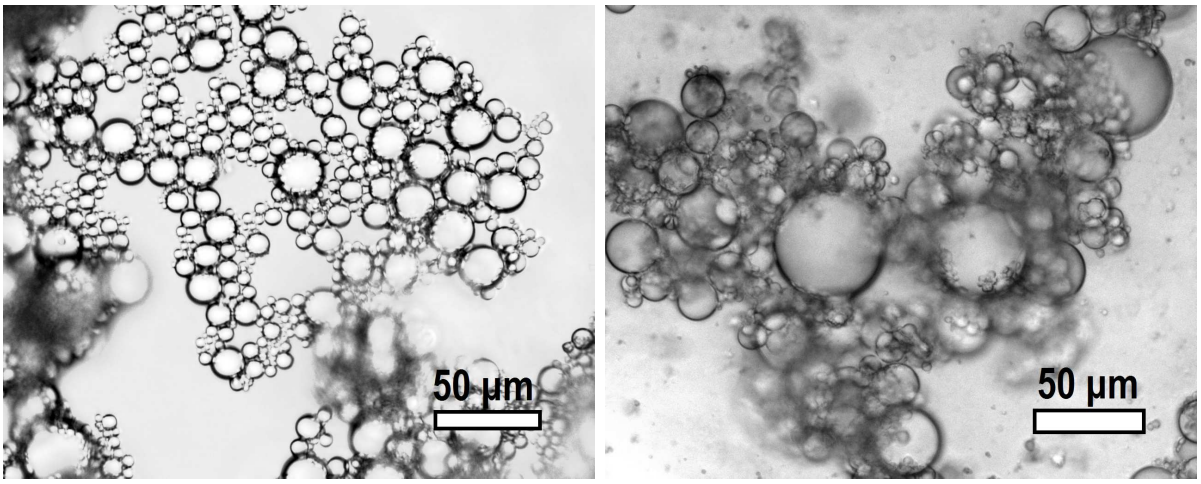

(a) No salt (b) 7.5% (w/w) salt

Figure 2.2: Representative photomicrographs of the hydrate-forming emulsions.

m) when necessary, and this is observed to occur under certain of the conditions studied here. The Couette geometry is used in the rheometer. The cup diameter is 34 mm. The bob diameter is 32 mm with a length of 33.5 mm. Thus, there is 1 mm gap between the concentric cylinders. Temperature control is achieved through a re-circulating fluid bath. Temperature is measured by a thermocouple in direct contact with the cup.

The emulsions are sheared at constant rates of 1 s^{-1} and 100 s^{-1} until the measured viscosity reaches a steady value. The final formed slurry structure without any aging process (i.e., immediately following hydrate formation under shear) is run through a shear rate loop from 1 to 100 s^{-1} and back to 1 s^{-1} (total loop duration is 2000 s) to determine whether hysteresis is present. The yield stress of the final slurry material was determined by the method used by Yang *et al.* [74]; shear stress was measured as the rate increased from 10^{-4} to 1 s^{-1}, the yield stress was identified as the value of the stress plateau at low shear rate in the plot.

2.2.5 Thermodynamic data simulation

The thermodynamic simulator, PVTsim version 20 (Calsep A/S) was used to predict the liquidus data and water to hydrate conversion in the emulsion at various salt concentrations. A comparison of PVTsim to other softwares in predicting hydrate formation is given by Ballard and Sloan; experimental data are predicted quite well by PVTsim [75]. The volumetric concentration of cyclopentane was adjusted by the addition of normal-octane which is comparable to light mineral oil (a mixture of alkanes) used in the μDSC experiments. Water and sodium chloride formed the aqueous phase. The aqueous fraction of the emulsion was set at 40% (v/v) as in the experiments. The Soave Redlich Kwong (SRK) equation of state with Peneloux volume correction equation [76] is used in the simulations. Solid salt formation was observed in the simulation at $T \leq$ -16.0 °C for 3.4% (w/w) salt concentration and at $T \leq$ -15.6 °C for 15% (w/w) salt concentration. Therefore, no solid salt precipitation is expected in temperature range of $T \geq$ -13.0 °C at which the rheometric experiments are run.

2.3 Results and discussion

2.3.1 Thermodynamic conversion

Figure 2.3 shows the heat flow measured by μDSC during the study of cyclopentane hydrate formation in a segregated water/organic sample. Recall this is the system without surfactant added. These experiments allow determination of properties at a precise concentration, because conversion is minimal under these segregated conditions with only a small surface area between the organic and aqueous phases. When the temperature of the aqueous and cyclopentane bulk phases is lowered from 25 °C to -40 °C at a rate of 1.5 °C min^{-1}, an exothermic peak is observed at -10 °C due to ice formation. This is higher than the homogeneous nucleation temperature for ice observed at -38 °C by Zhang *et*

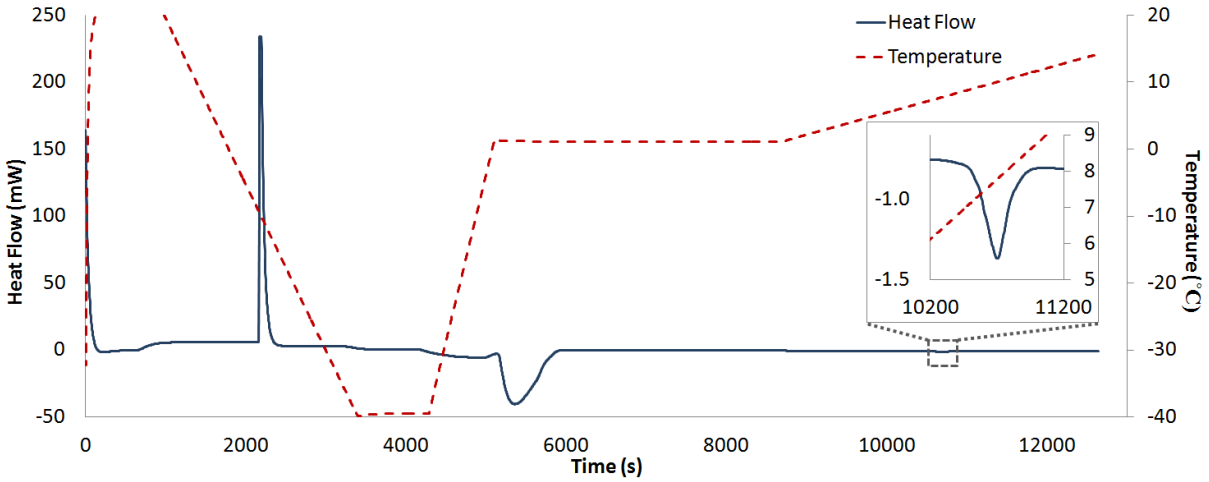

Figure 2.3: μDSC graph for hydrate formation between aqueous and oil bulk phases.

al. [77]. Homogeneous nucleation is rarely achieved [78], while heterogeneous nucleation occurs at a significantly higher temperature due to the presence of solid interfaces [77, 6], as discussed in Karanjkar *et al*. [64]. The exothermic peak observed in the experiment corresponds to the heterogeneous nucleation and growth of ice crystals in the bulk aqueous phase. The formation of ice is further confirmed when the solution is heated to 1°C, above the melting temperature of ice (0°C) and an endothermic peak of comparable total energy is seen. The asymmetrical non-bell shaped exothermic peak is typical of the ice formation in bulk water as opposed to a symmetrical bell-shaped crystallization of an emulsion [79]. During ice melting, free liquid water becomes available allowing hydrate crystal growth [64] and it has been argued that long-lived hydrogen bonds [80] supplied from ice dissociation cluster together forming hydrate crystal nuclei between the aqueous and cyclopentane-containing oil phase. The nucleation of hydrate based on the thermal history such as melting of ice is referred as the memory effect of the solution [81], but may also be due to the nearby ice surface during the period of melting.

The fraction of water converted to hydrate in the two bulk phase experiments is

$$X_w = \frac{Q}{\Delta H_{hyd} m_{w-in}}, \tag{2.1}$$

where Q, the heat released during the hydrate dissociation, is calculated from the area under the small endotherm (enlarged in the inset) at 6.3-8.8 °C in figure 2.3. The initial water content is m_{w-in}. The hydrate formation enthalpy is $\Delta H_{hyd} = 348.9$ kJ/kg water converted. The heat of formation of hydrate on a converted water basis is computed from the heat of cyclopentane hydrate dissociation, 283.9 kJ/(kg hydrate) [82], and the ratio 1:17 of cyclopentane to water molecules forming the hydrate [77].

When no Span 80 is present, the computed fractions of water converted to hydrate ranges from $X_w = 0.1$ to 5.4% with most cases below 2% conversion as shown in Table 2.4. Therefore, the change in salt and cyclopentane concentrations in the aqueous and oil phase, respectively, are small and considered to be negligible. The temperature data in Table 2.5 represent an experimental evaluation of the liquidus line in the hydrate-brine system, which is the highest temperature at which the hydrate crystal and brine coexist, i.e. this represents the melting point of the hydrate in contact with such a brine. Above the liquidus line as shown in figure 2.6, hydrate is not thermodynamically stable and only brine is present. Below the liquidus line as temperature decreases, the ratio of solid to liquid phase increases.

When no Span 80 is present, the melting point of cyclopentane hydrate in cyclopentane-water system without salt is found to be 7.11 ± 0.10 °C, which is close to the value reported by Zhang and Lee [33] of , 7.02 °C, and the quadruplet point reported by Fan *et al.* in which four phases (a liquid water-rich phase, a cyclopentane-rich phase, a solid hydrate phase, and a vapor phase of cyclopentane + water) are in equilibrium is 7.07 °C [83]. When 0.05 % (v/v) Span 80 is dissolved in cyclopentane, the water fraction converted to hydrate without salt is significantly higher ($X_w = 42.6\%$) compared to when Span 80 is absent ($X_w = 0.7\%$); note that no agitation is performed. Moreover, the equilibrium temperature is lowered by $\Delta T = 0.63$°C in the presence of 0.05% (v/v) Span 80. Hydrate formation in the interface is highly affected by surfactant activity. Karanjkar *et al.* [64] observed that without Span 80 a polycrystalline shell is formed on the water-

oil interface; when Span 80 is present, a mushy porous structure with small needle-like crystals is formed in the interface which fill the aqueous phase as more hydrate is formed. This is consistent with the conversions observed in our μDSC experiments where in the presence of Span 80 up to a sixty fold increase in water to hydrate conversion is measured even with no agitation. Porous hydrate may cause a melting temperature depression referred to as the Gibbs-Thomson effect due to more interface being present similar to porous ice; the premelting of ice is reviewed in detail by Dash *et al.* [84, 85].

Table 2.4: Liquidus data for ice [1] and cyclopentane hydrate at 100% (v/v) cyclopentane

	Ice Data interpolated from Stephen and Stephen [1]	Hydrate Cyclopentane Concentration 100% (v/v)	
Salt Concentration (% w/w)	Equilibrium Temperature (°C)	Equilibrium Temperature (°C)	Water Converted (%)
0.0 (no Span 80)	0.0	7.11 ± 0.10	0.8 ± 0.2
0.0 (0.05% Span 80)	-	6.57 ± 0.01	42.3 ± 3.3
3.4	-2.5	5.28	4.9
5.0	-3.6	4.27	5.4
7.5	-4.8	2.71	1.8
10.0	-7.0	1.16	0.7
12.5	-8.5	-0.79	0.6
15.0	-11.0	-3.51	1.1
17.5	-13.1	-5.50	1.0
20.0	-16.2	-8.00	0.9
23.0	-21.1	-11.66	0.4

In figure 2.4, the experimental and simulated liquidus temperatures for various salt concentrations are plotted. The ice-brine equilibrium data plotted in figure 2.4 are taken from Stephen and Stephen [1]. The limits of cyclopentane concentration used are chosen to guide our understanding of the results from the emulsion studies. The 50% (v/v) cyclopentane concentration represents the initial condition in the emulsion when no water is converted to hydrate ($X_w = 0\%$). The 37% (v/v) cyclopentane concentration represents the concentration of cyclopentane when all water is assumed to be converted to hydrate ($X_w = 100\%$). Thus, these two conditions represent the absolute upper and lower limits of cyclopentane concentration in the emulsion under study.

Table 2.5: Hydrate liquidus data for the simple oil phase (light mineral oil and cyclopentane (LMO+CP)) and the emulsion oil phase (light mineral oil, Halocarbon 27 and cyclopentane (LMO+HLC+CP)).

		LMO+CP		LMO+HLC+CP	
Cyclopentane Concentration (% v/v)	Salt Concentration (% w/w)	Equilibrium Temperature (°C)	Water Converted (%)	Equilibrium Temperature (°C)	Water Converted (%)
50	0.0	5.40	0.4	5.39	3.5
	3.4	3.30	0.6	3.50	3.7
	5.0	2.45	0.9	2.68	0.03
	7.5	1.01	0.7	1.30	2.9
	10.0	-1.03	1.6	-0.23	0.1
	12.5	-2.71	1.2	-2.73	2.1
	15.0	-4.61	0.4	-5.03	1.5
	17.5	-7.38	0.6	-7.29	1.2
	20.0	-9.79	0.1	-9.44	0.4
	23.0	-13.68	0.3	-13.45	0.2
37	0.0	4.41	0.2	4.70	3.4
	3.4	2.32	0.4	2.80	1.5
	5.0	1.55	0.5	1.76	2.6
	7.5	-0.46	1.8	0.04	1.4
	10.0	-2.10	1.1	-1.94	2.3
	12.5	-4.14	0.5	-3.58	1.0
	15.0	-6.07	0.5	-5.93	1.3
	17.5	-8.04	0.5	-7.95	0.6
	20.0	-10.90	0.3	-10.67	0.3
	23.0	-15.35	0.3	-14.48	0.3

Water conversion to hydrate is given by

$$X_w = \frac{m_{w-hyd}}{m_{w-in}} \ , \tag{2.2}$$

where m_{w-hyd} is the mass of water in hydrate and m_{w-in} is the initial mass of water in the emulsion. The mass of water in hydrate is expressible as

$$m_{w-hyd} = m_{tot} X_{hyd} (1 - X_{s-hyd}) \ , \tag{2.3}$$

where m_{tot} is the total mass of water and salt, X_{hyd} is the fraction of aqueous phase converted to hydrate and X_{s-hyd} is the fraction of salt in hydrate. The fraction of aqueous phase converted to hydrate is obtained by mass balance of two phases, $X_{hyd} + X_{brine} = 1$,

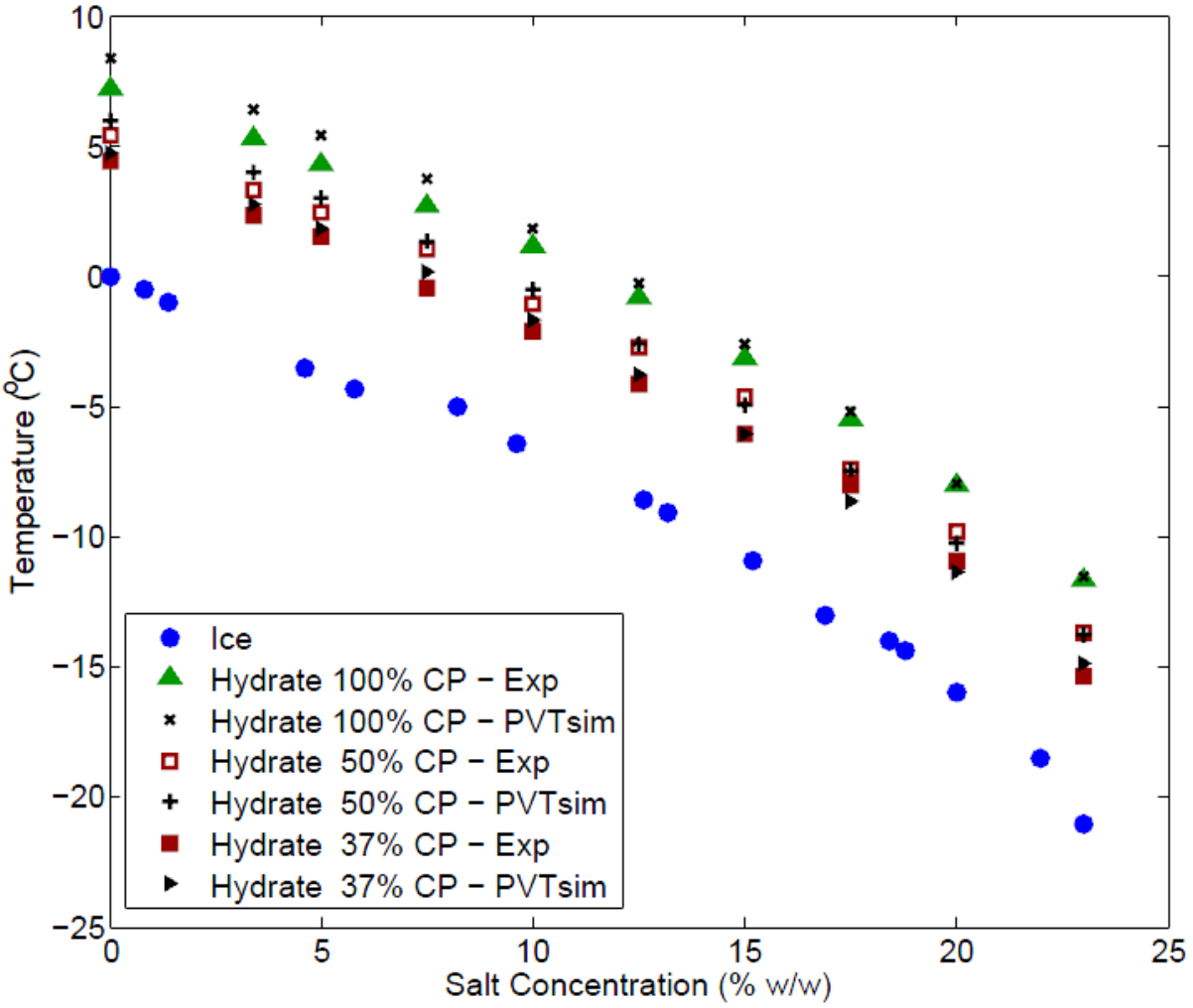

Figure 2.4: Ice [1] and experimental and simulated cyclopentane hydrate liquidus curves.

where X_{brine} is the fraction of aqueous phase remaining as brine. The equation balancing the mass of salt is $X_{hyd}X_{s-hyd} + X_{brine}X_{s-brine} = X_{s-in}$, and thus we obtain

$$X_{hyd} = \frac{X_{s-brine} - X_{s-in}}{X_{s-brine} - X_{s-hyd}} \ , \tag{2.4}$$

which can be seen as a lever rule calculation.

To illustrate the situations encountered and application of this thermodynamic data, consider figure 2.6, where point A represents a condition at which water is present only in the liquid brine phase. As the temperature is lowered, the system reaches point B, at

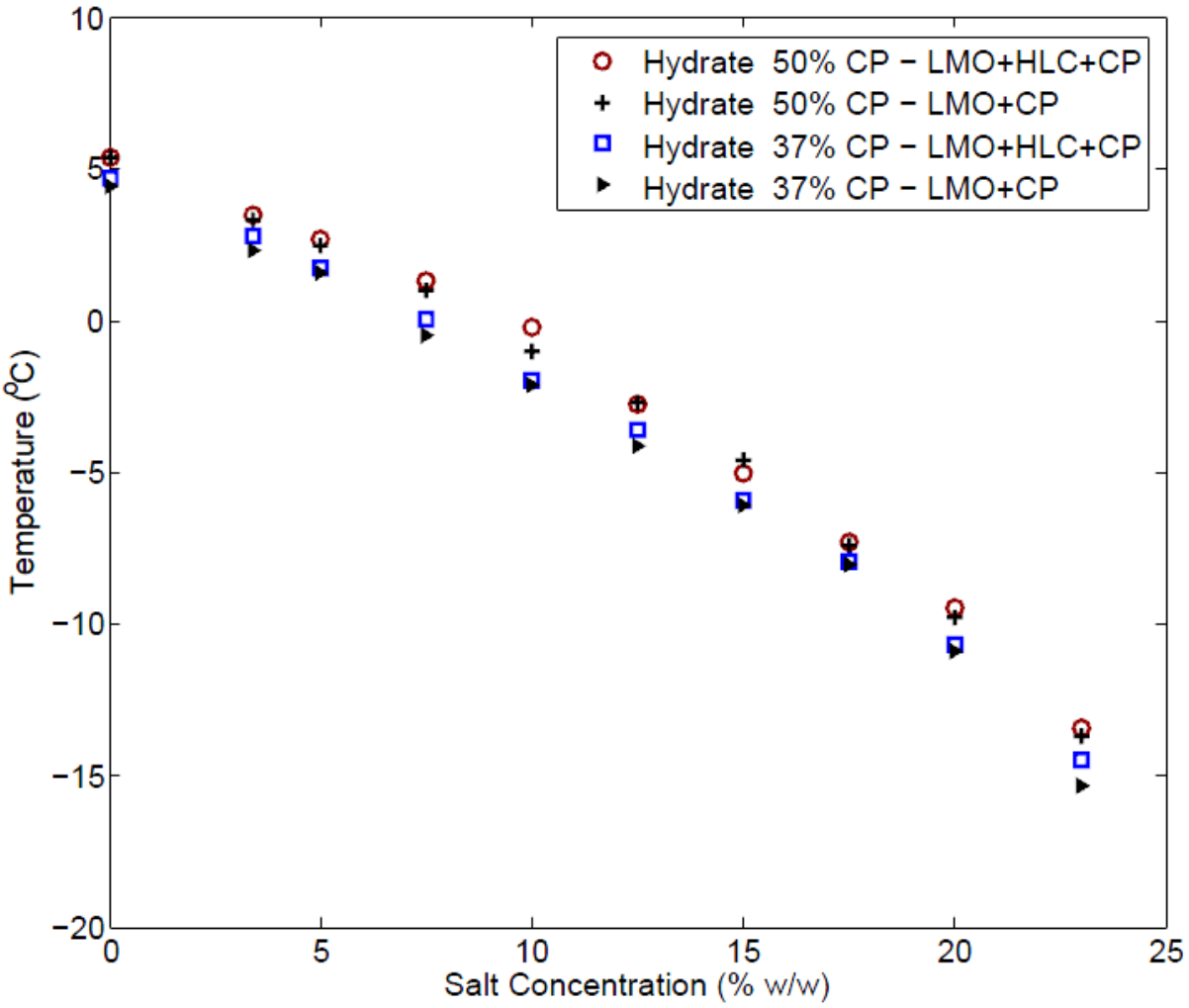

Figure 2.5: Cyclopentane hydrate liquidus curves for the 37 and 50% (v/v) cyclopentane concentrations for the simple oil phase (light mineral oil and cyclopentane (LMO+CP)) and the emulsion oil phase (light mineral oil, halocarbon 27 and cyclopentane (LMO+HLC+CP)).

which hydrate crystal formation is thermodynamically stable. With further cooling we reach point C, for which the hydrate to brine aqueous mass fraction is represented by the ratio of the length of dashed red line, $\overline{CC_b}$, to solid (blue) line, $\overline{C_hC}$. The concentration of salt in the hydrate phase is zero, while the concentration of salt in brine is the salt concentration of point C_b. As the temperature decreases, at point D, the ratio of hydrate ($\overline{DD_b}$) to brine ($\overline{D_hD}$) aqueous mass fraction increases when compared to conditions in C. The concentration of brine increases from C_b to D_b as we move from C to D.

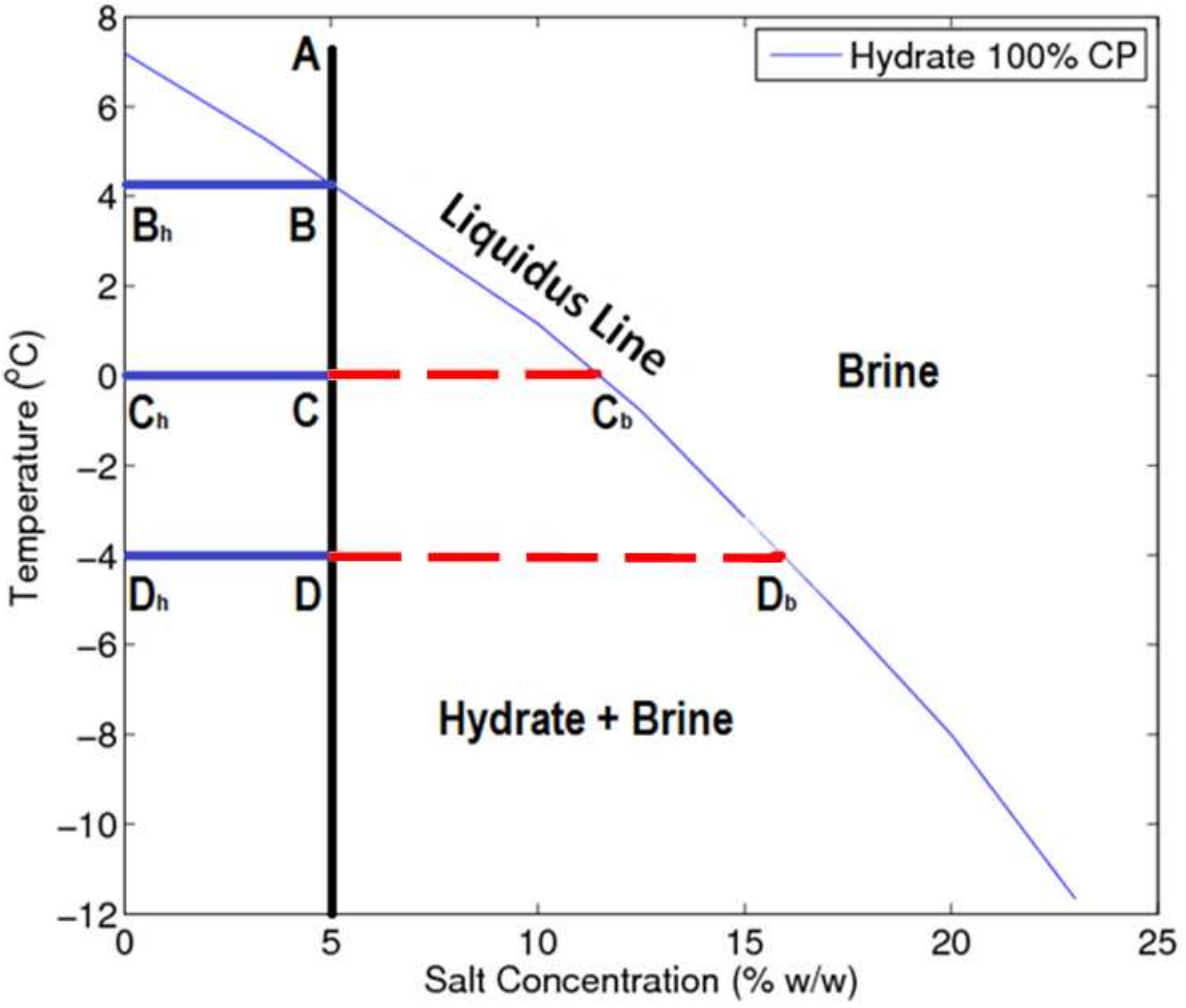

Figure 2.6: Binary phase diagram.

As noted salt is not present in the hydrate crystal ($X_{s-hyd} = 0$). Thus, for a given temperature T, the maximum conversion of water to hydrate is obtained from equations (2.2), (2.3) and (2.4),

$$X_w(T) = \frac{X_{s-brine}(T) - X_{s-in}}{X_{s-brine}(T)(1 - X_{s-in})} \ . \tag{2.5}$$

Equation (2.2) is used to calculate the conversion of water to hydrate for both the absolute upper and lower limits of cyclopentane concentration in the emulsion. The fraction of

water converted to hydrate is then weighted between the two values as

$$X_w = \left(\frac{X_{w-37} + X_{w-50}}{2}\right) X_{w-37} + \left(1 - \frac{X_{w-37} + X_{w-50}}{2}\right) X_{w-50}, \tag{2.6}$$

where X_{w-37} and X_{w-50} are the conversions of water estimated at cyclopentane concentration of 37% and 50% (v/v), respectively. Since direct measurement of equilibrium temperature is not achievable due to large changes in salt and cyclopentane concentrations in the two bulk phase experiments when Span 80 is present, an assumption of shifting the equilibrium temperature by $\Delta T = 0.54°\text{C}$, which is the shift in the equilibrium temperature of pure cyclopentane and pure water when 0.05% (v/v) Span 80 is added, is made. The difference between the theoretical conversion values when the shift in equilibrium temperature caused by Span 80 is neglected and taken into consideration by this assumption is no more than 4% as shown in Table 2.6. Furthermore, the simulated water to hydrate conversion data from PVTsim agree with our computed conversions from the experimental liquidus data (cyclopentane and light mineral oil in the oil phase) as shown in figure 2.4; in the simulation, n-octane is substituted for light mineral oil used in the experiments. In figure 2.5, a comparison of liquidus data using two different oil phases is given; the oil phase composed of light mineral oil and cyclopentane (LMO+CP), which agrees well with PVTsim, and the oil phase used in the hydrate-forming emulsion composed of light mineral oil, Halocarbon 27 (substituting approximately 53% by volume of light mineral oil in the previous case) and cyclopentane (LMO+HLC+CP). The data given in Table 2.5 and plotted in figure 2.5 for the two oil phases with and without Halocarbon 27 agree well. There is only a slight increase in cyclopentane activity due to the presence of Halocarbon 27.

Table 2.6: Thermodynamic conversion of water to hydrate in emulsion

Temperature (°C)	Salt Concentration (% w/w)	Water Conversion (%)	Water Conversion Corrected (%)
-7	0.0	100	100
	3.4	82.2	81.3
	5.0	73.4	72.2
	7.5	59.4	57.5
	10.0	44.9	42.4
	12.5	30.0	26.8
	15.0	14.3	10.7
-10	0.0	100	100
	3.4	85.5	84.0
	5.0	78.4	77.7
	7.5	67.0	66.0
	10.0	55.1	53.8
	12.5	42.7	41.2
	15.0	29.9	28.1
-13	0.0	100	100
	3.4	87.5	87.4
	5.0	81.3	81.2
	7.5	71.4	71.2
	10.0	61.0	60.6
	12.5	50.1	49.5
	15.0	38.7	37.8

2.3.2 Viscosity evolution

There is a slight increase in viscosity associated with a decrease in temperature when the emulsion is quenched from room temperature (25°C) to the desired experimental temperature [62]. Following quenching, nucleation of hydrate occurs in the emulsion. As hydrate grows, a network structure starts forming in the emulsion. The viscosity of the emulsion changes as hydrate is formed. Critical time (t_c) is defined as the onset time of sharp viscosity increase as previously described by Peixinho *et al.* [62] and described in figure 2.8 where the line fit to initial viscosity (η_{in}) intersects with the steeply-sloped line describing the viscosity evolution. Following t_c, viscosity evolves until it reaches a final value (η_f). Depending on the experimental conditions an overshoot or smooth approach to the final viscosity value may be observed. The period from critical time to the time at which viscosity initially reaches 90% of its final value is defined as the viscosity evolution time (t_e).

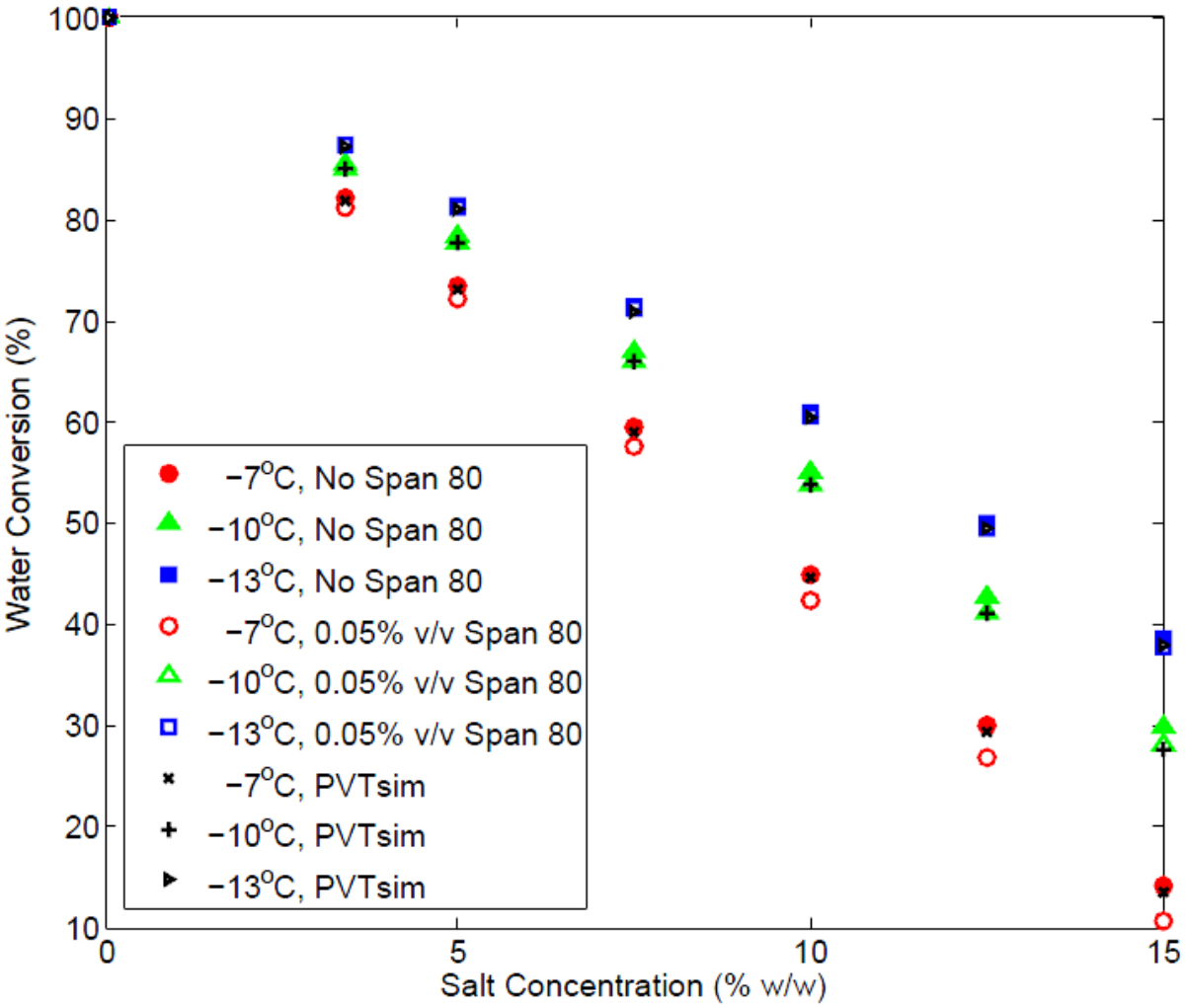

Figure 2.7: Plot of maximum water conversion to hydrate as a function of salt concentration in the aqueous phase. The computations are based on the experimental data (LMO+HLC+CP). The simulation (PVTsim) contains normal-octane as substitute to light mineral oil and Halocarbon 27 (LMO+HLC) with no surfactant.

2.3.3 Critical time

Critical time (t_c) is presumably equal to or larger than nucleation time (t_n); most likely a single nucleation site is not enough to trigger an abrupt increase in the hydrate-forming emulsion viscosity. Mechanical effects also depend on the rate of nucleation and growth of crystals from different drops connecting into a network structure. Since $t_c \geq t_n$, then critical time is affected by the nucleation time. Although stochastic in nature [81], hydrate

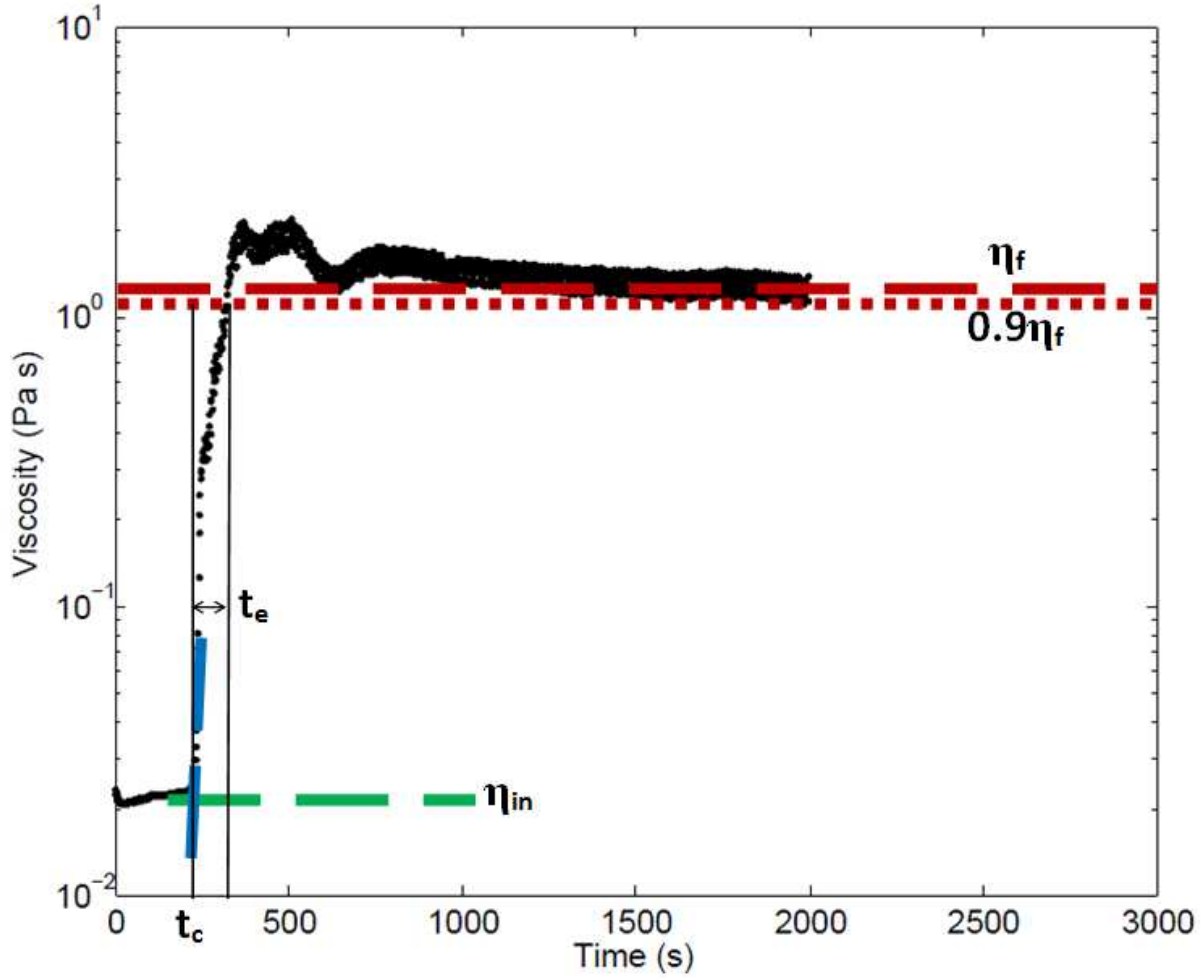

Figure 2.8: Schematic depiction of initial viscosity (η_{in}), critical time (t_{c}), evolution time (t_{e}) and final viscosity (η_{f}) of the hydrate-forming emulsion. The data shown is for a seeded hydrate-forming emulsion at $X_{s-in} = 0\%$ (w/w) salt concentration and $T =$ -13 °C (100% water to hydrate conversion).

nucleation is dependent on the level of subcooling, $\Delta T = T_{eq} - T$, in the emulsion. The presence of salt lowers the equilibrium temperature (T_{eq}) of hydrate. At lower subcooling, a larger radius of nucleation needs to be formed to allow stable crystal growth. The critical radius of nucleation allowing crystal growth is expected to be inversely proportional to the subcooling, $\Delta T = T_{eq} - T$ [86, 87],

$$R^* = \frac{2\gamma}{L_v}\frac{T_{eq}}{\Delta T}\ , \tag{2.7}$$

where γ is the energy per unit area on the crystal-liquid interface and L_v is the latent heat per unit volume of crystal. The dependence of critical time on nucleation time is substantiated in figure 2.9, where the hydrate-forming system has a lower critical time with higher subcooling.

At lower shear rate, average critical time is larger and a higher variance is observed. It is hard to distinguish whether shear rate affects the nucleation process or hydrate growth the most, although at higher shear rate droplet interaction increases. Thus, a droplet where hydrate is formed at the interface may act as nucleation site for other droplets as they come into contact enabling the growth of hydrate to increase in the emulsion.

2.3.4 Viscosity evolution time

Our data suggest that subcooling, the difference between the equilibrium temperature and the set temperature, is the main parameter affecting viscosity evolution time. Subcooling is determined by initial salt concentration because conversion has not started at the moment the hydrate-forming emulsion reaches the set temperature. Shear rate apparently does not have a significant effect on the time it takes viscosity to increase. In figure 2.10, viscosity evolution time decreases with initial emulsion subcooling. The data can be fitted to the following empirical relation,

$$t_e = Ae^{-B\Delta T} \ , \tag{2.8}$$

where t_e is the viscosity evolution time, and ΔT is the initial emulsion subcooling. Fitting coefficients A and B are given in Table 2.7.

Viscosity increase is attributed to the increase in total hydrate mass and its growth in a network structure. Thus, hydrate particle growth in the emulsion may be associated with viscosity evolution rate. A higher hydrate growth rate would result in shorter time to reach final viscosity. Uchida *et al.* also found that CO_2 hydrate growth was mainly

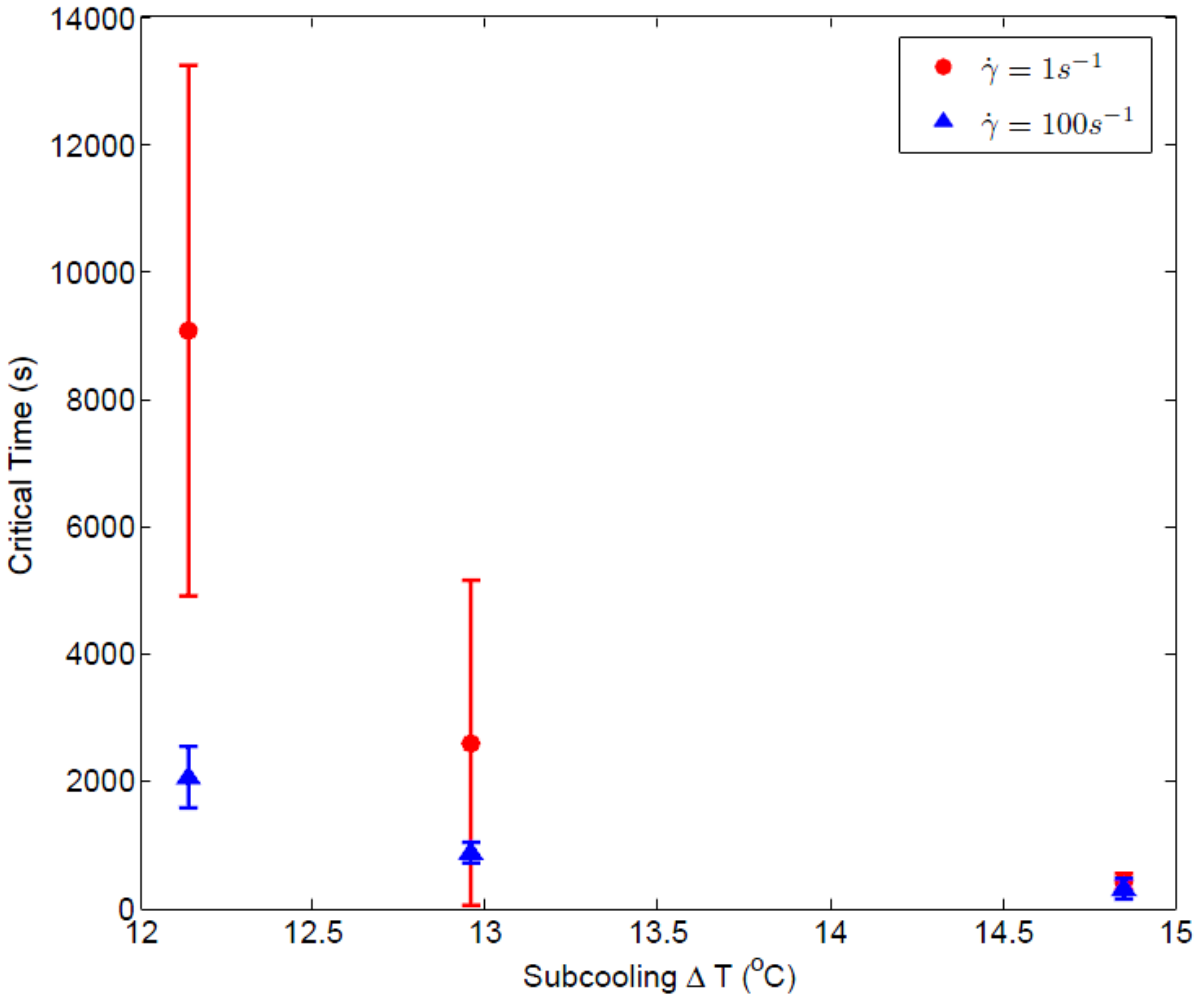

Figure 2.9: Critical time of viscosity evolution plotted as a function of the initial subcooling ($\Delta T_{in} = T_{eq} - T$) at $\dot{\gamma} = 1$ s^{-1} and $\dot{\gamma} = 100$ s^{-1} (T = -10 °C). The points left to right of each symbol correspond to initial salt concentration of X_{s-in} = 5, 3.4, 0% (w/w).

Table 2.7: Fitting coefficients for viscosity evolution time.

	Experimental Conditions		Fitting Coefficients		Coefficient of Determination
Fit Line	Temperature T (°C)	Shear Rate $\dot{\gamma}$ (s^{-1})	$A/10^4$ (s)	B ($°C^{-1}$)	R^2
(1)	-7	100	7.3	0.43	0.93
(2)	-7	1	6.3	0.37	0.85
(3)	-10	100	6.5	0.34	0.96
(4)	-10	1	7.0	0.30	0.94
(5)	-13	100	18	0.34	0.73
(6)	-13	1	3.3	0.19	0.94

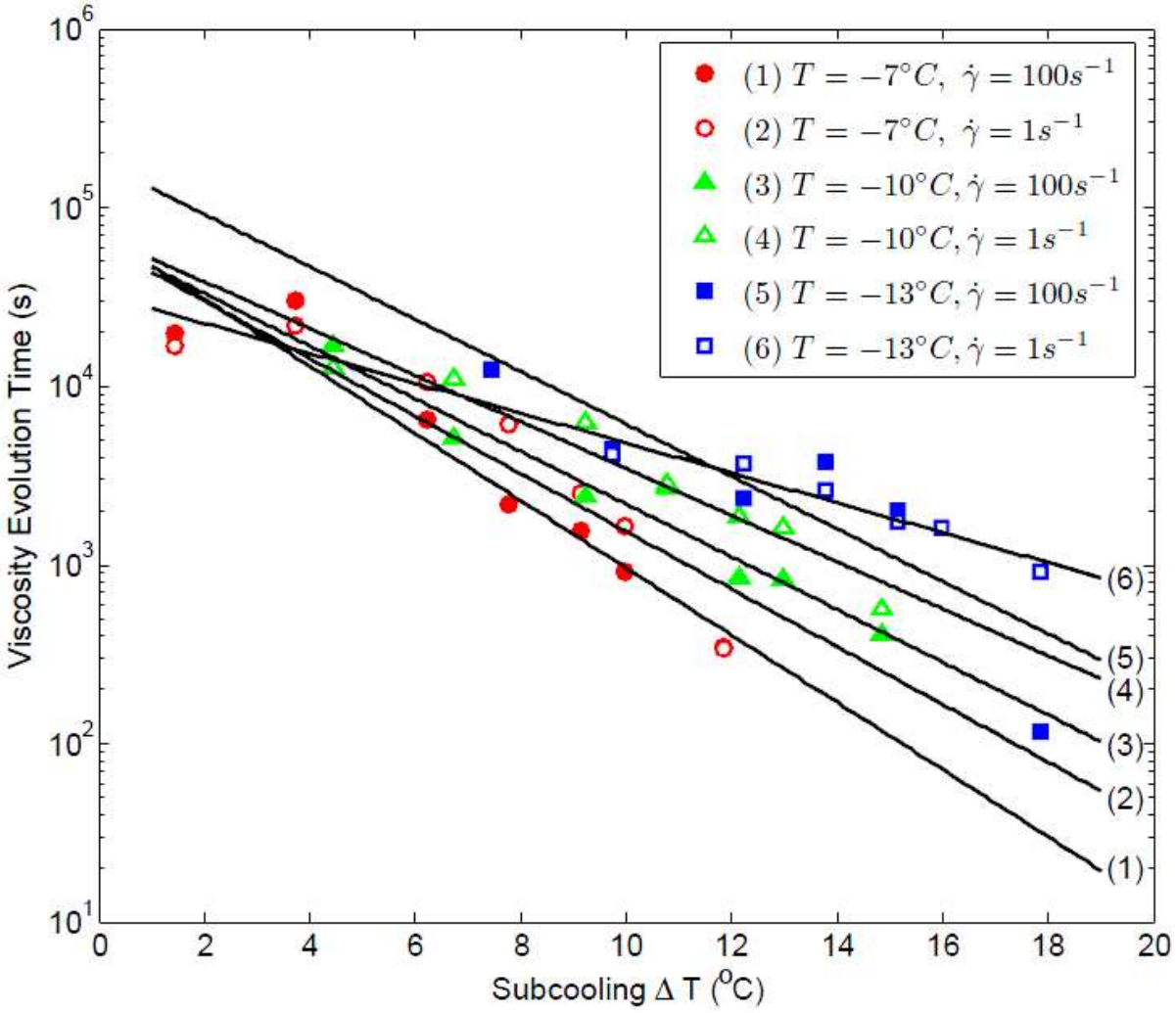

Figure 2.10: Viscosity evolution time versus the initial subcooling ($\Delta T = T_{eq} - T$) of the emulsion. Fitting coefficients for line described by equation 2.8 are given in Table 2.7.

dependent on the subcooling [56]. The dependence of hydrate growth on temperature was based on a heat-transfer-limited growth model proposed by Mori [88].

At 40% (v/v) aqueous fraction, the hydrate-forming emulsion is highly concentrated. Contact-induced agglomeration by collision of crystallizing droplets [57] under quiescent conditions is unlikely. Shear-induced aggregation is dependent on shear rate; higher shear rates result in higher number of collisions between particles [89, 90]. In our study shear rate plays negligible role on viscosity increase, indicating that collision-agglomeration is not the mechanism of hydrate-forming emulsion viscosity growth. Our data suggest

that viscosity increase in the emulsion is due to the simultaneous crystallization process of water droplets into porous hydrate particles [64, 91] and residual aqueous content forming capillary bridges binding porous particles together [5, 21, 22]. This mechanism is mainly dependent on the thermodynamic driving forces and our data suggests that subcooling plays a critical role. The strength of the network formed by this mechanism is attributed to capillary forces. Capillary forces surpass in magnitude other colloidal forces such as van der Waals and electrostatic forces [92]. Capillary bridges may also overcome weight for particles less than 100 μm (ρ_p = 3000 kg m^{-3}), consequently preventing suspension sedimentation [92, 93].

2.3.5 Viscosity after conversion

The viscosity after conversion, or final viscosity, is rather obviously dependent on the amount of hydrate present as the water in the emulsion converts. However, it is not so simple as more hydrate implies higher viscosity; this is shown by figure 2.11. The limiting component for hydrate conversion is water; cyclopentane in the oil phase is in excess. The maximum hydrate content is limited by thermodynamics. Given temperature and initial salt concentration in the aqueous phase, the thermodynamic limit on water to hydrate conversion can be calculated using equation (2.6). It is assumed that thermal conductivity and mass transfer do not ultimately prevent the hydrate-forming emulsion from reaching its final thermodynamic limit, i.e. thermodynamically-allowed conversion is attained when viscosity of emulsion reaches a final steady state value, a value considered statistically constant within instrumental measurement error. The final viscosity of the hydrate-forming emulsion is plotted as a function of the maximum achievable water to hydrate conversion in figures 2.11 and 2.12. In figure 2.11, the final viscosities of hydrate-forming emulsions with various initial salt concentrations (the points from left to right for each symbol are for X_{s-in} = 15, 12.5, 10, 7.5, 5, 3.4, 0% (w/w) at three different temperatures (T = -7, -10, -13 °C) and at two shear rates ($\dot{\gamma}$ = 1, 100 s^{-1}) are plotted.

As water to hydrate conversion increases, final viscosity reaches a maximum at 61% $\leq$ $X_w \leq$ 85%. After the peak value, there is a significant decrease in the final viscosity as conversion increases. In figure 2.12, the ultimate mixture formed from two hydrate-forming emulsions with initial salt concentrations of 1.5 and 3.4% (w/w)) are subjected to different conditions by increasing temperature (the points from right to left represent T = -13, -7.4, -0.5, 1.5, 2.4, 2.8, 3.7, 6.4 °C for 1.5% (w/w) salt concentration; and T = -10.8, -7.3, -4.2, -1.2, 1.4, 2.4, 4.8 °C for 3.4% (w/w) salt concentration). At each temperature, water conversion to hydrate is computed. At the lowest temperature, conversion of water to hydrate is at a maximum. The viscosity at maximum conversion for the initial 1.5% (w/w) salt concentration hydrate-forming emulsion (η = 11 Pa s at X_w = 94%) is lower than peak viscosity achieved at lower conversion values (η = 29 Pa s at X_w = 82%). The behavior of hydrate-forming emulsions with initial concentration of 1.5 and 3.4% (w/w) are similar; the measured peak viscosity for 3.4% (w/w) initial salt emulsion is achieved at the same level of water to hydrate conversion, $X_w \approx$ 82%.

The results in figure 2.12, in which initial salt concentration is kept fixed but temperature is varied, and figure 2.11, in which temperature is kept fixed but the initial salt concentration is different, both show that peak viscosity is achieved at intermediate conversions of X_w = 61-85%. The behavior of hydrate-forming emulsions in figures 2.11 and 2.12 suggests that cohesive forces between hydrate particles are a function of conversion. The maximum in viscosity achieved at lower conversions may be attributable to the liquid (or capillary) bridge mechanism keeping the hydrate particles in a network structure [5, 21, 22]. Similar behavior is shown in figure 2.8 where a maximum in viscosity is initially reached before the hydrate-forming emulsion attains a lower final viscosity. The apparent decrease in viscosity cannot be associated with sedimentation, which results in an increase in measured viscosity [94], but it may be a result of network reaching a lower viscosity as the water to hydrate conversion approaches 100%. If we postulate that initial conversion yields at least a shell (likely porous) on a drop which we will now term

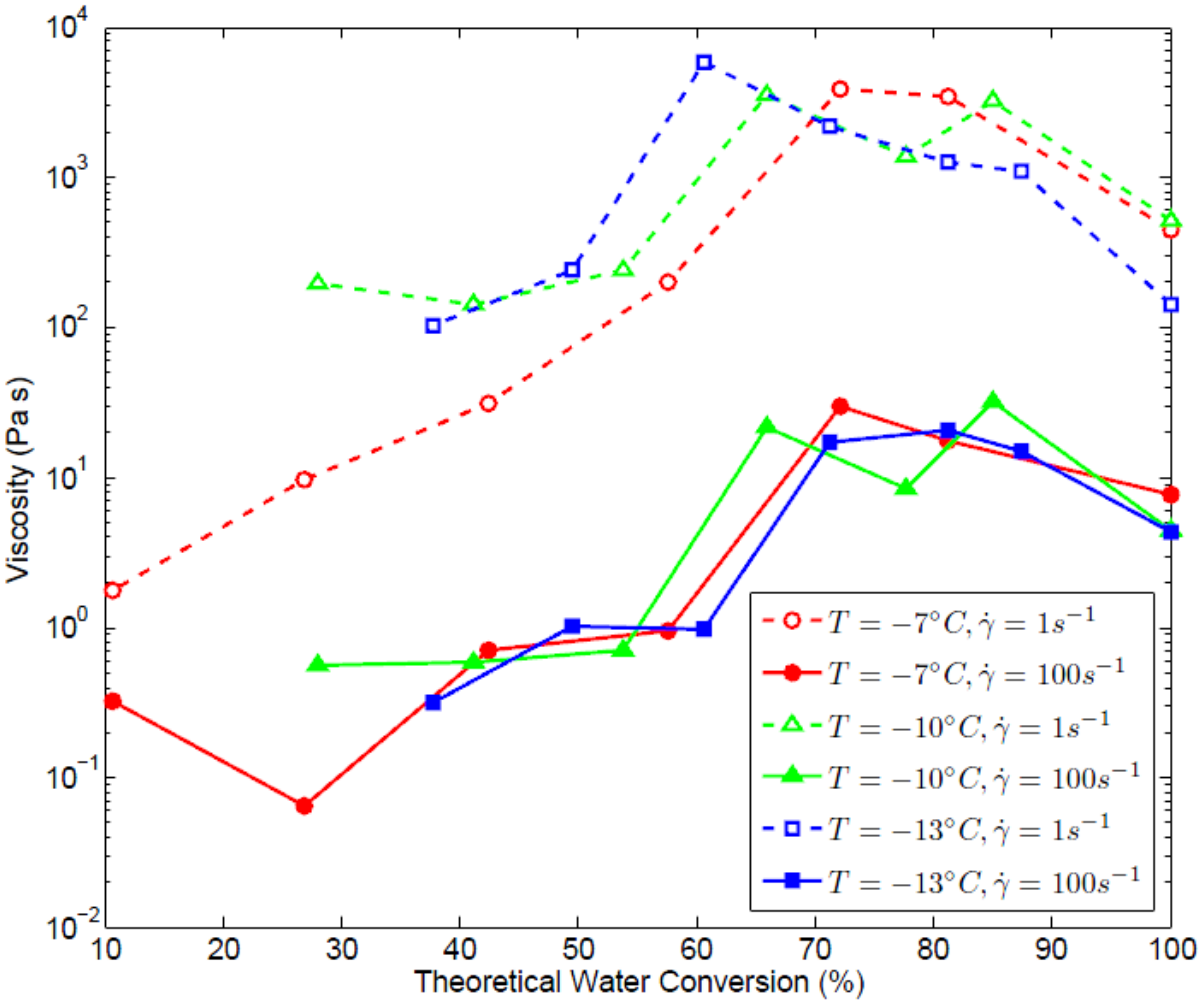

Figure 2.11: Final hydrate-forming emulsion viscosity plotted as a function of theoretical water to hydrate conversion. The points left to right of each symbol correspond to initial salt concentration of X_{s-in} = 15, 12.5, 10, 7.5, 5, 3.4, 0% (w/w).

"particle", the number of capillary bridges connecting particle surfaces becomes larger, or their size larger, as more aqueous phase remains unconverted due to thermodynamic limitations, and consequently the structural strength of the hydrate network may increase [21, 22]. In work with simpler suspensions McCulfor *et al.* [95] found that addition of small amounts of water to glass particles suspended in mineral oil significantly increases the viscosity of the suspension due to capillary bridge formation, and the viscosity of suspension went through a maximum as more water was added. A similar maximum in

viscosity due to water content has also been reported by See *et al.* in electrorheological fluids [96]. Our data suggest that a similar mechanism is affecting the viscosity of the hydrate-forming emulsion as the unconverted aqueous content, which is responsible for capillary water bridges in the complex fluid, is controlled by temperature and salt concentration.

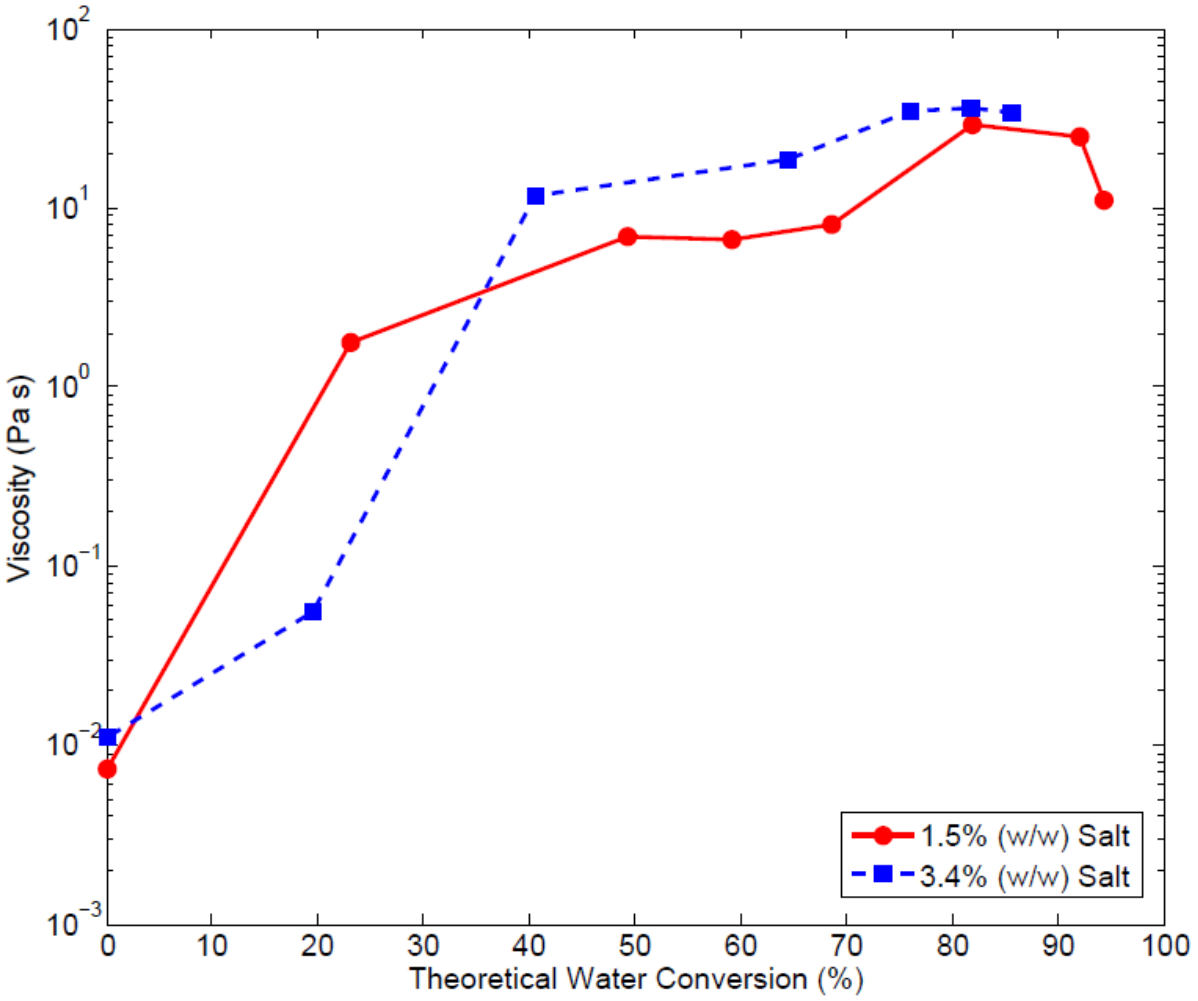

Figure 2.12: Viscosity dependence on water to hydrate conversion. Points from right to left, in which temperature is increased in the experiment, correspond to T = -13, -7.4, -0.5, 1.5, 2.4, 2.8, 3.7, 6.4 °C for X_{s-in} = 1.5% (w/w) salt concentration, and T = -10.8, -7.3, -4.2, -1.2, 1.4, 2.4, 4.8 °C for X_{s-in} = 3.4% (w/w) salt concentration. The residual aqueous phase salinity for the points from right to left correspond to $X_{s-brine}$ = 21.5, 16.2, 7.8, 4.6, 3.6, 2.9, 1.9, 1.5 % (v/v) for X_{s-in} = 1.5% (w/w) salt concentration, and $X_{s-brine}$ = 19.7, 16.2, 12.8, 9.0, 5.6, 4.2, 3.4% (w/w) for X_{s-in} = 3.4% (w/w) salt concentration. Shear rate is $\dot{\gamma}$ = 100 s^{-1}.

Capillary bridges were also found responsible for shear thinning in the work on glass particle suspensions [95]. Shear thinning [2] is observed in our hydrate suspension for all conversion levels, as shown in figure 2.13. McCulfor *et al.* [95] reported that small additions of water caused the glass particle dispersion in oil to show a highly shear thinning behavior. Capillary bridges were found to be the main cause of shear thinning behavior in that study, as surfactant addition decreased the viscosity of the glass particle suspension and less shear thinning behavior was observed. The surfactant (Span 80) lowered the interfacial tension between the oil and water phases, consequently weakening the water bridging capillary force [95]. A similar mechanism may be responsible for the shear thinning observed in our hydrate-forming emulsions, but we are unable to alter the concentration of surfactant without also altering the basic emulsion. At similar water to hydrate conversions, the 3.4% (w/w) salt concentration system residual aqueous phase has a higher salinity than the 1.5 % (w/w) system. Therefore, the apparent higher viscosity at 3.4% (w/w) salt concentration when compared to the 1.5% (w/w) salt cocentration system in figure 2.12 may be attributed to an increase in capillary bridges interfacial tension [95] caused by additional energy needed to create an ion free zone in the aqueous-oil interface at elevated salt concentrations [68].

A power law fit, known also as Ostwald-de Waele law [97], describes the viscosity dependence on shear rate of the hydrate-forming suspension in its final state:

$$\eta = K\dot{\gamma}^{n-1} \ , \tag{2.9}$$

where η is the effective viscosity of the suspension, K is the flow consistency index, $\dot{\gamma}$ is the shear rate, and $n < 1$ is the flow behavior index ($n = 1$ implies Newtonian response). No significant hysteresis is observed in figure 2.13: the hydrate-forming emulsion final structure appears to be non-thixotropic.

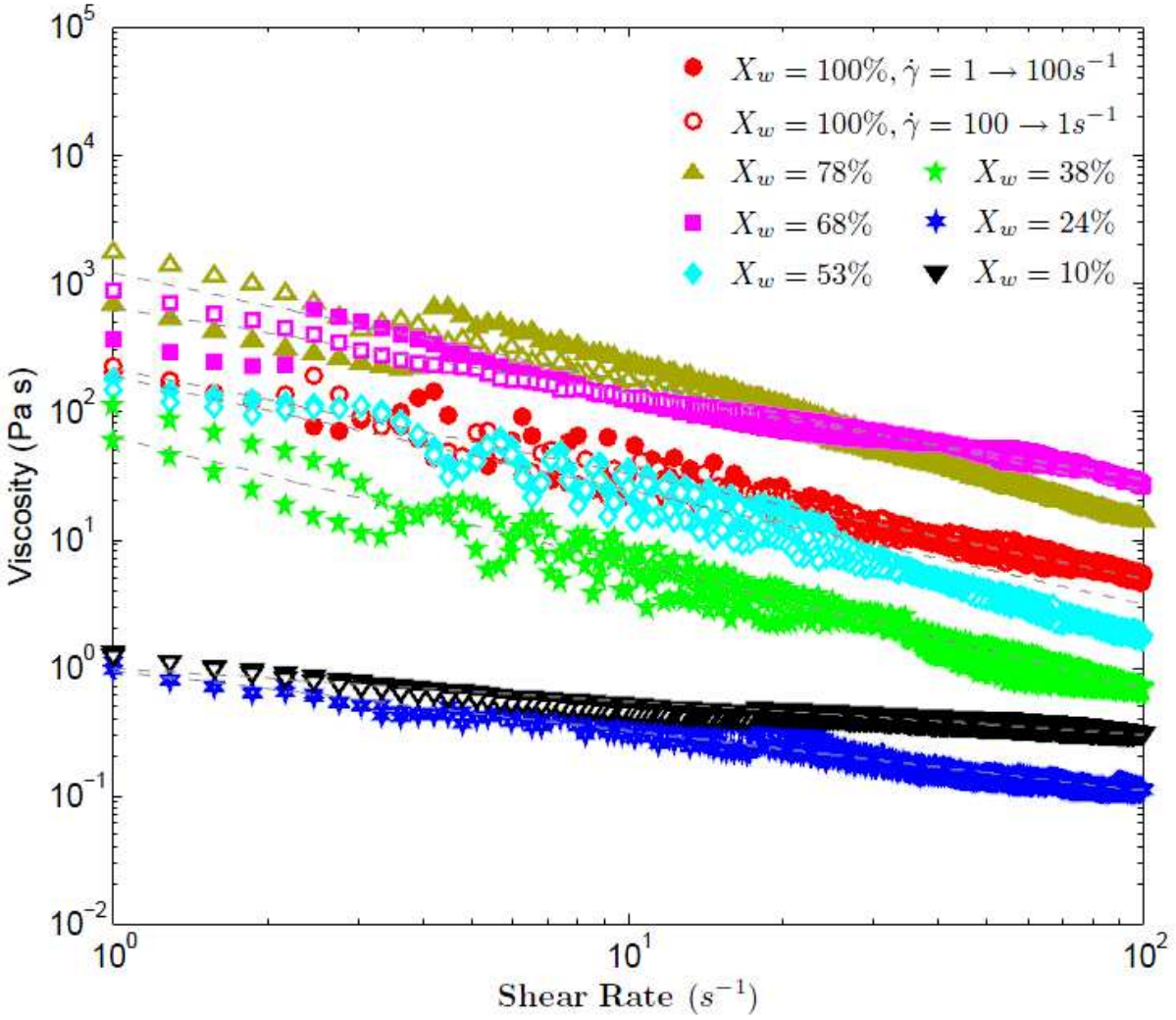

Figure 2.13: Shear thinning behavior of hydrate-forming emulsion structure formed at T = -7°C and $\dot{\gamma} = 100s^{-1}$ (closed symbols $\dot{\gamma} = 1 \rightarrow 100s^{-1}$, open symbols $\dot{\gamma} = 1 \rightarrow 100s^{-1}$).

Table 2.8: Shear thinning fit parameters.

Theoretical Water Conversion % (w/w)	Flow Consistency Index K (Pa s^n)	Flow Behavior Index n
100	220	0.18
81.3	1200	0.16
72.2	650	0.33
57.5	190	0.11
42.4	62	0.023
26.8	0.94	0.53
10.7	0.99	0.74

2.3.6 Yield stress

The minimum shear stress needed to make a suspension flowable is given by yield stress measurements [98]. Yield stress quantifies suspension network rigidity and it correlates to the magnitude of interparticle forces and the number of interparticle bonds required to be broken for the suspension to flow [98, 99]. Employing the method used by Yang *et al.* [74], yield stresses, τ_y, were measured for the final structures formed at various water to hydrate conversions shown in figure 2.14. In this method, in the logarithmic plot of shear stress versus shear rate, stress forms a plateau at low shear rates, indicating a finite stress at zero shear rate or yield stress behavior [74]. In the emulsion of 40% internal aqueous phase, at low water to hydrate conversions up to 27%, the yield stress is quite small, O (10^{-1} Pa). At higher water to hydrate conversions in the range of 42-81%, yield stress increases 1000-fold to O (10^2 Pa). The yield stress slightly increases with higher conversions in 42-81% conversion range; it reaches a maximum of $\tau_y \approx 145$ Pa at 81% conversion. At maximum theoretical conversion 100%, $\tau_y = O$ (10 Pa), an order of magnitude lower than seen at 42-81% conversion. The behavior of yield stress as a function of conversion follows a similar trend as the viscosity, and thus also suggests the influence of capillary bridges between hydrate particles. The peak yield stress of 145 Pa indicates the maximum strength of capillary bridges achievable in the studied hydrate-forming emulsion. The maximum value may be interpreted as the optimal number of bridges and particles surface needed to achieve a maximum network strength is attainable at 81% water to hydrate conversion. At lower conversions, the aqueous content availability for bridges is higher, but the hydrate particle surface area is lower. The opposite is true at higher conversions; the hydrate particle surface area is larger but the residual aqueous content to generate an optimal number of capillary bridges is insufficient.

Koos and Willenbacher reported that the addition of a second immiscible fluid to a suspension can increase the yield stress of a material by more than one order of magnitude

[100]. The presence of an immiscible fluid causes a particle suspension to transition from fluid behavior to particle network formation resulting in gel or paste properties. The authors reported that the dominant force keeping the particles in a gel state is caused by capillary bridges, with van der Waals forces having negligible contribution to the adhesion mechanism [100]. We propose that a similar behavior is seen in the hydrate suspension. The unconverted aqueous fraction serves as a binder between hydrate particles. Thus, at 100% water to hydrate conversion, where the highest content of hydrate exists, the yield stress for the material is lower than yield stress observed at $\approx 80\%$ conversion.

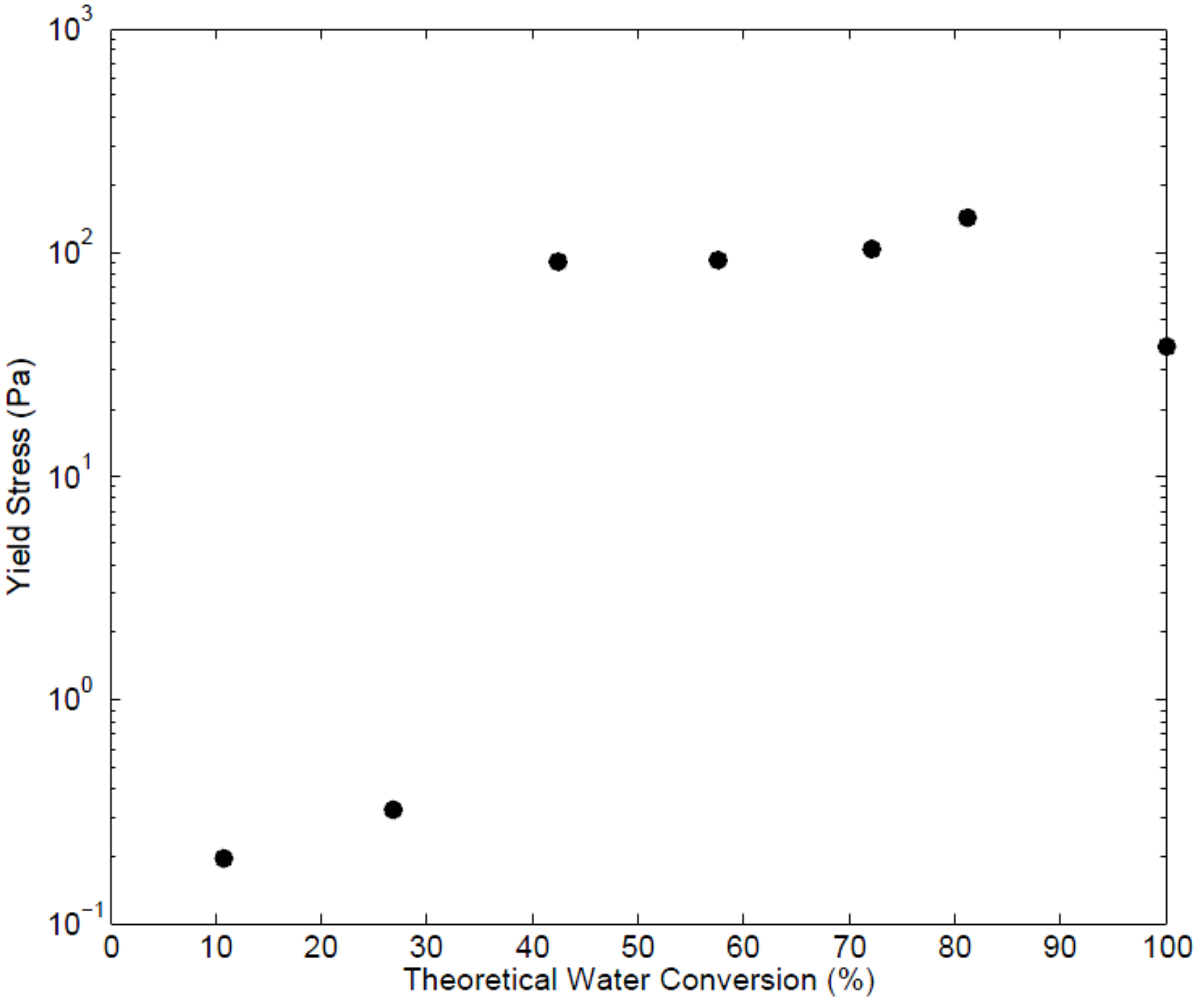

Figure 2.14: Yield stress of hydrate-forming emulsion structure formed at T = -7°C. The points left to right correspond to initial salt concentration of X_{s-in} = 15, 12.5, 10, 7.5, 5, 3.4, 0% (w/w).

2.4 Conclusion

We have analyzed the effects of salt on both the thermodynamic and rheological properties of a hydrate-forming emulsion. This has provided insight to the role of conversion of water to hydrate on the mechanical properties of the hydrate slurry formed from a water-in-oil emulsion.

Using calorimetry, specifically microDSC, we measured the equilibrium temperature of cyclopentane hydrate at various salt concentrations in the aqueous phase and cyclopentane concentrations in the oil phases. Under conditions with no surfactant, the experimental setup for the calorimetry tests was designed so that the change in salt and cyclopentane concentrations in the aqueous and oil phases remained negligible as cyclopentane hydrate formed in the interface. As salt concentration increases, the equilibrium temperature for hydrate stability is shifted to lower values, a result of chemical potential changes of water in the brine solution. Similarly, as cyclopentane concentration is decreased in the oil phase, its activity is reduced, resulting in lower equilibrium temperatures. Using the liquidus experimental data, we were able to construct a phase diagram for the hydrate-brine system. From the phase diagram, theoretical maximum water to hydrate conversions were determined as functions of temperature and initial salt concentration.

In order for water-in-oil emulsion to transition to hydrate suspension, with the observed rapid change in the mechanical properties (viscosity primarily in this work) at a critical time, nucleation needs to occur. Nucleation is highly dependent on subcooling. Our data suggests that critical time decreases with higher subcooling. In addition, critical time was found to decrease at higher shear rate. The evolution time of viscosity is found to be dependent on the subcooling effect of the hydrate forming emulsion. This observation is consistent with heat conduction limiting hydrate growth [56, 88].

Since the amount of hydrate is thermodynamically dependent on salt concentration

in the aqueous phase, final viscosity is directly affected by the salinity in the aqueous phase. The highest viscosity occurs at X_w = 61-85% (not X_w = 100%) water to hydrate thermodynamic conversion. The yield stress of the material is higher in the X_w = 42-81% range, reaching the peak yield stress at X_w = 81%. Both of these findings suggest strongly that capillary bridges affect the ultimate rheology of hydrate-forming emulsions, a factor which is critical when water conversion is limited as in brine emulsions.

3 Nucleation of cyclopentane hydrate by ice studied by morphology and rheology*

3.1 Introduction

Hydrate formation consists of two steps: 1) nucleation and 2) growth. Higher subcooling increases the rates of hydrate nucleation [6, 81, 19, 102, 103, 104, 105, 91, 106, 107] and growth [56, 108, 109, 110, 111, 112, 88, 19]. Even though hydrate growth occurs at any temperature below the hydrate equilibrium temperature ($T \leq T_{eq}$), spontaneous nucleation is highly improbable at a low subcooling where a metastable supersaturated mixture exists [6, 113]. Thus, investigating mechanisms of hydrate nucleation is crucial in understanding hydrate formation. Experiments [6, 114] and simulations [115] indicate that the site of gas hydrate nucleation is the gas-water interface. Due to low solubilities of hydrocarbon in the aqueous phase and water in the oil phase (if oil is present), nucleation is highly unlikely to occur in the bulk of either phase, but more likely at the interface where the two components of hydrate are both found at abundant concentrations. Nucleation of hydrate is a highly stochastic event [6, 81, 116, 117] and the stochastic behavior increases with smaller sample volumes [117, 118] and low subcooling [119, 120].

*The contents of this chapter are published as a paper in *Chemical Engineering Science* [101].

The influence of ice nucleation is conceptually related to what is termed the memory effect in hydrate formation. The issue raised here is that thermal history, describing a solution which at a previously lower temperature contained hydrate or ice, has been reported to shorten nucleation time and this phenomenon has been referred to as the memory effect [121, 122, 114, 123, 81]. The basic idea is that previously structured water associated with melted hydrate may play a role in nucleation of new hydrate when the system is chilled again. Two opposing views [124] exist in the scientific community for the explanation of the memory effect of hydrate: 1) the memory effect is due to residual molecular structures of water [6, 114, 125, 123, 81, 126, 119] and 2) the higher-than-equilibrium concentration of the hydrate-forming component in the aqueous phase following hydrate melting causes the memory effect [127, 124, 128, 129, 116]. Wilson *et al*. [129, 116] claim, based on data from an 'automated lag time apparatus' (ALTA), which can automatically detect nucleation and run hundreds of freeze/thaw cycles on the same hydrate-forming sample, that there is no evidence for memory effect in THF hydrate. These authors argue that the reports of memory effect can be explained in terms of stochastic behavior of heterogeneous nucleation, unmelted residual hydrate, or evolution of dissolved gas concentration in water following hydrate melting.

Addition of solids such as ice, silica particles, rust, or clay has been reported to shorten hydrate nucleation time [130, 18, 131, 132, 133]. Silica particles have been observed to reduce the stochastic nature of hydrate formation [130], rendering the process more regular. Sloan and Fleyfel [133] proposed a molecular mechanism based on labile clusters for cyclopropane gas hydrate formed from a ball mill-agitated ice. The formation mechanism of a critical nucleus through agglomeration of labile clusters has been criticized by Radhakrishnan and Trout [134] due to the large free energy that needs to be overcome during this process; these authors have instead proposed a local structuring hypothesis, in which thermal fluctuations induce rearrangement of guest molecules in a clathrate-like structure leading to nucleation. Yingming *et al.* [132] devised a novel method of

fast dichlorofluoroethane hydrate formation from the melting of ice without the need of mechanical stirring. Instantaneous hydrate formation was observed when ice melted, otherwise hydrate formation required over 16 hours when no ice was present in the reactor [132].

From the foregoing, it is clear that the onset of hydrate formation has been a topic where there is a lack of clarity regarding the role of nucleating agents, although their importance has been established. In this work, the heterogeneous nucleation of cyclopentane hydrate by ice, which is a potential candidate in hydrate-forming systems when the temperature drops low enough, is investigated experimentally. We address the zone of influence of the ice and the macroscopic consequences of ice nucleation relative to seeding by the hydrate itself. Under atmospheric pressure, cyclopentane forms the cubic hydrate sII [6], as does natural gas (but under elevated pressures), and thus it is used as a model for investigating gas hydrate behavior in an emulsion, eliminating the need for a pressurized environment. We have devised an experimental technique of observing the site of hydrate nucleation by ice. A striking dependence of a single drop conversion to hydrate on the temperature ramp rate controlling the melting rate of ice was experimentally observed. The rheological properties of hydrate-forming emulsion are investigated and compared at various subcooling following the addition of ice and hydrate seeds. Understanding the effects of ice on the evolution of hydrate-forming emulsion rheological properties is directly relevant to flow assurance. This study elucidates the mechanism by which a small quantity of ice triggers hydrate-growth in an otherwise metastable emulsion, consequently resulting in a rapid and drastic change of its mechanical properties.

3.2 Experimental

3.2.1 Materials

In the rheological experiments, 5% (w/w) sodium chloride salt (99+% pure, Fisher Scientific) is dissolved in deionized water obtained from a Millipore QTM system to form the aqueous phase. The oil phase of hydrate-forming emulsion is composed of 50% (v/v) cyclopentane (99+% pure, Fisher Scientific), while in the ice-forming emulsion cyclopentane is substituted by isooctane (99+% pure, Fisher Scientific), which does not form a hydrate structure. The rest of the oil phase in both hydrate- and ice-forming emulsions is a mixture of light mineral oil (NF/FCC Fisher Scientific) and Halocarbon 27 (polychlorotrifluoroethylene polymer, Halocarbon Products Corporation) used to match the density of the oil and aqueous phase to minimize sedimentation of the droplets in the emulsion. Sorbitan monooleate (Span 80 from Sigma-Aldrich), a non-ionic surfactant with a hydrophilic-lipophilic balance (HLB) of 4.3 [60], which does not form stable lipid bilayers in the aqueous phase [61], is used as a surfactant to stabilize the emulsion at a concentration of 0.05% (v/v) in the oil phase. The critical micelle concentration of Span 80 in the emulsion oil phase is 0.03% (v/v)[48], and we estimate based on the interfacial area per adsorbed Span 80 molecule of $\Gamma_\infty = 45$ Å [91] that the oil phase concentration of surfactant is 0.02% (v/v) after formation of the emulsion; hence, no micelle formation occurs. Relevant physical properties of the materials are provided in Table 4.1.

Table 3.1: Physical properties of materials used in this study.

Material	Chemical Formula	Mol. Weight (g mol^{-1})	Density (g cm^{-3})	Viscosity (cP)
Cyclopentane	C_5H_{10}	70.1	0.751 (25 °C)	0.44 (20 °C)
Isooctane	C_8H_{18}	114.2	0.690 (25 °C)	0.51 (22 °C)
Halocarbon 27	$(C_2ClF_3)_n$	-	1.96 (37 °C)	51 (37.8 °C)
Light mineral oil	-	-	0.83 (15.6 °C)	46 (25 °C)
Span 80	$C_{24}H_{44}O_6$	428.6	0.986 (25 °C)	1200-2000 (20 °C)
Water	H_2O	18.0	1.00 (4 °C)	1.00 (20 °C)
Sodium Chloride	NaCl	58.4	2.16 (25 °C)	-

In the single drop experiments, cyclopentane was the organic phase, and it was used in the as-delivered form (99+% pure) and with 0.05% (v/v) Span 80 surfactant. Deionized water was used for ice formation. Salt was dissolved at 5% (w/w) in deionized water to form brine.

3.2.2 Single drop experiment

A Peltier stage (Linkam LTS 120) was used to provide a well-controlled temperature environment. Images were captured using a Sony digital XCD-SX 910 camera equipped with an Edmund Optics VZM 300 Zoom imaging lens, as described previously [91]. A 1 μL aqueous drop with no salt was placed in the middle of a small well (12.5 mm in diameter and 2 mm deep) machined in an aluminum microscope slide. The minimum stage temperature attained by the apparatus is -40 °C. The experimental procedure followed was:

1. Temperature T was lowered to T_{fin} = -40.0 °C at a rate of -5.0 °C min^{-1} to induce ice crystallization of the drop previously place in the middle of the well;

2. T was held at T_{fin} = -40.0 °C until the aqueous drop fully solidified;

3. T was increased from -40.0 °C to T_{fin} = -5.0 °C;

4. T was held at T_{fin} = -5.0 °C and the ice in the well was covered with cyclopentane with 0.05% (v/v) Span 80;

5. T was increased at various rates of $\dot{T}$ = 1.0, 0.2, 5.0, 10.0 and 30.0 °C min^{-1} from -5.0 °C to T_{fin} = 0.2 °C, i..e. just above the ice melting temperature (T_{eq-ice} = 0.0 °C).

Time is measured from the onset of ice melting which starts at $T \doteq 0.0$ °C (step 5).

Utilizing the same setup except that a Navitar Zoom 7000 imaging lens is used in this case, we have investigated the nucleation of hydrate at ice-oil-aqueous phase interface following these steps:

1. Ice was formed by initially freezing 10 μL deionized water at -30.0 °C; the ice is firmly anchored at a 1 mm hole in the middle of the well;

2. at -30 °C, another 10 μL water was put on top of the ice formed in step 1, to form a taller columnar structure;

3. temperature was ramped to T = -3.6 °C;

4. at T = -3.6 °C, 0.1 mL brine at X_{s-in} = 5% (w/w) salt concentration was poured in the well to partially cover the ice as shown in figure 3.5;

5. the ice and brine in the well were covered with cyclopentane and images were recorded.

3.2.3 Rheology

Rheometric analysis was performed on density-matched 40% (v/v) aqueous fraction emulsions. Mixing of a total volume of 50 ml of water and oil to form a water-in-oil emulsion was achieved using the IKA T25 Digital Ultra-Turrax at 7000 rpm for 5 minutes. Following emulsification, 700 droplet diameters were measured for both the hydrate- and ice-forming emulsions. The droplet size was found to be $d = O(10)\mu$m for both emulsions as shown in Table 3.2. The capillary number, the ratio between the viscosity forces and the capillary forces, had maximum value $Ca_{max} = \frac{\eta_c \dot{\gamma} d}{\sigma} = O\left(10^{-2}\right)$, where $\eta_c = 0.0055$ Pa s is the continuous fluid viscosity [48], $\dot{\gamma} = 100$ s^{-1} is the shear rate, and $\sigma = O(10^{-3}$ N m^{-1}) [48] is the interfacial tension between the two phases at 0.05% (v/v) Span 80 concentration; the small value of Ca indicates droplet deformation is negligible [69]. The emulsions do not coalesce for several days, but flocculation was observed under quiescent

conditions after a few hours. The emulsions are shear thinning [62] and the disruption of flocs of drops due to shearing may be responsible for this behavior [70]. Density matching was performed to limit the effect of sedimentation, as previously discussed in detail by Zylyftari *et al.* [48], and sedimentation effects are considered negligible within the experimental times in this work.

Table 3.2: Emulsion droplet size at 5.0% (w/w) salt and 0.05% (v/v) Span 80

Emulsion	Numerical Average Mean $\frac{\sum n_i d_i}{\sum n_i}$ (μm)	Standard Deviation $\sqrt{\frac{\sum (d_i - \bar{d})^2}{N-1}}$ (μm)	Volume Mean Diameter $\frac{\sum n_i d_i^4}{\sum n_i d_i^3}$ (μm)
Hydrate-forming	10.9	11.1	53.5
Ice-forming	8.9	4.2	16.2

A volume of 25 mL emulsion was transferred to the Couette cup of the rheometer at room temperature ($T \approx 25$ °C). The cup was quickly quenched to a lower temperature. As soon as the emulsion temperature reached the desired temperature, it was seeded with five ice/hydrate crystals of approximately 1 mm in diameter placed on the upper surface of the emulsion, specifically on the layer covering the inner cylinder in the Couette geometry. All seeds are placed within 10 s, which is well below the minimum experimental uncertainty of $O(10^2$ s). Immediately after the seeds were placed in the rheometer, shearing was started. Onset of shear was defined as taking place at $t = 0$ s.

A strain controlled rheometer (ARES-G2) with Couette geometry was used to measure properties of the hydrate- and ice-forming emulsions. This rheometer is equipped with a force rebalance transducer (FRT). The software automatically switches between the three ranges of measurement, and this is observed to occur under certain of the conditions studied here. The cup diameter was 30 mm. The bob diameter was 28 mm with a length of 42 mm, yielding a 1 mm gap between the concentric cylinders. Temperature control was achieved through the Advanced Peltier System (APS), with temperature measured by a thermocouple in contact with the cup. The emulsions were sheared at constant rate of $\dot{\gamma} = 100$ s^{-1} until the measured viscosity reached a steady value.

3.3 Results and discussion

3.3.1 Conversion time

Crystal morphology evolution was investigated under various temperature ramp rates plotted in figure 3.1: $\dot{T} \equiv dT/dt$ = 0.2, 1.0 (figure 3.2(b-c)), 5.0 (figure 3.2(e-g)), 10.0 and 30.0 (figure 3.2(h-j)) °C min^{-1} for the case of no salt (X_{s-in} = 0% (w/w)) and 0.05% (v/v) Span 80 in cyclopentane. Once the temperature reached T = 0.2 °C, the experiment was held fixed at this temperature. Conversion time (t_{cv}) is defined as time after passing T = 0.0 °C, and thus when ice melting and hydrate formation starts [64] (t = 0 s), until water to hydrate conversion is complete. The temperature ramp and hold protocol is shown schematically in figure 3.1.

Conversion time was found to be quite strongly dependent on temperature ramp rate, $\dot{T}$, as plotted in figure 3.4. The minimum conversion time, t_{cv} = 228 ± 81 s, from the various ramp rates studied here was observed at $\dot{T}$ = 1.0 °C min^{-1}. At a significantly lower temperature ramp rate, $\dot{T}$ = 0.2 °C min^{-1}, conversion time (t_{cv} = 385 ± 205 s) was higher. At higher temperature ramp rates $\dot{T}$ = 5.0, 10.0, and 30.0 °C min^{-1}, conversion time increases with the ramp rate. The conversion time at $\dot{T}$ = 30.0 °C min^{-1}, t_{cv} = 4610 ± 3030 s, is 20 times the minimum observed conversion time at $\dot{T}$ = 1.0 C min^{-1}. Temperature ramp rate determines the heat rate entering the hydrate forming system; thus, the fraction of unmelted ice at $T \geq 0$ °C decreases with higher temperature ramp rates.

Based on these observations, we propose that at lower temperature ramp rates, there is more unmelted fragmented ice [132]. A portion of the ice is at the oil-aqueous phase interface as shown in figure 3.2(b),(e),(h) and figure 3.3(a). These results indicate that the ice at the oil-aqueous phase interface is providing an ice-oil-aqueous (IOA) phase contact line where hydrate nucleation is favorable. At low temperature ramp rates as shown in figure 3.2(b) and figure 3.3(a), there is a greater length of IOA contact line, providing more

heterogeneous nucleation sites for hydrate formation. Under these conditions, we observe the formation of a large number of small crystals, whereas at higher temperature ramp rates, less ice is present as shown in figure 3.2(h), and thus less IOA hydrate nucleation sites are available. The high ramp rate condition gives rise to a few large crystals as shown in figure 3.3(c). It is important to note that when the single drop experiment is run at isothermal conditions of $T = 0.2$ °C, without prior formation of ice (i.e., no IOA contact line), no hydrate formation is observed for $t = 5$ h (at which time the experiment was ended). This indicates the rarity of homogeneous nucleation [135, 114, 136] and the crucial role of ice in the interfacial region to heterogeneously nucleate hydrate.

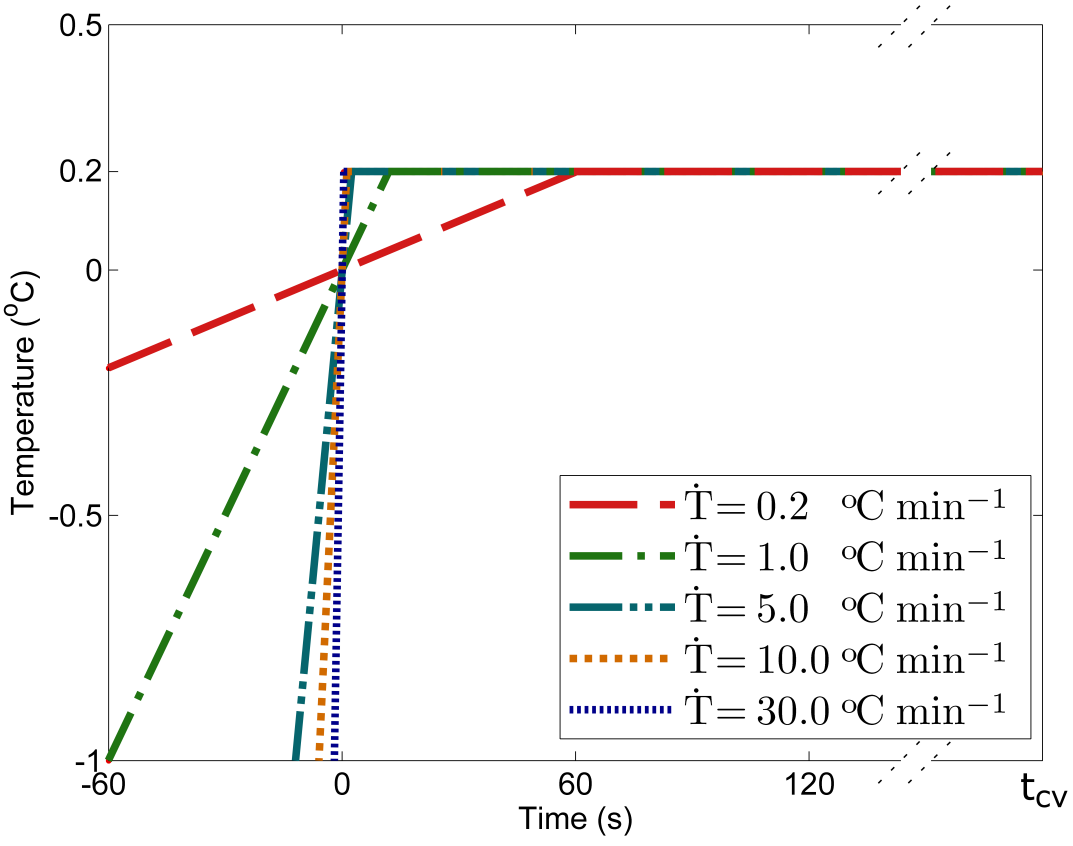

Figure 3.1: Experimental temperature profiles. Conversion time (t_{cv}) is measured from when temperature reaches $T = 0.0$ °C and ice starts to melt until the whole drop has converted to hydrate.

The observed higher conversion time at $\dot{T} = 0.2$ °C min^{-1} compared to the conversion time at $\dot{T} = 1.0$ °C min^{-1} is believed to be associated with a limiting amount of free water available from ice melting and not with a shortage of IOA nucleation sites. By contrast, at higher temperature ramp rates, $\dot{T} \geq 5.0$ °C min^{-1}, free water is visibly abundant; see figures 3.2(e),(h),(i) and 3.3(b),(c). Since the subcooling at the hold temperature of $T = 0.2$ °C was the same for all temperature ramp rate experiments, $\Delta T \doteq 6.4$ °C [48] ($T_{eq-hyd} = 6.6$-7.7 °C [48, 82, 33, 83, 123, 137]), the increase in conversion time indicates the effect of heterogeneous nucleation of hydrate by ice on the overall conversion rate. It is not related to the crystal growth rate which is dependent on subcooling [91, 54, 56, 112, 108, 109, 110, 111]. The dependence of water drop conversion to hydrate on the number of primary crystals is more evident in figure 3.2(i), where during the first 2850 s, a few crystals grow at the interface. After the immersion of significant hollow-conical hydrate crystals in the aqueous phase as described by Karanjkar *et al.* [91], other crystals may form at the interface and this causes the drop conversion to complete at 6475 s. The amount of hydrate conversion is negligible during the earlier stage when a few crystals grow at the interface, but the submerged crystals may induce secondary nucleation [113, 138, 139]. The observations here thus indicate that the net three phase (IOA) contact line length increases with the concentration of unmelted fragmented ice at lower temperature ramp rates. This results in an increased heterogeneous nucleation rate of hydrate, which decreases the time to full conversion of water to hydrate. Since only ice is melted and not hydrate during the temperature ramp step ($T_{eq-ice} < T_{fin} < T_{eq-hyd}$), the melt is not supersaturated with cyclopentane. Thus, supersaturation of melt with the hydrate-forming component (cyclopentane in our experiment) [127, 128] is not a basis for fast hydrate nucleation. Furthermore in all experiments, hydrate crystals are seen when some ice is still present. Thus, the observations are not related to a possible memory effect mechanism. These observations lead to a further examination of the role of ice in interfacial nucleation.

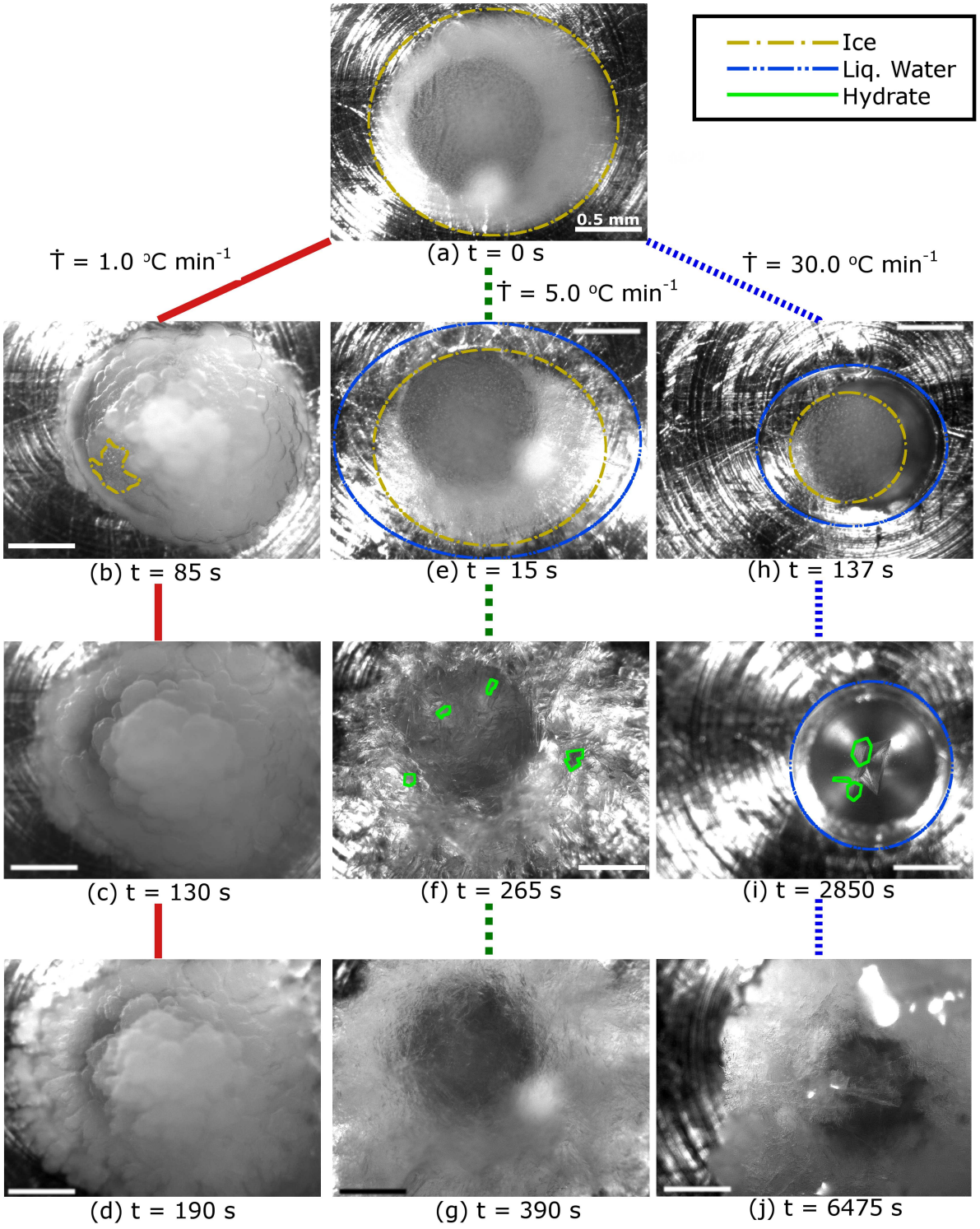

Figure 3.2: a) Initial ice ball: common structure for all conditions. Images of hydrate growth at temperature ramp rates of $\dot{T}$ = (b-d) 1.0, (e-g) 5.0, (h-j) 30.0 °C min^{-1} at 0.05% (v/v) Span 80 and no salt, scale bar = 0.5 mm. Final temperature T_{fin} = 0.2 °C (ΔT = 6.4 °C). Thermodynamically-allowed conversion of water to hydrate is X_{w-hyd} = 100%.

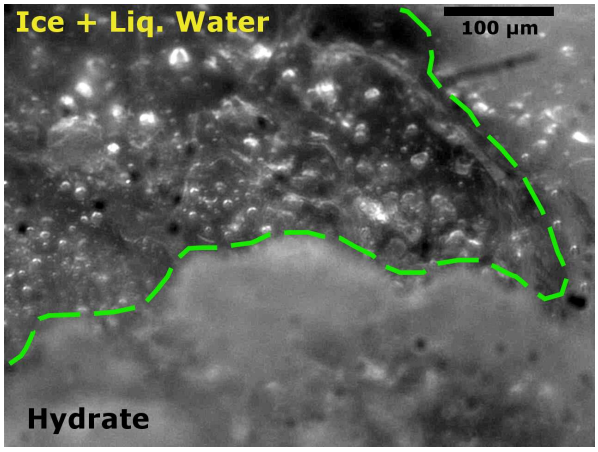

(a) $\dot{T} = 0.2$ °C min^{-1}, $t = 81$ s

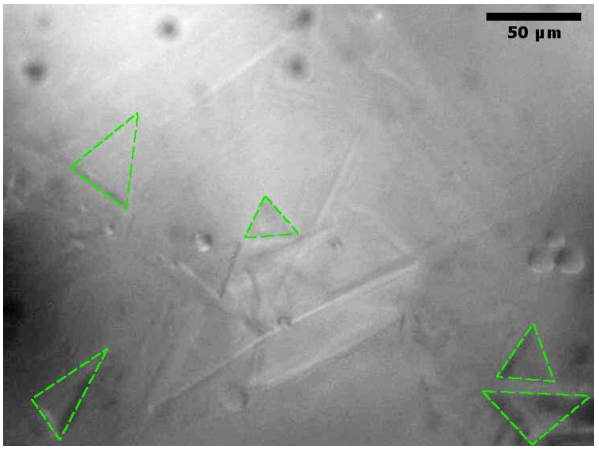

(b) $\dot{T} = 5.0$ °C min^{-1}, $t = 218$ s

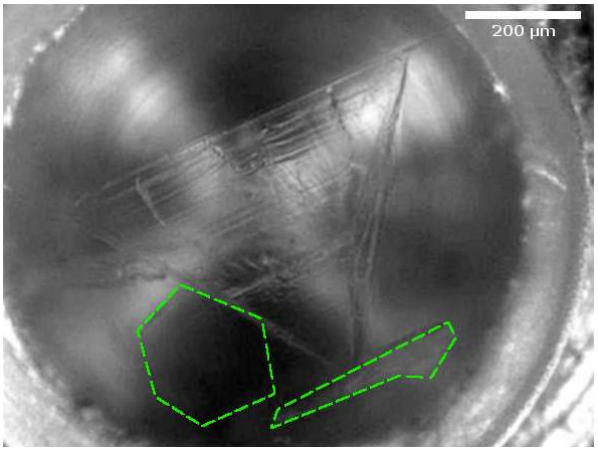

(c) $\dot{T} = 30.0$ °C min^{-1}, $t = 5930$ s

Figure 3.3: Primary hydrate crystals at temperature ramp rates of $\dot{T}$ = (a) 0.2, (b) 5.0, (c) 30.0 °C min^{-1} at 0.05% (v/v) Span 80 and no salt. Final temperature $T_{fin} = 0.2$ °C (ΔT = 6.4 °C). A few representative crystals are highlighted in (b) and (c) to indicate the typical size.

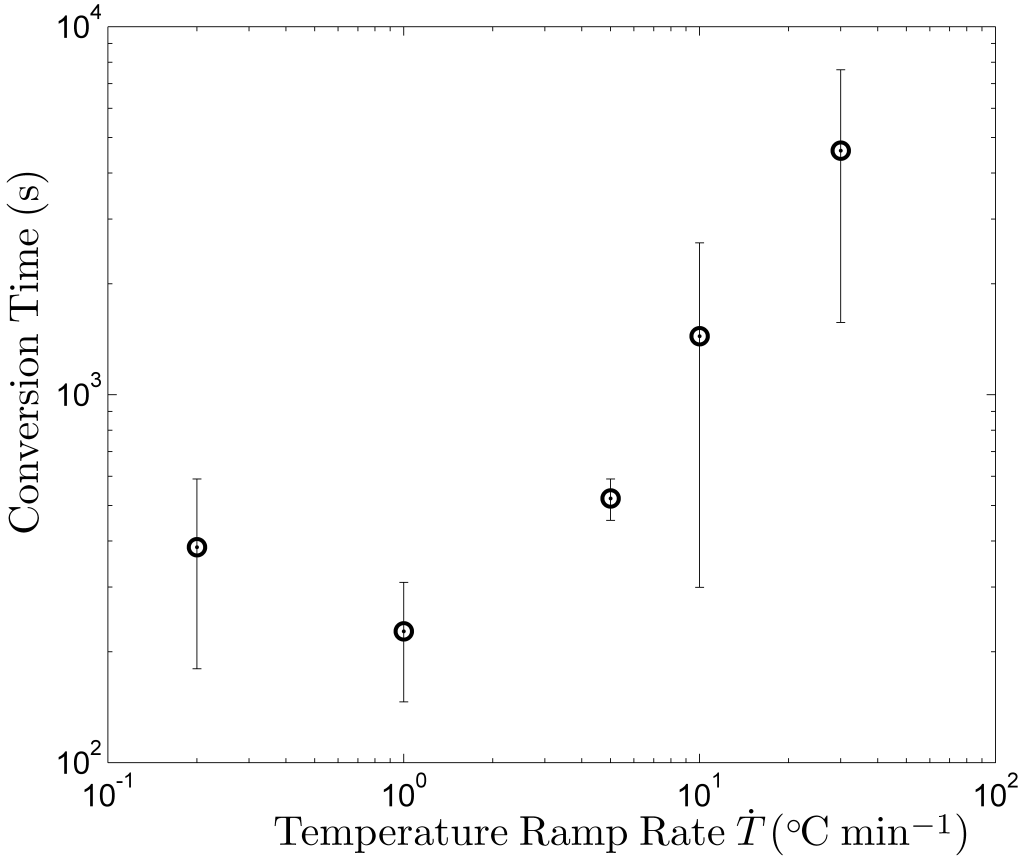

Figure 3.4: Conversion time dependence on temperature ramp rate at 0.05% (v/v) Span 80 and no salt. Final temperature T_{fin} = 0.2 °C (ΔT = 6.4 °C). Thermodynamically-allowed conversion of water to hydrate is X_{w-hyd} = 100%.

3.3.2 Hydrate nucleation at the ice-oil-aqueous phase contact line

The experimental setup for examination of nucleation of hydrate by ice at an oil-aqueous phase interface is shown in figure 3.5. Initially ice is formed in a columnar structure at the center of the aluminum plate. Brine at a salt concentration of $X_{s-in} = 5\%$ (w/w) is added at its ice-brine equilibrium temperature of T_{eq-ice} = -3.6 °C, partially covering the ice as shown in 3.5(b) so that the ice protrudes above the brine. Under these conditions no net ice formation or melting is thermodynamically allowed and a slight increase or decrease in temperature can be re-equilibrated with only a small phase change. Pure cyclopentane without surfactant is added to the ice-brine system, forming the IOA contact line.

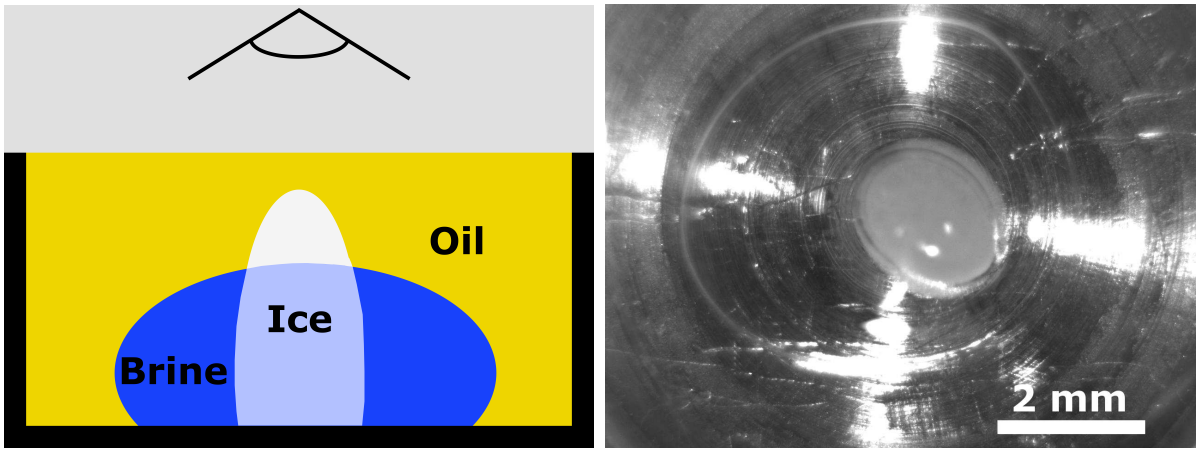

(a) schematic (b) ice, brine and oil

Figure 3.5: Setup of the experiment probing heterogeneous nucleation of hydrate by ice at the ice-oil-aqueous (IOA) contact line. Aqueous phase salt concentration is $X_{s-in} = 5\%$ (w/w) and the temperature is at T_{eq-ice} = -3.6 °C, where ice is at equilibrium with the brine.

Hydrate nucleation by ice followed by its growth at the aqueous-oil interface is shown in figure 3.6. Hydrate crystals are observed to initiate at the IOA contact line in figures 3.6(a)-(e). These crystals enable growth and complete coverage of the oil-aqueous phase interface as shown in figures 3.6(f). As no surfactant is present, hydrate growth is limited to the interface where it grows as a shell as reported by Karanjkar *et al.* [91] and

the shell limits the conversion of water to hydrate as verified through differential-scanning calorimetry by Zylyftari *et al.* [48].

The heterogeneous nucleation may occur according to the induce-promote-nucleate (IPN) mechanism at an ice interface as proposed by Pirzadeh *et al.* [140]. In this mechanism the hydrate-former component, here cyclopentane, may migrate to the ice and induce structural defects [141] and promote cage formation around the cyclopentane which finally nucleates into a hydrate. The solubility of cyclopentane in water in mole fraction is $O(10^{-5})$ [142, 143] and the mole fraction of water in cyclopentane is $O(10^{-4})$ [142]. A schematic density profile of each component in the oil and aqueous phases is shown in figure 3.7. Since cyclopentane is abundant in the bulk oil and sufficiently concentrated at the water-oil interface, heterogeneous nucleation of ice is favorable in these regions according to the IPN mechanism [140]. However, neither the bulk oil nor the aqueous phase favor hydrate growth due to low solubility of the complementary component. Thus, the only region where an optimal concentration (comparable to the 1:17 cyclopentane to water ratio [77] for fully occupied large cages) exists is at the oil-aqueous phase interface, whose length scale is $\lambda = O$ (1 nm) [144, 145, 146] as shown in figure 3.7. Furthermore, our observations indicate that in fact the oil-aqueous phase interface is the region where hydrate heterogeneous nucleation by ice occurs and subsequent growth occurs.

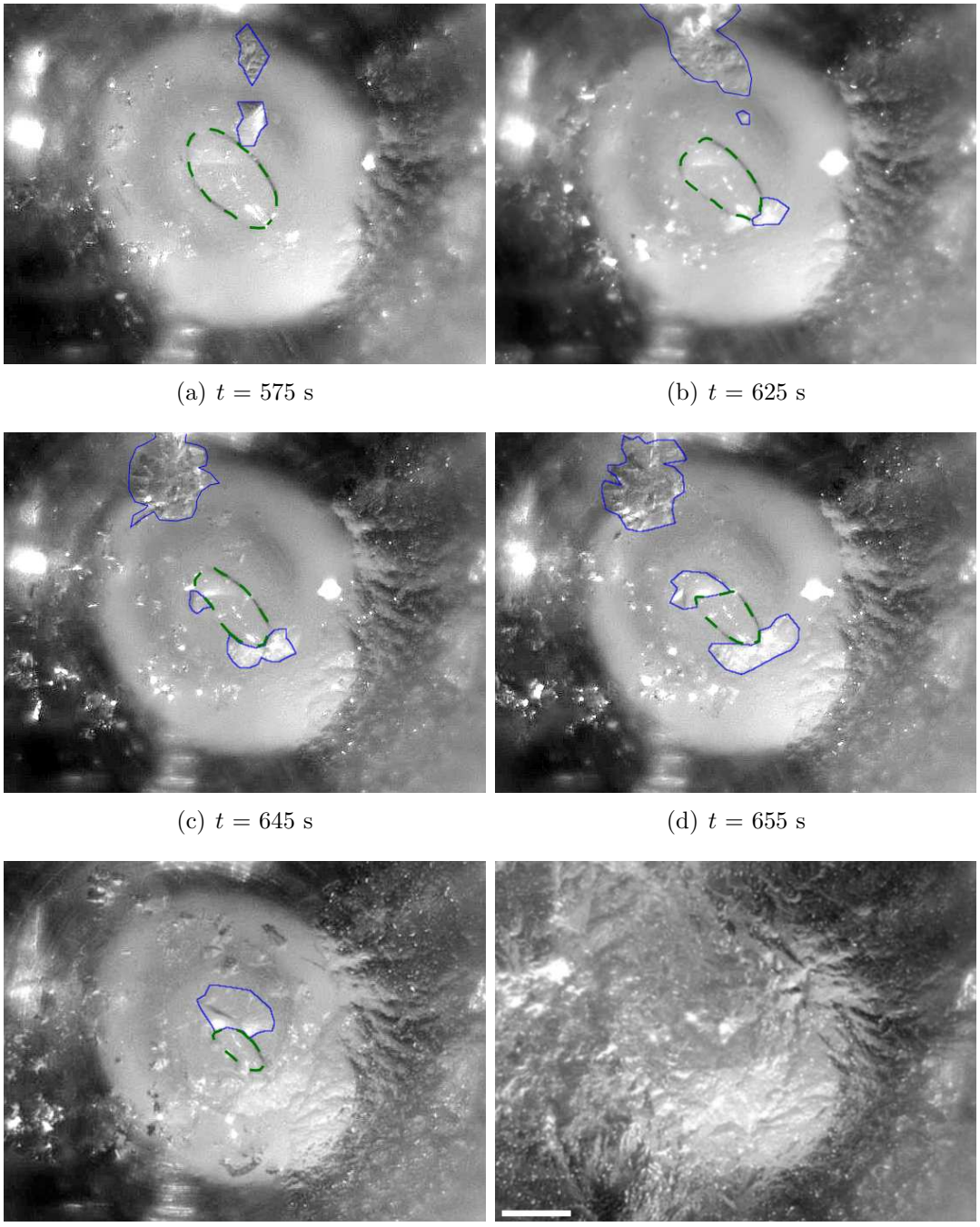

(a) t = 575 s (b) t = 625 s

(c) t = 645 s (d) t = 655 s

(e) t = 700 s (f) t = 1270 s

Figure 3.6: Heterogeneous nucleation of hydrate by ice at the oil-aqueous phase interface. The scale bar = 500 μm. Aqueous phase salt concentration is X_{s-in} = 5% (w/w) and the temperature is set to T_{eq-ice} = -3.6 °C. The ice-organic-aqueous (IOA) contact line is shown by the dashed (green) line, while the solid (blue) line highlights selected hydrate crystals.

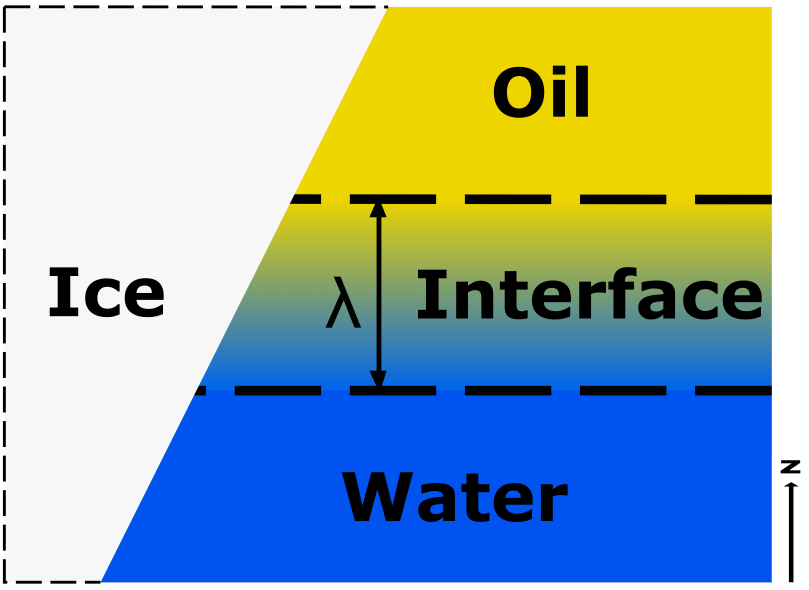

(a) Ice-oil-water contact point, $\lambda = O$ (1 nm) [144, 145, 146]

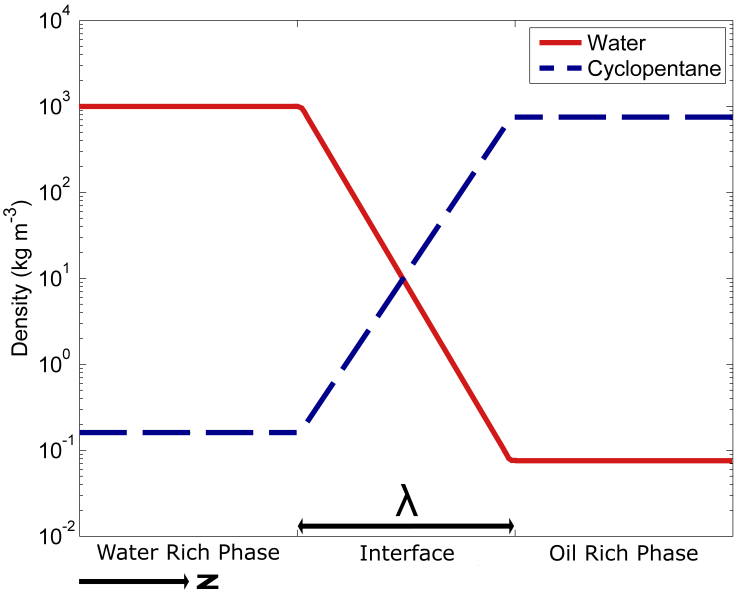

(b) Hypothetical cyclopentane and water density profile based on solubility [142, 143]

Figure 3.7: Schematic of (a) the ice-oil-water (IOA) contact region and (b) concentration profiles at the interface.

3.3.3 Rheometry: critical time dependence on hydrate nucleation and growth

We now consider how ice-induced nucleation affects the mechanical property evolution in hydrate-forming emulsions. The hydrate-forming emulsion is ice-seeded in the rheometer as depicted in figure 3.8; seeding is immediately followed by the onset of shear at $\dot{\gamma} = 100$ s^{-1}, at time $t = 0$ s. Following seeding, the critical time, denoted t_c and defined as the time after seeding where an abrupt jump in viscosity is observed as described by Peixinho *et al.* [62] and Zylyftari *et al.* [48], is measured as shown in figure 3.9. Without seeding, no jump in viscosity is observed for $t = 60000$ s (16.7 hours); see figure 3.10. After ice seeds are placed at $t = 60000$ s, a jump in viscosity is observed approximately 5000 s later, as can also be seen in figure 3.10. The initial decrease in viscosity between $t = 60000$ s and $t = 65000$ s is puzzling, but may be associated with the ice seeds breaking the flocculation of droplets which may have risen [48] in this very extended duration experiment. This rising and flocculation is most likely responsible for the observed slow increase in viscosity during the first 60000 s. The lack of an observable jump in viscosity in the metastable hydrate-forming emulsion without seeding is understandable based on small hydrate homogeneous nucleation rates at low subcooling [135, 114, 136].

Since cyclopentane hydrate is found to only form at the oil-aqueous phase interface, where both cyclopentane and water are in sufficient concentrations, whereas ice can form in the bulk aqueous phase, there is a competition between hydrate and ice formation for the available water in the emulsion (provided the temperature is below the ice melting temperature). The thermodynamically-allowed water to hydrate or ice (i.e., assuming only ice formation) conversions are given in Table 3.3, based on data of Zylyftari *et al.* [48]. At the smallest subcooling for which we have presented data, $\Delta T = 4.3$ °C, the water to hydrate conversion is $X_{w-hyd} = 51\%$, while at the highest subcooling $\Delta T = 7.3$ °C conversion is $X_{w-hyd} = 66\%$, and thus there is no more than 15% increase in conversion.

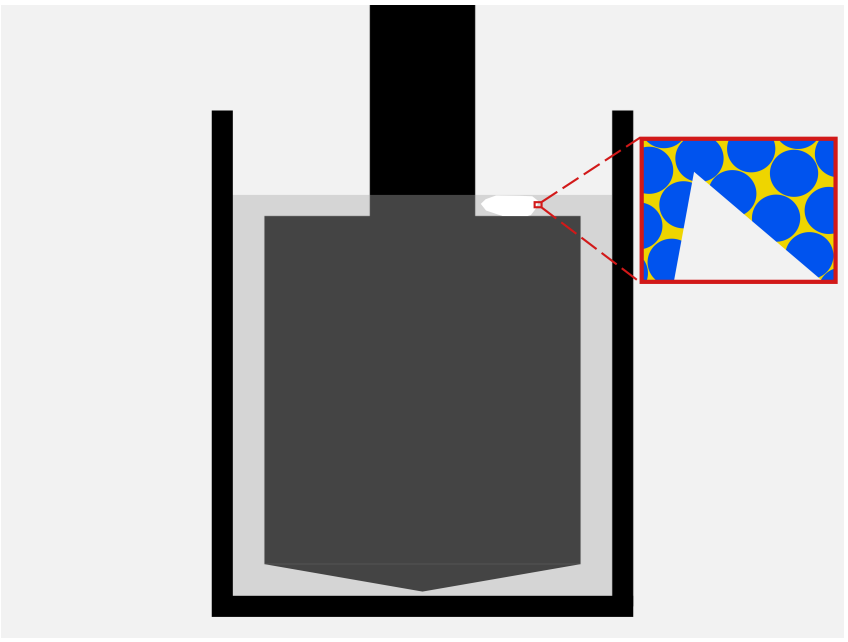

(a) Schematic of a seeded emulsion in the rheometer

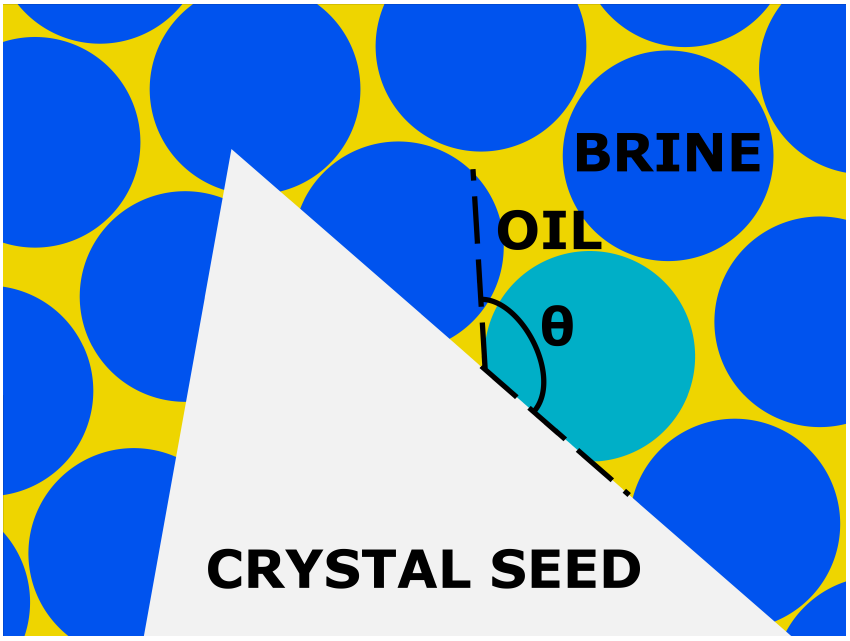

(b) Crystal seed and the droplets in the emulsion; highlighting of one drop is used only to describe the contact angle.

Figure 3.8: Schematic of (a) an emulsion seeded in the rheometer and (b) the contact angle between a droplet and the crystal seed.

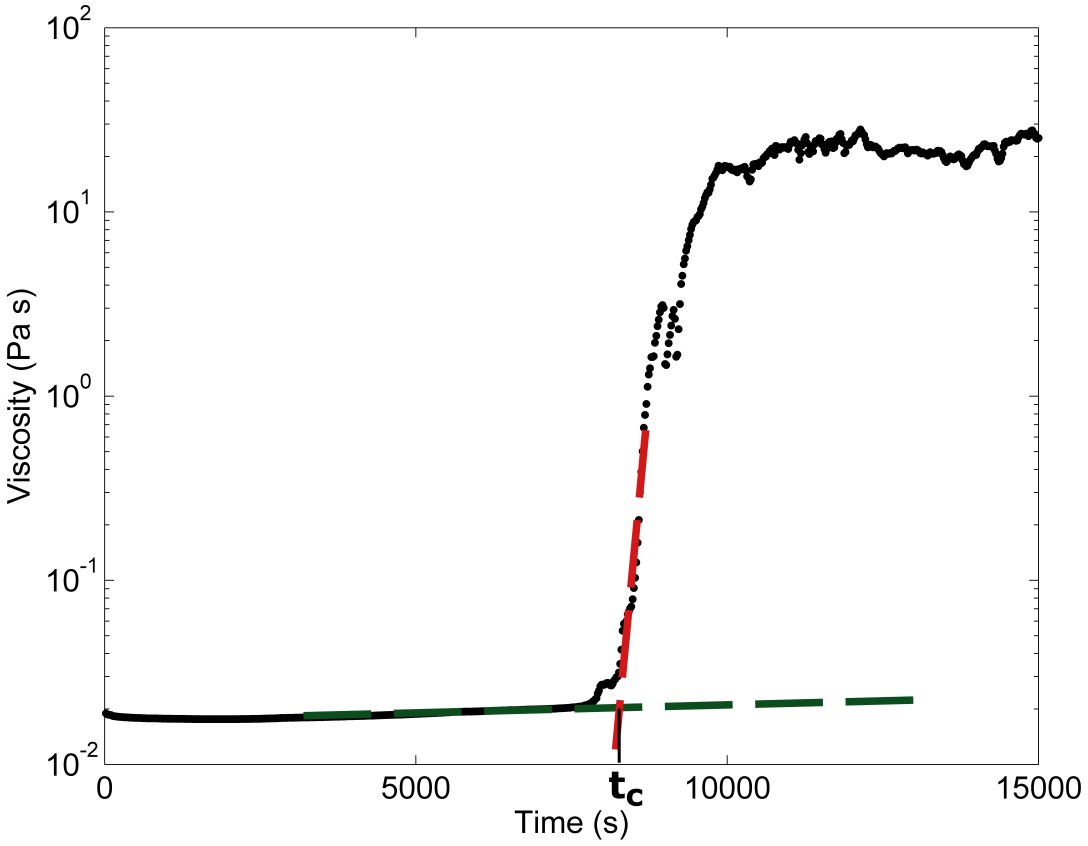

Figure 3.9: Schematic depiction of critical time (t_c) of the hydrate-forming emulsion. The data shown is for an ice-seeded density-matched 40% (v/v) aqueous fraction hydrate-forming emulsion at initial salt concentration of X_{s-in} = 5% (w/w), shear rate of $\dot{\gamma}$ = 100 s^{-1} and temperature equal to the ice-brine equilibrium temperature of T_{eq-ice} = -3.6 °C (62.4% water to hydrate conversion; no net ice formation is thermodynamically allowed).

Since the initial salinity of the aqueous phase in the hydrate-forming emulsion is X_{s-in} = 5% (w/w), no water to ice conversion is thermodynamically allowed at or above the ice-brine equilibrium temperature of T_{eq-ice} = -3.6 °C [48, 1], i.e. at hydrate subcooling of $\Delta T \leq$ 6.3 °C.

In the case of an emulsion seeded with ice below the ice-brine equilibrium temperature, it becomes unclear whether the jump in viscosity is due to ice or hydrate formation; under the imposed conditions, thermodynamically-allowed water to ice conversion at T = -4.6

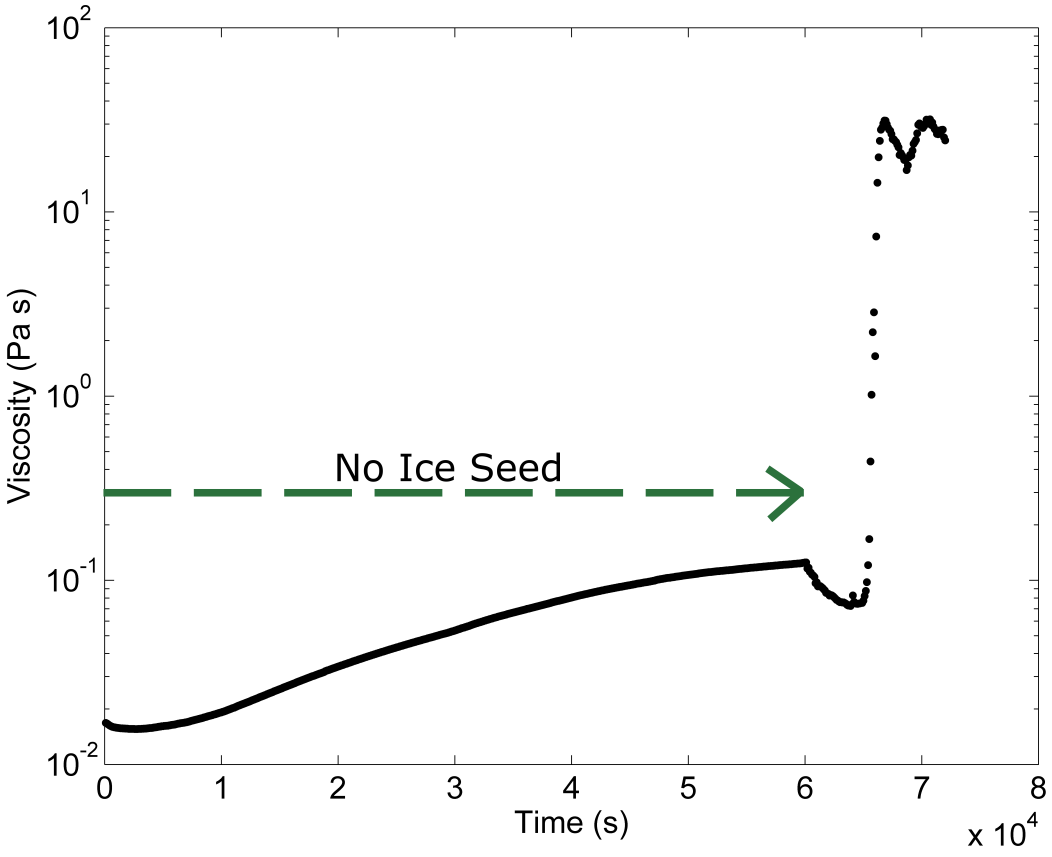

Figure 3.10: Density-matched 40% (v/v) aqueous fraction hydrate-forming emulsion at initial salt concentration of $X_{s-in} = 5\%$ (w/w), shear rate of $\dot{\gamma} = 100\ s^{-1}$ and temperature T = -3.6 °C is ice-seeded at time t = 60000 s. No abrupt jump in viscosity is observed during the period the emulsion remains unseeded. A jump in viscosity is observed at time t = 65000 s, approximately 5000 s after the emulsion is seeded with ice. Thermodynamically-allowed water to hydrate conversion is 62.4%; no net ice formation is thermodynamically allowed.

°C is $X_{w-ice} = 31\%$ (assuming hydrate-formation is negligible) as shown in Table 3.3. In order to establish whether the viscosity is due to ice or hydrate, an ice-forming emulsion, containing isooctane (which does not form hydrate) instead of cyclopentane, is ice-seeded. No jump in viscosity is observed in the ice-forming emulsion; the slight increase with time seen in figure 3.11 may be associated with flocculation and sedimentation of droplets [48] or with ice formation. The viscosity evolutions of hydrate- and ice-forming emulsions are compared in figure 3.11. Thus, the data indicates that hydrate and not ice formation is

responsible for the dominant abrupt viscosity increase observed in the hydrate-forming emulsion at T = -4.6 °C.

Table 3.3: Thermodynamically-allowed water to hydrate and water to ice (if hydrate formation is negligible) in the hydrate-forming emulsion.

Subcooling $\Delta T = T_{eq-hyd} - T$ (°C)	Water to Hydrate Conversion X_{w-hyd} %	Water to Ice Conversion X_{w-ice} %
4.3	51	0
5.3	57	0
6.3	62	0
7.3	66	31

The hydrate-forming emulsion was ice-seeded and hydrate-seeded at subcoolings of ΔT = 4.3, 5.3, 6.3 and 7.3 °C (T = -1.6, -2.6, -3.6, -4.6 °C, with T_{eq-hyd} = 2.7 °C for X_{s-in} = 5% (w/w) salt [48]). Results are shown in figure 3.12. Critical time decreases with subcooling for both hydrate- and ice-seeding methods. A similar decrease in critical time with higher subcooling was reported by Zylyftari *et al.* [48] for unseeded hydrate-forming emulsions. In the unseeded case, critical time is directly affected by hydrate nucleation time [48] as well as growth. Since in the hydrate-seeded case, a decrease in critical time (t_c) with higher subcooling is observed, hydrate growth rate and not nucleation time affects the critical time in the present work: at higher subcooling, higher hydrate growth rate leads to shorter critical time. The decrease in nucleation time with shear rate observed by Zylyftari *et al.* [48] is most likely caused by a higher overall hydrate growth rate rather than by a shorter time for the first nucleation to occur in the emulsion. At higher shear rates, droplet interaction increases; thus, the rate of propagation of hydrate from a droplet to a neighboring droplet is larger. In this respect, each partially converted droplet acts as a hydrate seed for unconverted droplets in the emulsion. Thus, in view of previous work by Zylyftari *et al.* [48] and experiments reported here, both nucleation time and hydrate growth rate are needed to understand critical time in hydrate-forming emulsions.

The difference of approximately 4000 s (i.e., a little more than one hour) in critical

time between the ice- and hydrate-seeded emulsions, found across the entire range of subcoolings, indicates that ice seeding is less effective than hydrate seeding. At higher subcooling of $\Delta T = 6.3$ and 7.3 °C, the standard deviation in critical time in the hydrate-seeding experiments is also about 20 times smaller than in ice-seeding experiments. At smaller subcooling, although the average critical time in the hydrate-seeded emulsion is lower than that of the ice-seeded case, the standard deviation in the hydrate-seeded case is about the same as that of ice-seeded hydrate-forming emulsion and approximately 17 times that of the hydrate-seeded case at the highest subcooling of $\Delta T = 7.3$ °C. Thus, critical time becomes less stochastic only for the hydrate seeding at high subcooling. A possible basis for the difference in critical time between the ice- and hydrate-seeded emulsions may be the difference in surface tensions of the ice-brine and hydrate-brine pairs, and between ice-oil and hydrate-oil. Simulations by Subbotin *et al.* [147] have shown that the tension at an ice-hydrate surface is non-zero and of $O(10^{-2}$ N m$^{-1})$. Hydrate is more hydrophobic than ice, and brine may have more hydrophobic interactions with hydrate [148, 149]. Thus, there is no reason to assume that the angle of contact of droplet on the ice is same as on the hydrate seed. It may be inferred from the schematic in figure 3.8(b) that less nucleating contacts associated with the ice-oil-aqueous phase contact line will result if the brine wets the ice seed more efficiently than the hydrate seed. To illustrate, envision a hypothetical case where the whole crystal is engulfed by brine (i.e. wetting angle is $\theta = 180^o$), and there would be no stable IOA contact line as seen in figure 3.6, and thus the heterogeneous nucleation of hydrate by ice would be eliminated. Furthermore, the hydrate seed surface's relatively higher hydrophobicity [148, 149, 147] and hairy morphology [64, 91] may entrap oil similar to air pockets formed in porous hydrophobic surfaces in bubble nucleation studies [150, 151], and when wetted by brine, may provide more hydrate-oil-aqueous phase contact line compared to ice seed IOA contact line, thus resulting in a faster initial hydrate formation rate.

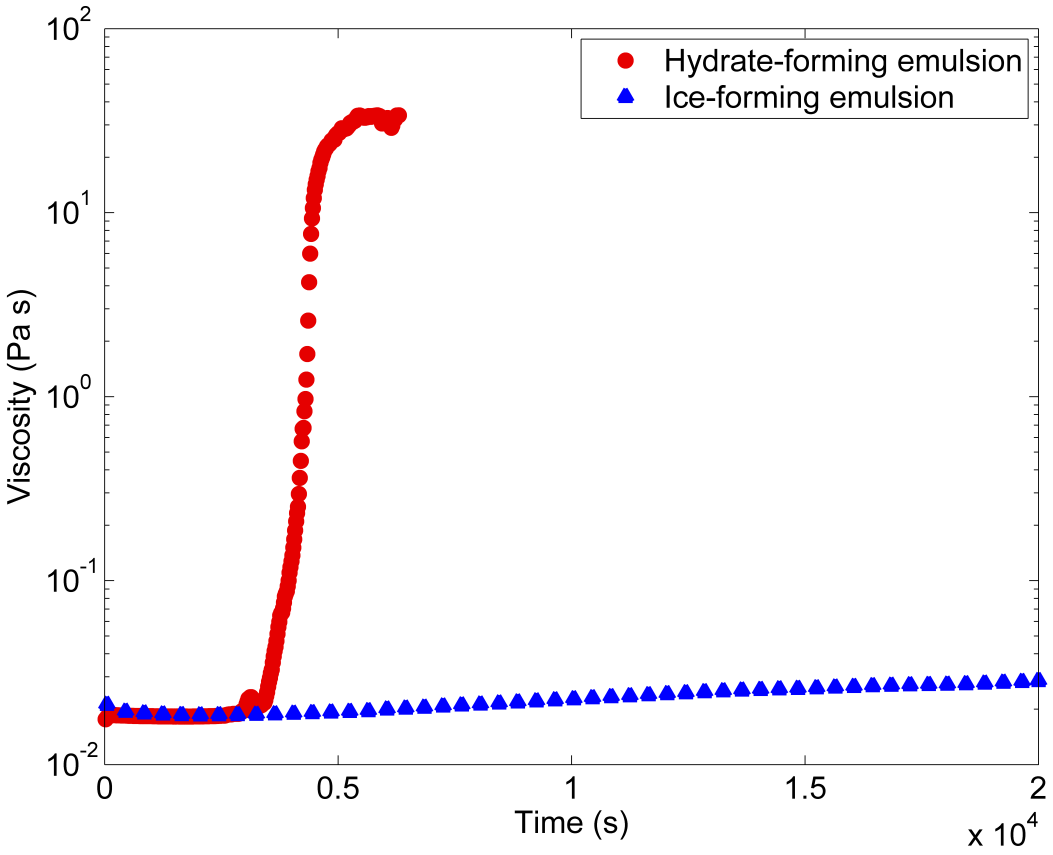

Figure 3.11: Ice-seeded density-matched 40% (v/v) aqueous fraction hydrate- and ice-forming emulsions at $X_{s-in} = 5\%$ (w/w) salt concentration, shear rate of $\dot{\gamma} = 100$ s^{-1} and temperature of $T =$ -4.6 °C. Water to hydrate conversion is $X_{w-hyd} = 65.7\%$; water to ice formation is $X_{w-ice} = 30.9\%$.

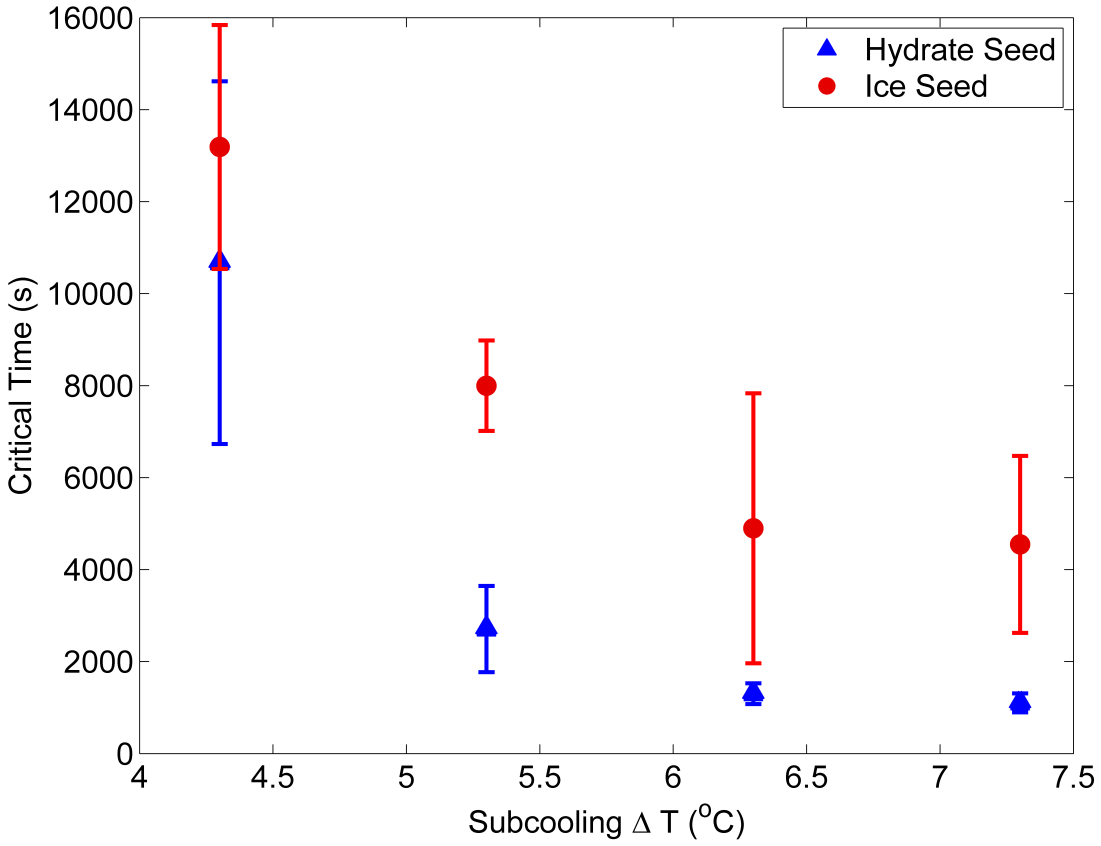

Figure 3.12: Effect of subcooling on the critical time of the ice- and hydrate-seeded hydrate-forming emulsions at X_{s-in} = 5% (w/w) salt concentration and shear rate of $\dot{\gamma}$ = 100 s^{-1}. The points left to right of each symbol correspond to the temperature of T = -1.6, -2.6, -3.6, -4.6 °C, thermodynamically-allowed water to hydrate conversion of X_{w-hyd} = 51.2, 56.7, 62.4, 65.7% and water to ice conversion of X_{w-ice} = 0, 0, 0, 30.9%.

3.4 Conclusion

We have experimentally investigated heterogeneous nucleation of cyclopentane hydrate by ice. The morphological studies coupled with hydrate-forming emulsion rheological properties have elucidated the effects of nucleation by ice on the transition of mechanical properties in hydrate-forming emulsions.

This work was motivated by a striking observation: the heterogeneous nucleation of hydrate by ice is found to be qualitatively controlled by the temperature ramp rate in the experiment. We observed that the amount of unmelted fragmented ice at the organic-aqueous phase interface affects the water to hydrate conversion rate. The shortest conversion time was observed at low temperature ramp rates, thus at a low ice melting rate. However at the lowest temperature ramp rate, conversion time is not at minimum due to limiting free water availability from ice melting; thus, the minimum conversion time occurs at an optimal ratio of unmelted to melted ice. Therefore, our results indicated than an increase in the ice-organic-aqueous (IOA) contact line density (length/surface area) at a drop interface results in a higher hydrate conversion rate.

To elucidate the effect of the IOA contact line, we devised a novel experiment where ice is in contact with bulk aqueous and oil phases, and the oil-aqueous phase interface gives us the proper site of hydrate heterogeneous nucleation. Ice at the equilibrium temperature for contact with an aqueous phase (T_{eq-ice} = -3.6 °C) at a salt concentration 5% (w/w) allows us to unambiguously identify and visualize the site of hydrate crystal formation. Our observation is that cyclopentane hydrate is heterogeneously nucleated by ice at the IOA contact line. The IOA contact line is a crucial region where ice comes into contact with an optimal concentration ratio of cyclopentane and water, thus promoting high hydrate nucleation and growth rates. This region is estimated to be of nanometer extent [144, 145, 146].

The experimental conditions were specifically designed to discriminate between the

effects of ice seeding and ice's influence on the bulk properties. These conditions allowed for hydrate formation, but ice was either thermodynamically impossible (at $T \geq$ -3.6 °C) or its presence was negligible (at T = -4.6 °C). As a result, ice did not measurably affect the observed mechanical transition. The critical time, defined as the time at which an abrupt transition in mechanical properties occurs, after the onset of hydrate-forming conditions for both ice- and hydrate-seeded hydrate-forming emulsions decreased with lower subcooling. Ice seeding was found to be influential, but less effective than hydrate seeding.

4 Modeling oilfield emulsions: Comparison of cyclopentane hydrate and ice

4.1 Introduction

Understanding the underlying physical phenomena leading to plug formation is intrinsically important in effectively and economically preventing flow interruption. Natural gas hydrates are the most common hydrates found in the oilfield emulsions [6]. Since high pressures are needed to conduct experiments in a laboratory setting [152, 153, 154, 155, 156], gas hydrates are particularly difficult to investigate. Alternatively, cyclopentane hydrate- [62, 64, 48, 101] and ice-forming emulsions [2] have been proposed as model emulsions without the need for pressurized environments.

Cyclopentane forms a cubic hydrate structure II (sII) [6] as natural gas hydrate as is most common in petroleum production (owing to the mixing of methane with larger molecules), but unlike natural gas, cyclopentane is stable in liquid form at room temperature and atmospheric pressure. Thus, cyclopentane based emulsions mechanical properties have been investigated utilizing non-pressurized rheometers [62, 48, 101]. The time where an abrupt jump in viscosity, referred as critical time, is observed for cyclopentane hydrate-forming emulsions has been found to decrease with subcooling [62, 48, 101]. Zy-

lyftari *et al.* [48, 101] found that both critical time and hydrate growth time, which is defined as the period of time from the jump in viscosity to attaining final viscosity, are dependent on the level of subcooling. The final viscosity achieved by a slurry formed from a hydrate-forming emulsion, and its yield stress, are mainly dependent on the level of water to hydrate conversion, and a peak in viscosity and yield stress are observed at about 80% water to hydrate conversion [48]; conversion in these experiments was controlled by varying temperature and initial salt concentration in the aqueous phase. The observed peak in viscosity and yield stress at an intermediate conversion indicated capillary bridge formation due to residual brine between hydrate particles [48, 5, 21, 22].

Rensing *et al.* [2] proposed that ice-forming emulsions are analogous and equivalent to hydrate-forming emulsions based on the fact that hydrate is mostly formed of water (over 80 mol%) [6]. The authors used water-in-crude oil emulsions in the experimental investigation. Viscosity and yield stress measurements were performed by varying aqueous volume fraction at no salt and 3.5% (w/w) NaCl (salt) concentration. The main findings in their study were the three yield stress regimes: 1) no yield stress under 25% (v/v) water fraction, 2) about 300 Pa yield stress at 25-55% (v/v) water fraction and 3) at above 55% (v/v) yield stress was higher than the rheometer measuring limit of 3000 Pa.

From a practical perspective, investigating the mechanical properties of a potentially hydrate-forming crude oil by adding only water to form ice slurry may seem more reasonable compared to diluting the crude oil with additional cyclopentane to form hydrate slurry. Thus, if ice-forming emulsions mechanical properties are equivalent to hydrate-forming emulsions, ice-forming water-in-crude oil emulsions may provide a better method of testing the properties of crude oil. Therefore, in order to assess the assumption of ice-forming emulsion being equal to hydrate-forming emulsion, in this study we compared the rheological and morphological properties of cyclopentane hydrate- and ice-forming emulsions at similar drop size, subcoolings and water conversions. Rheological and morphological experiments indicate that the behavior of cyclopentane hydrate is quite similar

to propane gas hydrate. We controlled the water conversion in the emulsions by varying initial aqueous phase salt concentration at a fixed temperature. Our results indicate that ice-forming emulsions behaves significantly different to hydrate-forming emulsions. Our findings at a single water fraction clearly indicate that care must be taken in relating behaviors of the ice and hydrate slurries, with further work examining whether a correspondence of the two at different water levels may be deduced.

4.2 Experimental methods

4.2.1 Materials

The aqueous phase in our studies at various salt concentration was formed by dissolving sodium chloride (99+% pure, Fisher Scientific) in deionized water obtained from a Millipore QTM system. The oil phase of the hydrate-forming emulsion is composed of 50% (v/v) cyclopentane (99+% pure, Fisher Scientific); whereas isooctane (99+% pure, Fisher Scientific), which does not form a hydrate, instead of cyclopentane is used for the oil phase of the ice-forming emulsion. Light mineral oil (NF/FCC Fisher Scientific) and Halocarbon 27 (polychlorotrifluoroethylene polymer, Halocarbon Products Corporation) are used to match the density of the oil and aqueous phase to minimize sedimentation of the droplets in the hydrate- and ice-forming emulsions. A non-ionic surfactant, sorbitan monooleate (Span 80 from Sigma-Aldrich), with a hydrophilic-lipophilic balance (HLB) of 4.3 [60], is used as a surfactant to form emulsion at a concentration of 0.05% (v/v) in the oil phase. Span 80 does not form a stable lipid bilayer in the aqueous phase [61]. Span 80 critical micelle concentration in the oil phase is 0.03 % (v/v) [48, 62]. Taking into account the interfacial area generated in the oil-aqueous phase interface after an emulsion is formed, no micelle formation is expected in the oil phase of the emulsion; this is discussed in detail elsewhere [48].

For the propane hydrate-forming emulsion, light mineral oil and Halocarbon at 0.1% (v/v) Span 80 is used as oil phase. Propane gas with a purity of 99.5% was obtained from T. W. Smith. All the materials were used as obtained without further purification. Relevant physical properties of the materials are provided in table 4.1.

Table 4.1: Physical properties of materials used in this study.

Material	Chemical Formula	Mol. Weight (g mol^{-1})	Density (g cm^{-3})	Viscosity (cP)
Cyclopentane	C_5H_{10}	70.1	0.751 (25 °C)	0.44 (20 °C)
Isooctane	C_8H_{18}	114.2	0.690 (25 °C)	0.51 (22 °C)
Propane	C_3H_8	44.1	0.002 (0 °C, 101.3 kPa)	-
Halocarbon 27	$(C_2ClF_3)_n$	-	1.96 (37 °C)	51 (37.8 °C)
Light mineral oil	-	-	0.83 (15.6 °C)	46 (25 °C)
Span 80	$C_{24}H_{44}O_6$	428.6	0.986 (25 °C)	1200-2000 (20 °C)
Water	H_2O	18.0	1.00 (4 °C)	1.00 (20 °C)
Sodium Chloride	NaCl	58.4	2.16 (25 °C)	-

4.2.2 Rheology

Atmospheric pressure

Rheological measurements for cyclopentane hydrate and ice slurry were performed on density-matched 40% (v/v) aqueous fraction emulsions. Emulsions were obtained by mixing a total volume of 50 ml of water and oil using the IKA T25 Digital Ultra-Turrax at an intensity of 7000 rpm for 5 minutes. The droplet diameter for both hydrate- and ice-forming emulsions is $d = O(10)\mu$m [48, 101]. The hydrate-forming emulsion continuous fluid viscosity is $\eta_{c-hyd} = 0.0053$ Pa s (T = -7.0 °C); the ice-forming emulsion fluid viscosity is $\eta_{c-ice} = 0.0064$ Pa s (T = -12.4 °C). Droplet deformation due to flow is negligible [48, 101]. Emulsions are stable and do not coalesce for several days but flocculation has been observed under quiescent conditions [62, 48]. Sedimentation effects are considered negligible in the experimental timescale [48].

Rheological data were obtained by using a stress-controlled rheometer (AR 2000ex, TA Instruments) equipped with a roughened cylindrical cup and a vane rotor. The cylindrical

cup has a 15 mm radius, and the vane rotor has a 14 mm radius, thus a gap of 1 mm. The vane rotor has 4 equally-spaced blades with height of 42 mm. Waterproof sandpaper of root mean square value roughness of $O(100\ \mu\text{m})$ was glued on the wall of the cup to prevent wall slip. The effective gap is less than the original 1 mm; the data are corrected for the new gap. Temperature control was achieved through a Peltier jacket system. A volume of 28 mL emulsion at room temperature (T $\approx$ 25°C) was transferred to the precooled cylindrical cup of the rheometer. As soon as the emulsion temperature reached the desired temperature, it was seeded with ice/hydrate crystals of approximately 1 mm in diameter (five on the upper surface) [101]. The emulsions are sheared at a constant shear rate of $\dot{\gamma} = 100\ \text{s}^{-1}$ until the measured viscosity reaches a steady value within the intrinsic experimental error. The final hydrate and ice slurry structure formed without any aging process (i.e., immediately following formation under shear) is run through a shear rate ramp from 100 to 1 s^{-1} and back to 100 s^{-1} (total loop duration is 1200 s) to determine shear rate dependence and whether hysteresis is present. Yield stress of the final structure was measured through the oscillatory stress ramp method at a frequency of 1 Hz [157, 158, 159].

High pressure

The density-matched oil mixture of mineral oil and Halocarbon is used to prepare the emulsion. Span 80 surfactant is added at a concentration of 0.1% by volume of oil phase. The emulsions are prepared by applying mechanical stirring using an IKA T25 digital Ultra-Turrax homogenizer operating at 7000 rpm for 5 minutes. The rheology data is obtained using the stress-controlled AR 2000ex rheometer equipped with high-pressure concentric cylinder geometry (TA Instruments). The pressure cell is a sealed vessel that can be pressurized up to 138 bar (2000 psi), over a temperature range of -10 to 150 °C. The geometry consists of a steel outer cylindrical cup and a titanium inner rotor. The cup sits in a Peltier jacket, which is mounted to the rheometer. A cooling bath with

water supplies the jacket with cooling fluid. The outer cylinder has a 14 mm radius, the inner cylinder has a 13 mm radius, and thus the geometry has a 1 mm gap. The sample volume used in an experiment is 9.5 mL. The emulsion prepared at room temperature is gently transferred to the rheometer. The cell is pressurized to 4 bars with propane gas from an external high-pressure propane bottle. The emulsion is allowed to saturate at rest with propane gas at 5 °C. After the saturation, the cell is re-pressurized with propane gas to 4 bars. In order to avoid long and unpredictable induction times, we preferred the formation of propane hydrates using ice. The temperature protocol used for the synthesis of hydrates is as follows:

1. First, the temperature T is decreased from 5 °C to -15 °C at a rate $\dot{T}$ = of -1 °C min^{-1} and at a shear rate of $\dot{\gamma} = 50\ s^{-1}$. During this temperature ramp, the viscosity of the emulsion increases. The pressure in the cell reduces from the initial value of 4 bars at 5 °C because the solubility of gas in liquid increases on decreasing the temperature.

2. T is held at -15 °C until the water drops in the emulsion freezes to ice. The formation of ice is indicated by a small increase (first peak) in the viscosity curve.

3. The temperature is then increased to 0.5 °C at a rate of $\dot{T} = 1$ °C min^{-1} to melt the ice providing liquid water for the hydrate formation. This melting ice helps in overcoming the long induction time associated with the propane hydrate nucleation [101]. As the temperature increases, the viscosity of the ice slurry decreases and some pressure is recovered in the cell. As soon as the freshly melted water comes in contact with propane gas, hydrate formation starts and we observe an increase in the viscosity.

4. Once the hydrate growth completes, the viscosity of hydrate slurry reaches a plateau. The temperature is then increased from 0.5 °C to 25 °C to dissociate the hydrate, which results in a sudden drop in the viscosity.

4.2.3 Morphology

Hydrate- and ice-forming emulsions

An emulsion of 15% (v/v) aqueous was placed in a small well (12.5 mm in diameter and 2 mm deep) machined in an aluminum microscope slide. Note that this lower water fraction emulsion is used to allow easier visualization of the droplet-scale morphology. A Peltier stage (Linkam LTS 120) was used to provide a well-controlled temperature environment. Images were captured using a Sony digital XCD-SX 910 camera equipped with an Edmund Optics VZM 300 Zoom imaging lens, as described previously [91, 101]. Emulsions consisting of droplets of $d = O(100)$ μm prepared with a Caframo high torque stirrer (BDC 1850) at speed of 350 rpm for 5 minutes were used since emulsions used in the rheometric experiments of $d = O(10)$ μm were difficult to visualize. The experimental procedure followed was:

1. Emulsion was placed in the well;
2. temperature T was lowered to $T_{fin} = T_{exp}$ as shown in table 4.4 at a rate of $\dot{T}$ = -5.0 °C min^{-1};
3. T was held at T_{exp};
4. hydrate seed for hydrate-forming emulsion or ice seed for ice-forming emulsion was added in the well and the cover was rapidly closed.

Cyclopentane hydrate-forming single drop

Using the same setup as above, a 1 μL water drop (no salt) was placed in the middle of the small well. The experimental procedure followed was:

1. Temperature T was lowered to T_{fin} = -40.0 °C at a rate of $\dot{T}$ = -5.0 °C min^{-1} to induce ice crystallization of the drop previously place in the middle of the well;

2. T was held at T_{fin} = -40.0 °C until the aqueous drop is fully solidified;

3. T was increased from -40.0 °C to T_{fin} = -5.0 °C;

4. T was held at T_{fin} = -5.0 °C and the ice in the well is covered with cyclopentane with 0.05% (v/v) Span 80;

5. T was increased at a rate of $\dot{T}$ = 5.0 °C min^{-1} from -5.0 °C to T_{fin} = 0.2 °C.

Propane hydrate-forming single drop

Propane hydrate visualization was performed using a high-pressure heating-freezing cell (THMS 600-PS, Linkam Scientific) placed on a Nikon microscopic stage with an objective lens with a magnification range of 2.5X to 10X and a CCD detector for a live recording. The cell can be operated up to 14 bars at a temperature range of -120 to 500 °C, and its temperature was controlled with an accuracy of 0.1 °C by using a temperature controller (TMS 94, Linkam Scientific). In all the experiments, a quartz crucible of 15 mm inner diameter was used. The experimental protocol is as follows: First, using a pipette, 200 μL of light mineral oil is loaded in the crucible, which spreads in the crucible as a thin film. A water droplet of diameter 600-800 μm (10 μL) is suspended in the mineral oil. The cell is sealed after suspending the drop and the cell is then pressurized to 5 bars with propane gas. The water drop suspended in the mineral oil is then allowed to stand under propane pressure to saturate the oil. During this preconditioning time, the pressure in the cell drops from 5 to 4.6 bars. After the preconditioning step, the pressure does not change even after waiting for a much longer time, which means it has reached the equilibrium value. The temperature protocol used for the synthesis of hydrates is as follows:

1. Temperature T is decreased from 22 °C (room temperature) to T_{fin} = -15 °C at a rate of $\dot{T}$ = -5 °C min^{-1};

2. T is held at T_{fin} = -15 °C until the water drop freezes completely. The pressure

in the cell reduces from the initial value of 4.6 bars at 22 °C to 2.8 bars at -15 ° because the solubility of gas in liquid increases on decreasing the temperature.

3. The temperature is then increased to 0.1 °C at a rate of $\dot{T}$ = 5 °C min^{-1} and some pressure is recovered in the cell. The pressure in the cell becomes 3.8 bars (approximately) at 0.1 °C.

4. The temperature is maintained constant at T_{fin} = 0.1 °C for one hour to melt the ice providing liquid water for the hydrate formation.

4.3 Results and discussion

4.3.1 Viscosity after conversion

Following temperature quenching from room temperature (25°C) to the experimental temperature, viscosities of the hydrate- and ice-forming emulsions evolve as shown in figure 4.1. Cyclopentane hydrate-forming emulsion mechanical properties and their evolution with time are observed to be quite similar to propane gas hydrate-forming emulsions (figure 4.2). In order to compare the hydrate and ice-forming emulsions mechanical properties we extracted the final viscosity from the viscosity evolution graphs as previously described by Zylyftari *et al.* [48]. Hydrate- and ice-forming emulsions were seeded with externally-grown hydrate and ice particles respectively in order to avoid delay of crystallization due to nucleation time [48, 101].

The final relative viscosities $\eta_{rel} = \frac{\eta}{\eta_c}$ (where η is the viscosity of the slurry and η_c is the continuous phase viscosity, i.e. for hydrate-forming emulsion η_{c-hyd} = 0.0053 Pa s and for ice-forming emulsion η_{c-ice} = 0.0064 Pa s) of hydrate- and ice-forming emulsions at varying salt concentrations and shear rate of $\dot{\gamma}$ = 100 s^{-1} are plotted with respect to thermodynamically-allowed water to hydrate/ice conversion in figure 4.3. Experimental temperatures of T = -7.0 °C for hydrate-forming emulsion and T = -12.4 °C for ice-

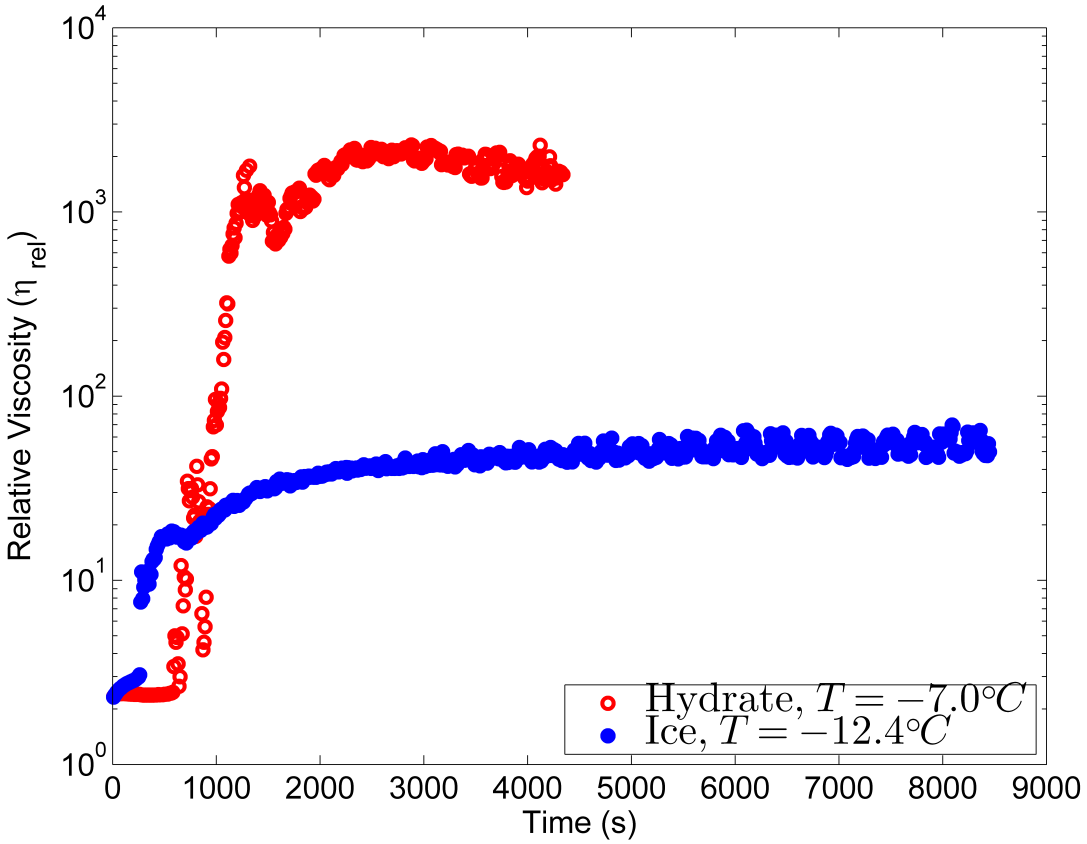

Figure 4.1: Relative viscosity evolution for 40% (v/v) water (X_{s-in} = 0.0% (w/w)) fraction hydrate-forming emulsion at T = -7.0 °C (X_{w-hyd} = 100%) and ice-forming emulsion at T = -12.4 °C (X_{w-ice} = 100%) at shear rate of $\dot{\gamma}$ = 100 s^{-1}. The hydrate- and ice-forming emulsion continuous fluid viscosities are η_{c-hyd} = 0.0053 Pa s and η_{c-ice} = 0.0064 Pa s. For both hydrate and ice-forming emulsions, subcooling is same, ΔT = 12.4 °C.

forming emulsion were selected to keep subcooling similar. The points from right to left for each symbol are for X_{s-in} = 0, 3.4, 5, 7.5, 10, 12.5 and 15% (w/w) at similar initial subcoolings as shown in Table 4.2. At water conversion of X_w = 100%, the ratio of hydrate- and ice-forming emulsions final viscosities is $\frac{\eta_{rel-hyd}}{\eta_{rel-ice}} = O(10)$ ($\eta_{rel-hyd}$ is the relative viscosity of hydrate slurry and $\eta_{rel-ice}$ is the relative viscosity of ice slurry). At water conversion of X_w = 58-81%, the ratio of hydrate and ice slurry is $\frac{\eta_{rel-hyd}}{\eta_{rel-ice}} = O(10^2)$. Additionally, data from Rensing *et al.* [2] in which ice slurry was formed in

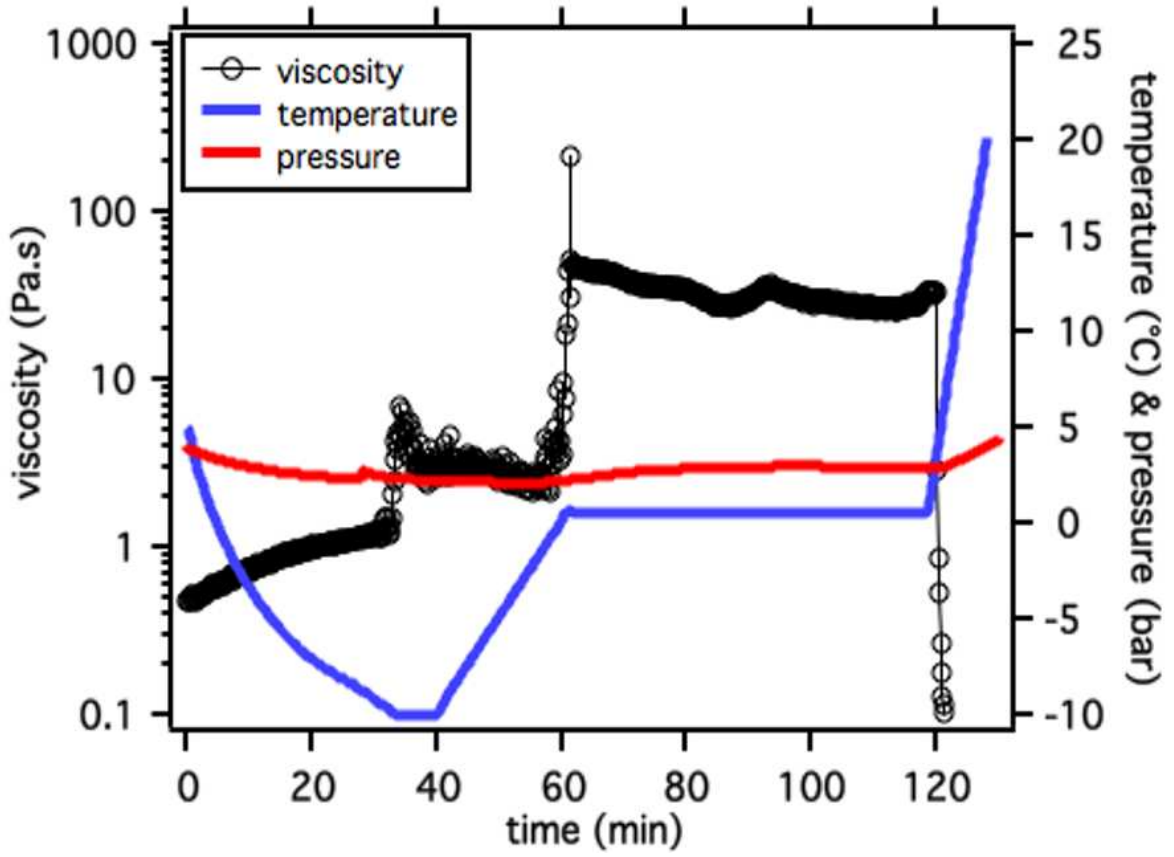

Figure 4.2: Viscosity evolution for 40% (v/v) water (X_{s-in} = 0.0% (w/w)) fraction propane hydrate-forming emulsion at shear rate of $\dot{\gamma} = 50\ s^{-1}$.

water-in-crude oil emulsion were compared with our data as shown in figure 4.3. The viscosity from Rensing *et al.* data [2] compare well with our results; they are within the same order of magnitude. Thus, ice-forming emulsion final viscosity is significantly lower compared to hydrate-forming emulsion final viscosity. The peak in viscosity observed for hydrate-forming emulsion at water to hydrate conversion of X_{w-hyd} = 72-81% indicates capillary bridge formation [5, 21, 22] as discussed in detail by Zylyftari *et al.* [48]. No such peak in viscosity is observed for ice-forming emulsions; maximum viscosity for ice-forming emulsion is achieved at water to ice conversion of X_{w-hyd} = 100% as shown in figure 4.3. The striking difference in viscosity and the lack of an observed peak in viscosity in the ice-forming emulsion shows that ice-forming emulsion may not be an adequate emulsion

model capturing relevant physical properties of hydrate-forming emulsion at least not for the same water fractions.

Table 4.2: Initial subcoolings and thermodynamic water conversions for hydrate- and ice-forming emulsions.

	Hydrate Slurry T = -7.0 °C		Ice Slurry T = -12.4 °C	
Salt Concentration X_{s-in} (% w/w)	Initial Subcooling ΔT_{in-hyd} (°C)	Water Conversion X_{w-hyd} (%)	Initial Subcooling ΔT_{in-ice} (°C)	Water Conversion X_{w-ice} (%)
0.0	12.4	100	12.4	100
3.4	10.3	81	9.9	82
5.0	9.5	72	8.8	74
7.5	8.0	58	7.6	59
10.0	6.0	42	5.4	44
12.5	4.3	27	3.9	29
15.0	2.4	11	1.4	12

The final hydrate- and ice-forming emulsions are shear thinning as shown in figure 4.4. The shear thinning behavior of hydrate-forming emulsions has been reported before by Zylyftari *et al.* [48]. The final viscosity dependence on shear rate fits a power law, known also as Ostwald-de Waele law [97],

$$\eta = K\dot{\gamma}^{n-1} \ , \tag{4.1}$$

where η is the effective viscosity of the suspension, K is the flow consistency index, $\dot{\gamma}$ is the shear rate, and $n < 1$ is the flow behavior index ($n = 1$ implies Newtonian response). The fitting parameters, K and n for water conversions of hydrate slurry at X_{w-hyd} = 58 and 100% and ice slurry at X_{w-ice} = 59 and 100% are given in table 4.3. The ratio of flow consistency index of final structure hydrate- to ice-forming emulsion is $\frac{K_{hyd}}{K_{ice}} = O\ (10^2)$ at X_w = 100% and $\frac{K_{hyd}}{K_{ice}} = O\ (10^3)$ at $X_w \approx$ 60%. The ratio of flow behavior index of the final hydrate- to ice-forming is $\frac{n_{hyd}}{n_{ice}} \approx 0.5$ at X_w = 100% and $\frac{n_{hyd}}{n_{ice}}$ ≈ 0.2 at $X_w \approx$ 60%. Thus, the ice-forming emulsion final structure in addition to being significantly less viscous, is also characterized by a less shear thinning behavior compared

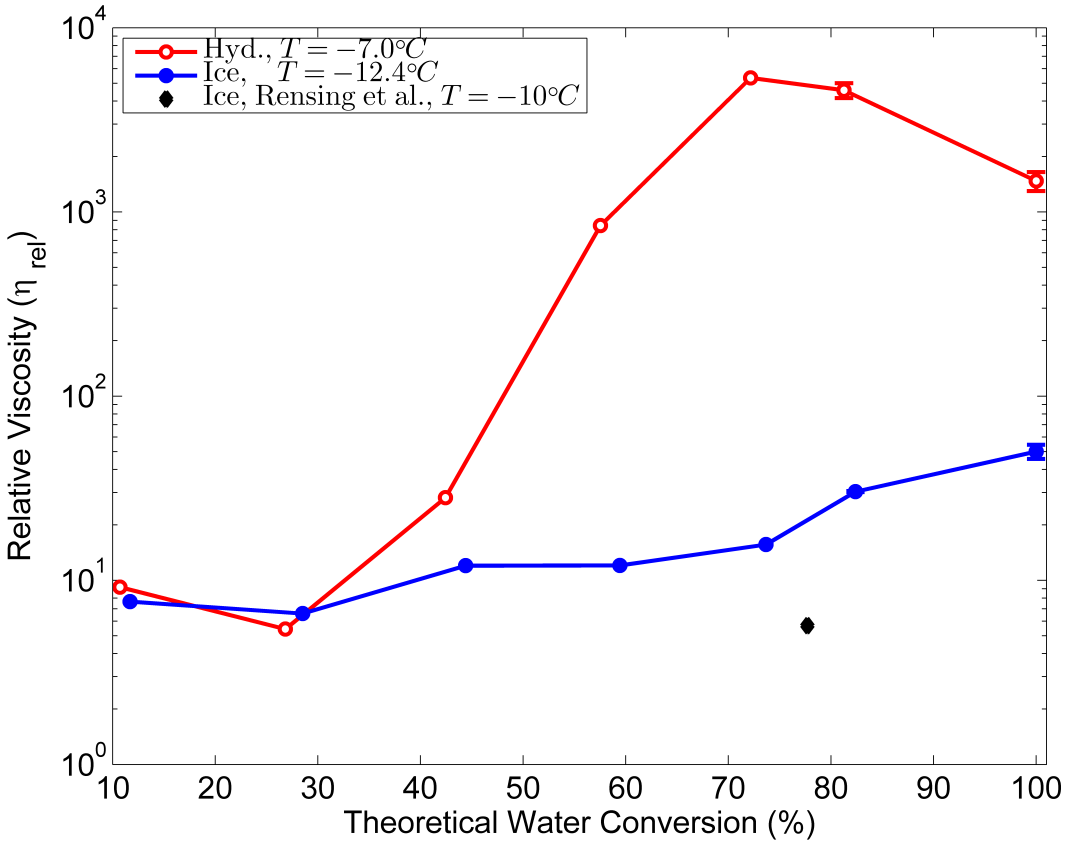

Figure 4.3: Final hydrate- and ice-forming emulsion viscosity at shear rate of $\dot{\gamma} = 100\ \mathrm{s}^{-1}$ plotted as a function of theoretical water to hydrate and ice conversion, respectively. The hydrate- and ice-forming emulsion continuous fluid viscosities are $\eta_{c-hyd} = 0.0053$ Pa s and $\eta_{c-ice} = 0.0064$ Pa s. The points from right to left of each symbol correspond to initial salt concentration of $X_{s-in} = 0.0$, 3.4, 5.0, 7.5, 10.0, 12.5 and 15.0% (w/w). The data from Rensing *et al.* [2] is at initial salt concentration of $X_{s-in} = 3.5\%$ (w/w).

to hydrate-forming emulsion. The hydrate- [48] and ice-forming emulsions final structures are non-thixotropic (figure 4.4).

Table 4.3: Shear thinning fit parameters, for the form $\eta = K\dot{\gamma}^{n-1}$.

Theoretical Water Conversion % (w/w)	Flow Consistency Index K (Pa s^n)		Flow Behavior Index n	
	Hydrate	Ice	Hydrate	Ice
100	440	1.8	0.23	0.43
58	445		0.10	
59		0.55		0.49

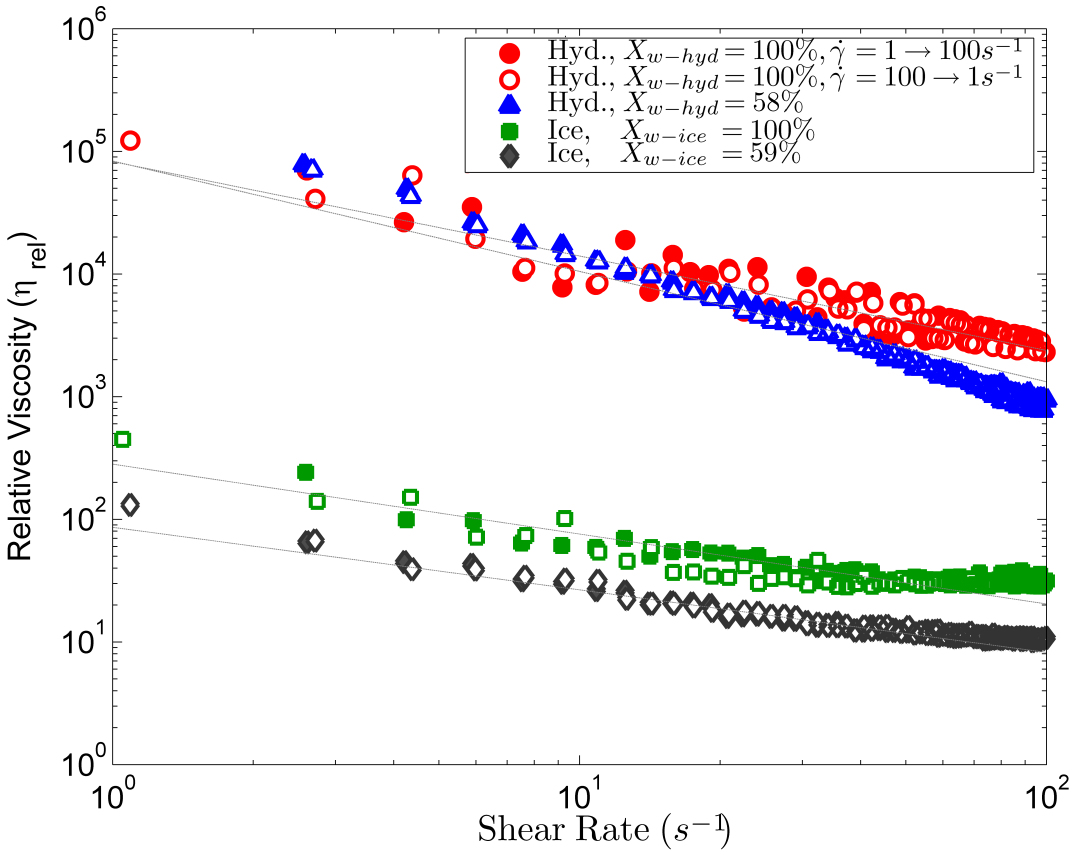

Figure 4.4: Shear rate dependence, showing shear thinning, of hydrate-forming emulsions structure formed at T = -7.0°C and ice-forming emulsions at T = -12.4°C at initial salt concentrations of X_{s-in} = 0.0 and 7.5% (w/w) and $\dot{\gamma}$ = 100 s^{-1} (closed symbols $\dot{\gamma} = 1 \rightarrow 100$ s^{-1}, open symbols $\dot{\gamma} = 100 \rightarrow 1$ s^{-1}). The hydrate- and ice-forming emulsion continuous fluid viscosities are η_{c-hyd} = 0.0053 Pa s and η_{c-ice} = 0.0064 Pa s.

4.3.2 Yield Stress

Yield stress gives the minimum shear stress needed to initiate flow in a material [98, 157, 159]. Thus, yield stress is a measurement of the interparticle forces that need to be overcome for a material to flow [98, 99, 159]. The most reliable method of measuring yield stress in a hydrate and ice slurry appears to be through the oscillatory stress ramp [157, 158, 159]. Particularly, a maximum in elastic stress, which is the product of elastic modulus (G') and strain (γ) gives an accurate and consistent measure of yield stress ($\tau_y = G'\gamma$). Below the yield stress, the elastic stress increases linearly with the applied oscillatory stress and above the yield stress, the elastic stress deviates from linear dependence.

The hydrate and ice slurries as formed in the rheometer (with viscosity evolution shown in figure 4.1) are used for further yield stress measurements. The slurry is subjected to a continuous oscillatory stress ramp test in which the amplitude of the oscillatory stress is increased logarithmically. Figure 4.5 shows a comparison of elastic stresses for hydrate and ice slurries. The maximum value in elastic stress ($G'\gamma$) is interpreted here as the yield stress. This method permits us to locate a sharp, clear and unambiguous yield stress value and thus proves to be a very robust and reliable method.

The yield stresses for hydrate- and ice-forming emulsions at various salt concentrations (the points from right to left for each symbol are for X_{s-in} = 0, 3.4, 5, 7.5, 10, 12.5 and 15% (w/w)) are plotted with respect to water conversions in figure 4.6. At water conversions of $X_w \geq 58\%$, the yield stress ratio of hydrate- to ice-forming emulsions is $\frac{\tau_{y-hyd}}{\tau_{y-ice}} > O\ (100)$ as shown in figure 4.6. The huge difference in yield stress between the hydrate- and ice-forming emulsions indicates that ice-forming emulsion may not be a well-fitted model for hydrate studies. At water to hydrate conversion of $X_{w-hyd} = 81\%$, a peak in yield stress, $\tau_{y-hyd} = 1955$ Pa is observed; at $X_{w-hyd} = 100\%$, yield stress is 36% lower, i.e. $\tau_{y-hyd} = 1250$ Pa. Similarly, at water to ice conversion of $X_{w-ice} = 82\%$, a peak

in yield stress is observed, which is lower than the yield stress at full water conversion; both yield stress values are small. The observed peak in the hydrate- and ice-forming emulsions suggests that capillary bridges are formed [95, 96, 21, 22] and have the most effect on the mechanical properties measured here at water conversion of $X_w \approx 80\%$, i.e. the optimal number of capillary bridges and crystal surface is present in the suspension [48]. Interestingly, in ice-forming emulsions no peak viscosity is observed at similar water conversions.

The yield stress reported in this study for hydrate slurry at water to hydrate conversion of $X_{w-hyd} \geq 58\%$ is an order of magnitude higher than the values reported by Zylyftari *et al.* [48] for the same conditions. The shear stress ramp method [74] used by Zylyftari *et al.* [48] tends to underestimate yield stress and is prone to errors [158, 159]. Furthermore, the yield stress reported previously may have been affected by wall slip [158, 157]. The yield stress reported by Rensing *et al.* [2] for the 40% (v/v) ice-forming emulsion with no salt is one to two orders of magnitude higher than the values reported here for an ice-forming slurry. In addition to the error-prone method of shear stress ramp used by Rensing *et al.* [2], we also used the oscillatory stress ramp method following the protocol used by Rensing *et al.* [2] and we obtained values an order of magnitude higher compared to the yield stress following our protocol. This suggests that the final structure of the ice-slurry after two hours of annealing under small strain oscillatory motion might not form the same structure as under constant shear rate. In addition the droplet size in the study by Rensing *et al.* [2] is an order of magnitude lower than our emulsion. Crude oil and asphaltenes [2] may also contribute to the observed difference. Regardless of the cause of the observed difference, the crude oil based ice-slurry yield stress is approximately an order of magnitude lower compared to cyclopentane-hydrate forming emulsion as shown in figure 4.6.

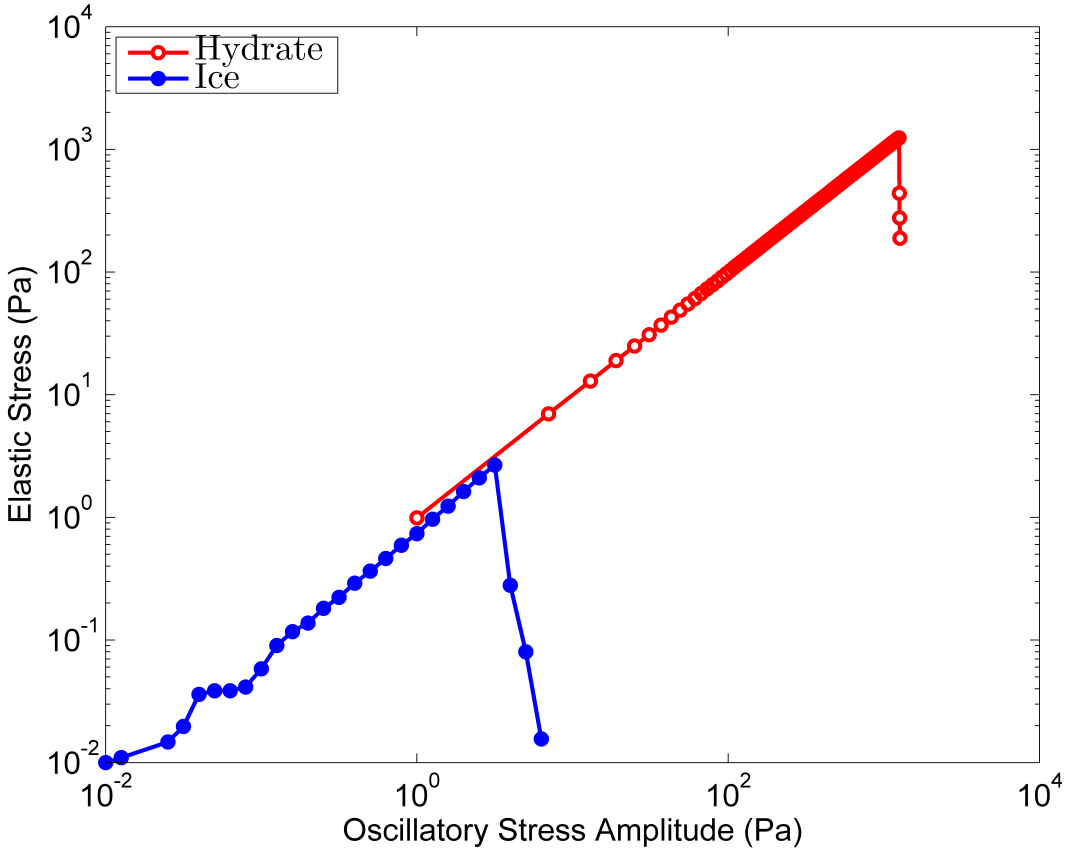

Figure 4.5: Elastic stress ($G'\gamma$) for 40% (v/v) water (X_{s-in} = 0.0% (w/w)) fraction hydrate-forming emulsion final structure at T = -7.0 °C (X_{w-hyd} = 100%) and ice-forming emulsion final structure at T = -12.4 °C (X_{w-ice} = 100%) at shear rate of and $\dot{\gamma}$ = 100 s^{-1}. For both hydrate and ice-forming emulsions, subcooling is same, ΔT = 12.4 °C.

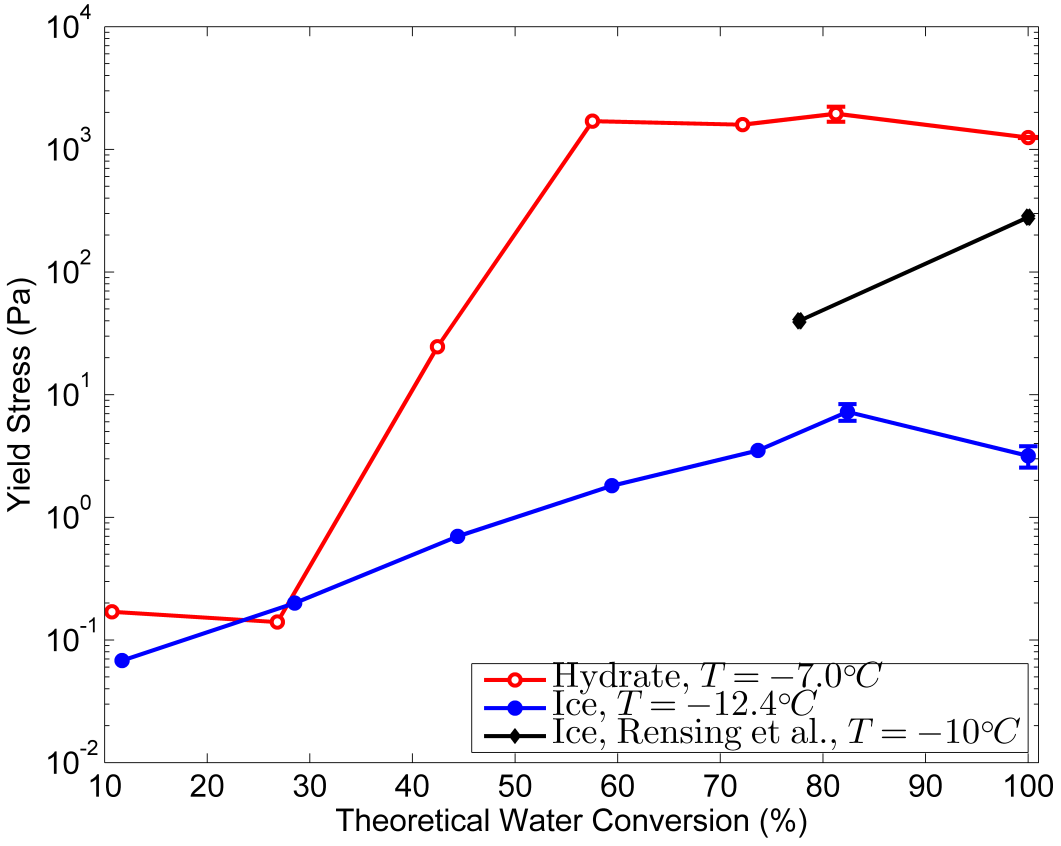

Figure 4.6: Yield stress of hydrate- and ice-forming emulsion final structure formed at shear rate of $\dot{\gamma} = 100\ \text{s}^{-1}$ plotted as a function of theoretical water to hydrate and ice conversion, respectively. The points from right to left of each symbol correspond to initial salt concentration of $X_{s-in} = 0.0$, 3.4, 5.0, 7.5, 10.0, 12.5 and 15.0% (w/w). The data from right to left of Rensing *et al.* [2] correspond to initial salt concentration of $X_{s-in} = 0$ and 3.5% (w/w).

4.3.3 Morphology

Morphological experiments were run to understand the structure evolution of the cyclopentane hydrate- and ice-forming emulsions. It should be noted that the morphological features of cyclopentane hydrate closely resemble those of propane gas hydrate as shown in the single drop experiments in figure 4.7; a more detailed morphological comparison of cyclopentane and propane hydrate-forming emulsion will be given in a separate paper as it needs further investigation. The experimental conditions for hydrate- and ice-forming emulsion are summarized in table 4.4. For a given initial salt concentration, initial subcooling was kept the same for hydrate- and ice-forming emulsions.

In figure 4.8 structural evolution of water ($X_{s-in} = 0.0\%$ (w/w)) based hydrate- and ice-forming emulsions at a subcooling of $\Delta T = 10.4$ °C are shown. Thermodynamically-allowed water conversion in both emulsions is $X_w = 100\%$. In the hydrate-forming emulsion (figure 4.8(a-d)), the water drop is punctured by the needle-like surface [64, 91, 101] of the hydrate seed. Following puncturing the aqueous drop wets the hydrate seed and conversion into hydrate occurs. Once the conversion of the emulsion to hydrate is complete (figure 4.8(d)) a porous hydrate structure is added to the hydrate seed. The original spherical shape of the aqueous drop is not retained, thus the shell model growth [160] is not observed in our experiments. In ice-forming emulsion (figure 4.8(e-h)), once the water drop ($X_{s-in} = 0.0\%$ (w/w)) contacts the ice seed, the drop fully converts into ice particle. The ice particle retains the spherical shape of the drop as observed in figure 4.8(h). The apparent difference in the mechanisms of crystal growth and morphology between the hydrate- and ice-forming emulsions explains the large ratios of viscosity $\frac{\eta_{rel-hyd}}{\eta_{rel-hyd}}$ (figure 4.3) and yield stress $\frac{\tau_{y-hyd}}{\tau_{y-ice}}$ (figure 4.6).

Figure 4.9 shows the structural evolution of hydrate- and ice-forming emulsions in brine ($X_{s-in} = 7.5\%$ (w/w)) at a subcooling of $\Delta T = 5.0$ °C. Thermodynamically-allowed water conversion in hydrate forming emulsion is $X_{w-hyd} = 45\%$ and for ice-forming emulsion is

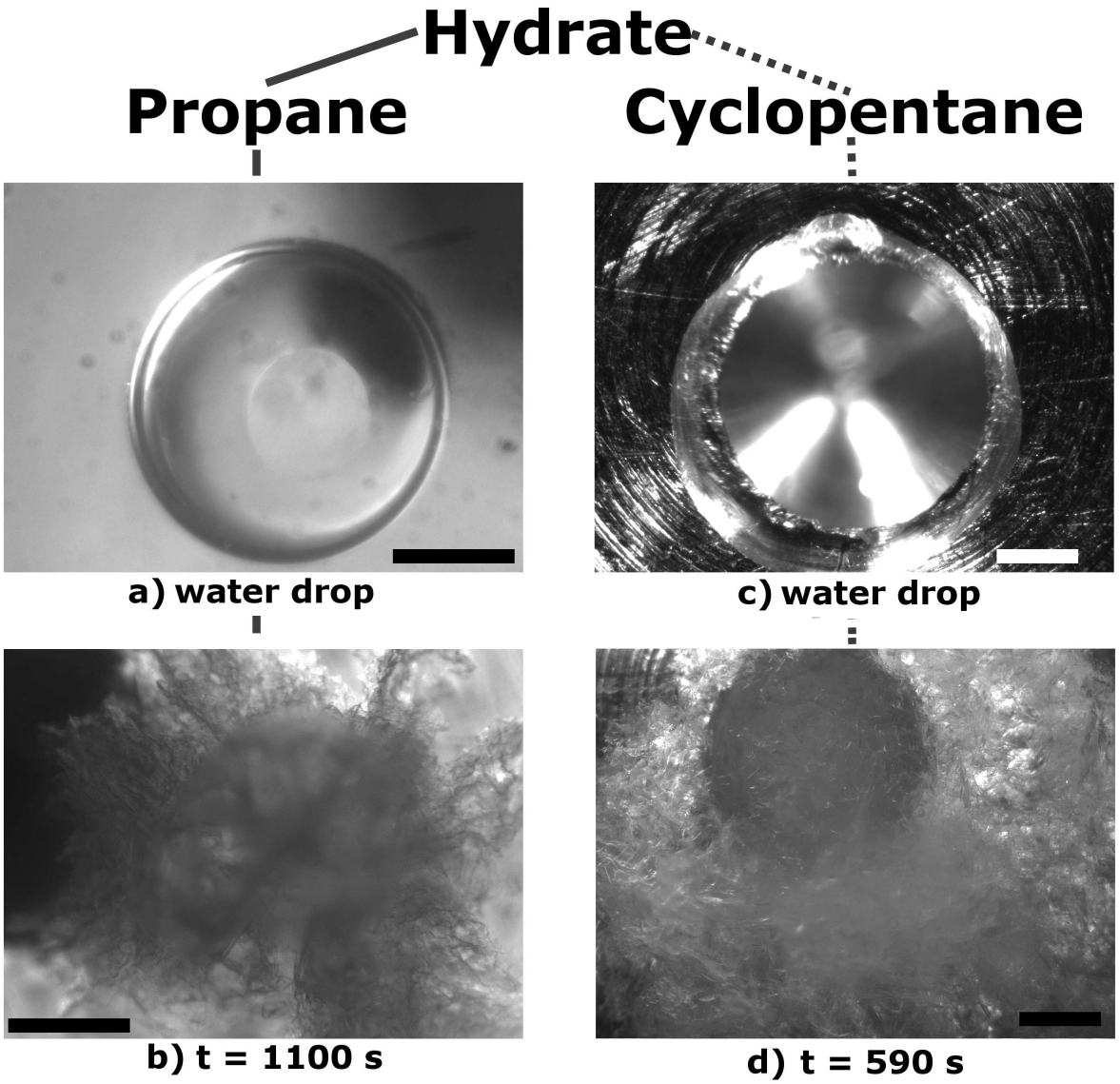

Figure 4.7: Morphology evolution of single water drop in oil containing propane (a,b) and cyclopentane (c,d).Scale bar is 300 μm.

Table 4.4: Initial subcoolings and thermodynamic water conversions for 15% (v/v) aqueous fraction hydrate- and ice-forming emulsions.

		Hydrate Slurry		Ice Slurry	
Salt Concentration X_{s-in} (% w/w)	Initial Subcooling ΔT_{in} (°C)	Experimental Temperature T_{exp} (°C)	Water Conversion X_{w-ice} (%)	Experimental Temperature T_{exp} (°C)	Water Conversion X_{w-hyd} (%)
0.0	10.4	-5.0	100	-10.4	100
7.5	5	-4.0	45	-9.8	49

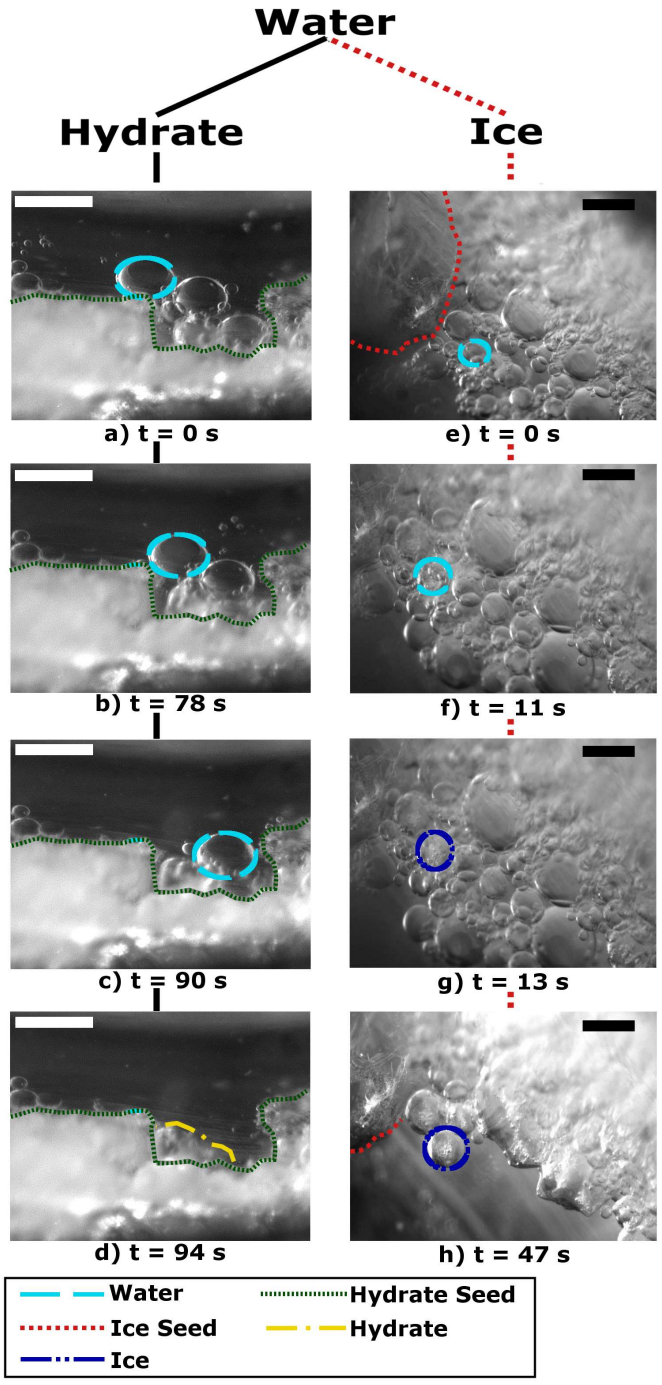

Figure 4.8: Morphology evolution of 15% (v/v) water ($X_{s-in} = 0.0\%$ (w/w)) hydrate- (a-d) and ice-forming (e-h) emulsions at subcooling of $\Delta T = 10.4$ °C. Thermodynamically-allowed conversion for the hydrate- and ice-forming emulsions is $X_w = 100\%$. Scale bar is 300 μm.

$X_{w-hyd} = 49\%$. In the hydrate-forming emulsion (figure 4.9(a-d)), hydrate starts forming at the water-oil interface [91, 101] (figure 4.9(b) and as it grows it punctures adjacent drops causing coalescence (figure 4.9(c,d)). Figure 4.10 shows the size of the drop after coalescence. Thus, the final structure formed in the hydrate-forming emulsion is a network of connected hydrate crystals which are wetted externally by brine (figure 4.9(d)). In contrast, ice grows in the bulk of the drop of the ice-forming emulsion (figure 4.9(f,g)). The brine-oil interface remains unaffected by the growth of ice as can be inferred by the comparison of interfaces of figure 4.9(e) and figure 4.9(h). Therefore, since the interface of the drops in the ice-forming emulsion does not change significantly, the mechanical interactions of these drops are not significantly affected until a certain conversion level is achieved. This morphological observations are consistent with the low viscosity increase (less than a factor of 2) of the ice-forming emulsions at $X_{w-ice} = 74\%$ where $\eta_{rel-ice} = 15.7$ compared to the viscosity at $X_{w-ice} = 12\%$ where $\eta_{rel-ice} = 7.7$; whereas hydrate-forming emulsion viscosity increases by 2 orders of magnitude at $X_{w-hyd} = 72\%$ where $\eta_{rel-hyd} = 5350$ compared to the viscosity at $X_{w-hyd} = 11\%$ where $\eta_{rel-hyd} = 9.2$.

The mechanisms of growth of crystals in hydrate- and ice-forming emulsions are schematically depicted in figure 4.11. Hydrate crystals grow at the oil-aqueous phase interface. The needle-like surface of hydrate punctures the aqueous drop. It should be noted that a needle-like hydrate structure forms when surfactants are present (e.g. an emulsion) and a faceted shell forms without surfactants [91]. Following puncturing, in the case of no salt, hydrate wets the hydrate seed and fully converts (figure 4.11(a1-a7)). In the presence of salt, the hydrate crystal grows at the interface and punctures the adjacent drops causing coalescence and wetting of the hydrate (figure 4.11(c1-c7)). Ice crystals are characterized by growth in the bulk of the aqueous phase. In the case of no salt, the whole aqueous drop freezes and it retains the spherical shape (figure 4.11(b1-b7)). When salt is present in the aqueous phase, ice grows in the bulk phase completely wetted by brine and the oil-aqueous phase remains largely unaffected (figure 4.11(d1-d7)).

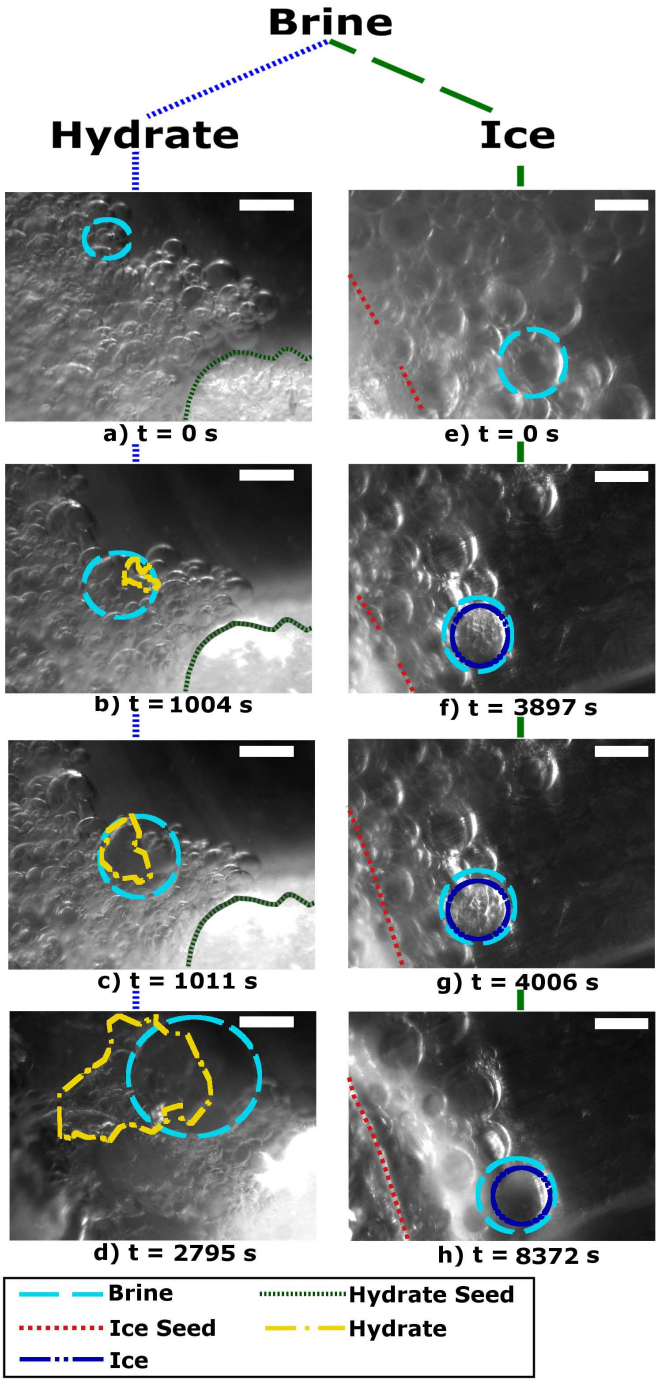

Figure 4.9: Morphology evolution of 15% (v/v) brine (X_{s-in} = 7.5% (w/w)) hydrate- (a-d) and ice-forming (e-h) emulsions at subcooling of ΔT = 5.0 °C. Thermodynamically-allowed conversion for the hydrate-forming emulsion is X_{w-hyd} = 45% and ice-forming emulsions is X_{w-ice} = 49%. Scale bar is 300 μm.

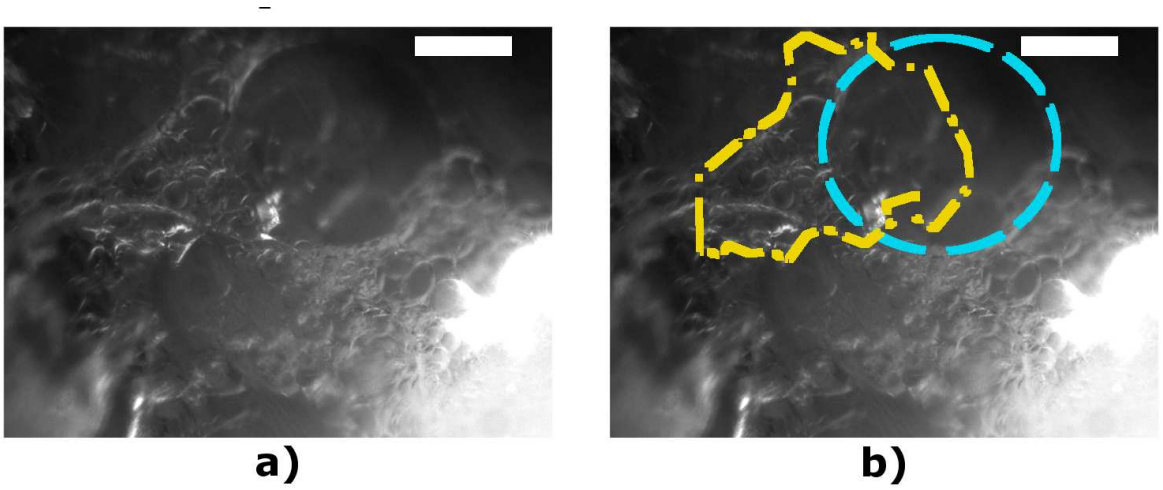

Figure 4.10: Final morphology of 15% (v/v) brine ($X_{s-in} = 7.5\%$ (w/w)) hydrate-forming emulsion, unmarked (a) and marked (b) photomicrographs, at subcooling of $\Delta T = 5.0$ °C and $t = 2795$ s. Thermodynamically-allowed conversion is $X_{w-hy} = 45\%$. Scale bar is 300 μm.

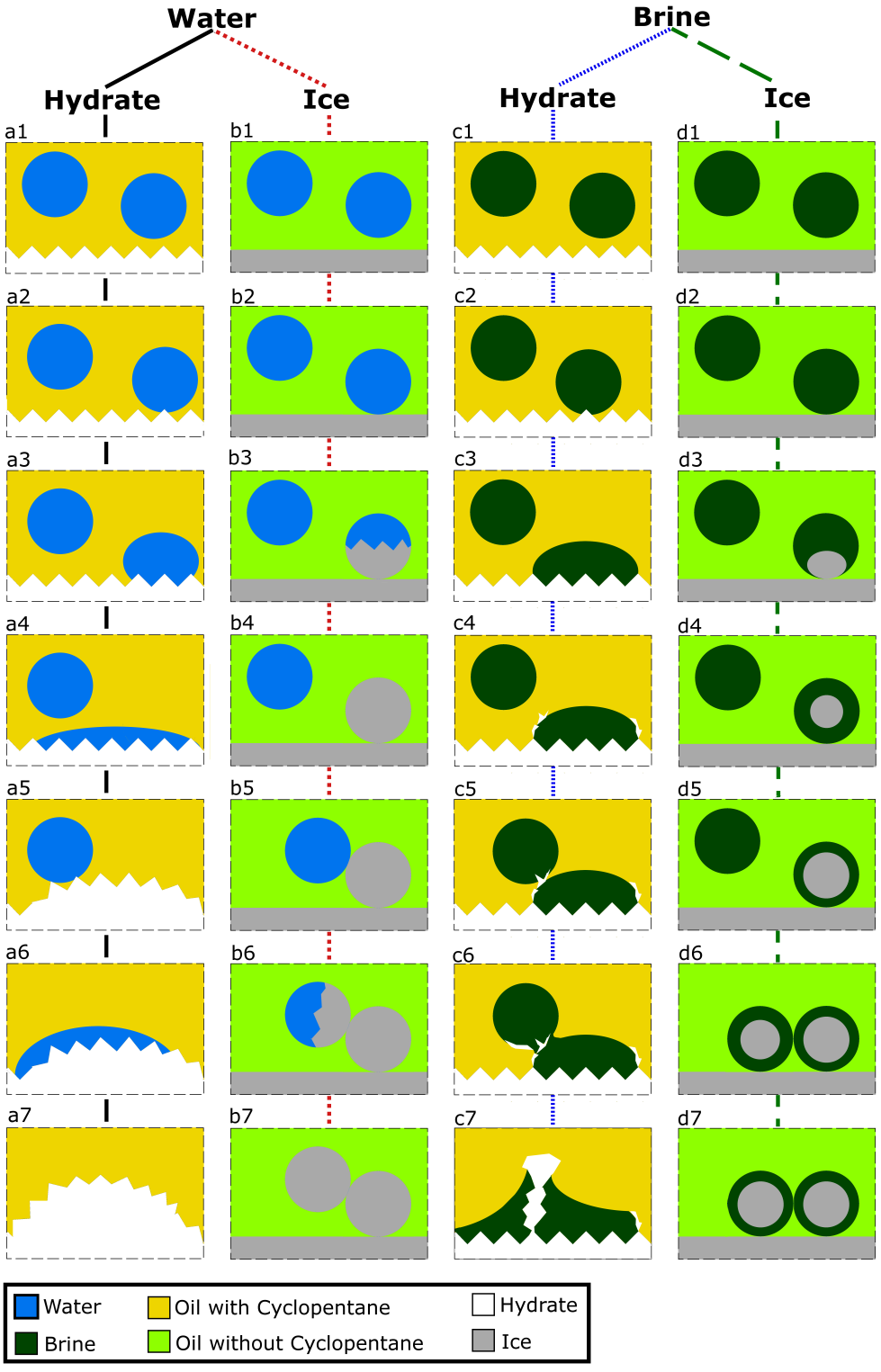

Figure 4.11: Schematic of the mechanisms of morphology evolution of hydrate- (a1-a7) and ice-forming (b1-b7) emulsions in the no salt case and hydrate- (c1-c7) and ice-forming (d1-d7) emulsions in the presence of salt.

4.4 Conclusion

We have investigated and compared two methods of modeling oilfield emulsions: cyclopentane hydrate- and ice-forming emulsions in terms of rheological properties, viscosity and yield stress, and morphology at various water conversions. Rheological and morphological results indicate that cyclopentane hydrate- and propane gas hydrate-forming emulsions are quite similar. For cyclopentane hydrate- ice-forming emulsions comparison, we have kept similar drop sizes and subcoolings. Water conversion was adjusted by varying the salt concentration in the aqueous phase. The relative viscosity of the cyclopentane hydrate-forming emulsion reaches up to approximately two orders of magnitude higher when compared to ice-forming emulsions. Yield stress of the cyclopentane hydrate-forming emulsion achieves up to three orders of magnitude higher values when compared to ice-forming emulsion. Both hydrate- and ice-forming emulsions exhibit non-thixotropic shear thinning behavior; hydrate slurry shear thinning behavior is more pronounced.

In order to understand the underlying physical phenomena causing the large difference in viscosity and yield stress between the hydrate- and ice-forming emulsions, we investigated and compared the emulsions morphology evolution. In the hydrate-forming emulsion under conditions of no salt, a hydrate crystal mass used as a seed punctures the aqueous drops in the emulsion and hydrate forms at the oil-aqueous phase interface as the whole drop wets the hydrate seed. In the presence of salt, hydrate forms at the interface and as it grows it punctures adjacent drops causing coalescence and wetting of the hydrate. In the ice-forming emulsion, no puncturing of the drop by the ice seed is observed. Ice grows in the bulk of the drop and the spherical shape is generally retained. In the presence of salt, ice is completely wetted by brine as it forms in the aqueous phase bulk, consequently the oil-aqueous phase interface remains intact. Therefore, the apparent difference in the mechanism of growth between hydrate and ice in the emulsions causes significantly different morphologies, thus resulting in very significant differences in

mechanical properties. The mechanical properties of hydrate-forming emulsions are not captured by the ice-forming emulsions and this is clearly shown by the large differences in rheological properties between the cyclopentane hydrate- and ice-forming emulsions. It may be possible to use ice slurries as a model of hydrate slurries of different solid fraction, i.e. formed from emulsions of different water fraction. However, this requires a study of the properties of both hydrate- and ice-forming emulsion conversion to slurries over a range of internal phase fraction, and is out of the scope of the present study.

5 Conclusion

5.1 Viscosity and yield stress peak dependence on water conversion

In Chapters 2 and 4, we have described techniques where water conversion to hydrate is controlled by varying initial salt concentration at a fixed temperature. The residual unconverted aqueous phase, which is present as brine, is in equilibrium with the hydrate. Thus, the study elucidates the interaction of three phases: solid hydrate, oil and brine. A peak in final structure viscosity and yield stress were observed for the 40% (v/v) aqueous fraction hydrate-forming emulsions at water to hydrate conversion of 61-85%. The observation of a maximum viscosity and yield stress at intermediate conversions indicates that residual brine may form capillary bridges between the hydrate particles. Therefore, both the concentrations of residual brine and solid are relevant to the rheological properties of the hydrate slurry. The role of brine in the slurry needs to be investigated further. In order to have a better understanding of the role of the brine in the slurry, solid hydrate concentration must be kept similar and residual brine concentration varied. Therefore, extension of the investigation of how the viscosity and yield stress vary with aqueous fraction may elucidate the interaction of residual brine with hydrate in a slurry.

5.2 Nucleation at the oil-aqueous phase interface

In Chapter 3, hydrate nucleation was observed to occur at the ice-oil-aqueous phase contact line. The concentration of water and hydrate-forming hydrocarbon, in our case cyclopentane, are present at an optimal concentration at the oil-aqueous phase interface. Thus, the fastest rate of hydrate nucleation and growth is at the oil-water interface. Our experiments show that the rate of single drop conversion to hydrate increases with more IOA contact line. Furthermore, addition of ice in a metastable hydrate-forming emulsion causes a rapid jump in viscosity. Like ice, others materials such as silica and clay have been reported to decrease hydrate nucleation time [130, 18, 131, 132, 133]. These materials may be investigated using the same experimental protocols as in Chapter 3. The efficiency of such materials to induce hydrate nucleation may be compared with existing hydrate and ice seed data. This information might be relevant in the field to eliminate components which induce hydrate nucleation. Other factors such as surface roughness and wettability by water or brine may be varied to determine whether they affect hydrate formation rate.

5.3 Drop puncturing and hydrate wetting mechanism

Hydrate slurry viscosity and yield stress values are of orders of magnitudes higher compared to ice-forming emulsion at similar water conversions. Thus, at the same aqueous fractions, ice-forming emulsions do not capture the mechanical properties of hydrate slurry. In Chapter 4, the large difference in rheological properties may be associated with the difference between the evolution of hydrate- and ice-forming emulsions. Hydrate is characterized by an interfacial growth, where water and cyclopentane are at an optimal concentration, while freezing of water into ice occurs in the bulk aqueous phase. Hydrate formation mechanism is characterized by an apparent puncturing of emulsion drops by hydrate needle-like structure, thus causing wetting of the hydrate. Such puncturing mechanism is not observed in the case of ice-forming emulsions. The spherical shape of

the drop is retained when ice particles are formed, whereas a mushy/hairy structure is observed in hydrate slurries. The mechanism of puncturing and wetting of the hydrate-forming emulsion is currently very poorly understood. The role that the surfactants play in the stabilization of hydrate growth at the water-oil interface need to be investigated. Furthermore, understanding the surfactant-crystal interaction is important in characterizing the slurry.

In order to achieve a clarification of the puncturing mechanism, needle-like ice formation, if possible, may be required to test whether the geometrical factor of the surface is critical rather than the interfacial energy difference between hydrate and ice. In order for a conclusive experiment to be conducted a few factors such as the density and sharpness of the hydrate needles need to be controlled. The surface roughness of the hydrate needs to be qualitatively estimated. Alternatively, a molecular dynamics simulation may be required to capture certain aspects of the interaction between the drop and the crystal surface. In the presence of brine, the growth of hydrate at the interface and its interaction with surfactant at the oil-aqueous interface is unknown. The mechanism by which hydrate causes coalescence needs to be mechanistically explored. If surfactants adsorb on the hydrate crystal, then the effectiveness of the hydrate crystal penetrating the adjacent surfactant-covered drop is of interest. The puncturing of drop needs to be explored at other surfactant concentrations to check whether a variation in hydrate formation rate in the emulsion is observed. Slowing down the process of interaction between hydrate crystals and aqueous drops may slow hydrate formation rate and could be directly relevant to the oil and gas industry to prevent pipeline plugging.

5.4 Modeling hydrate slurry flow in a pipe

The results discussed in this thesis may be used to estimate pressure drop (ΔP) in a pipe using the Hagen-Poiseuille equation [97]

$$-dP = \frac{128Q\eta(z)dz}{\pi d^4}, \tag{5.1}$$

where $\eta(z)$ is the hydrate-forming emulsion viscosity at a distance z in the pipe, Q is the volumetric flow rate and d is the pipe diameter. The average velocity of the hydrate-forming emulsion in the pipe is $v_{avg} = \frac{4Q}{\pi d^2}$.

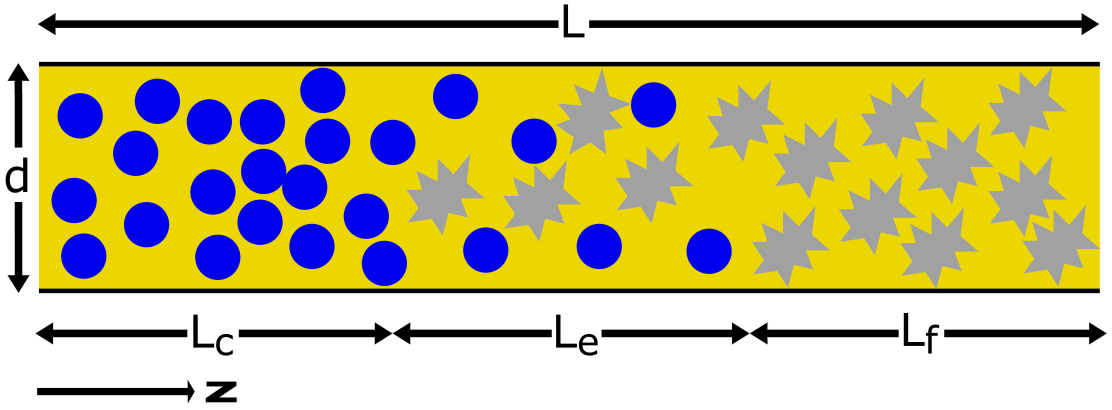

Figure 5.1: Schematic of hydrate-forming emulsion plug flow in a pipe.

Assuming a plug flow model in the pipe, the length at which the viscosity remains equal to initial hydrate-forming emulsion viscosity ($\eta(z) = \eta_{in}$) is $L_c = v_{avg}t_c$ (figure 5.1), where t_c is critical time as discussed in Chapter 2. Thus, the total drop in pressure at a distance $z \leq L_c$ is

$$-\Delta P(z) = \frac{128Q\eta_{in}z}{\pi d^4}. \tag{5.2}$$

At $z = L_c$, the total drop in pressure is

$$-\Delta P_c = \frac{128Q\eta_{in}L_c}{\pi d^4}, \tag{5.3}$$

which may be written in terms of critical time as

$$-\Delta P_c = \frac{512Q^2\eta_{in}t_c}{\pi^2 d^6}. \tag{5.4}$$

As shown in figure 5.1, following critical length L_c, the length in the pipe at which viscosity evolution ($\eta(z)$) from initial viscosity (η_{in}) to final viscosity (η_f) occurs is $L_e = v_{avg}t_e$. Viscosity evolution ($\eta(z)$) corresponds to $\eta(t)$ in our rheological experiments given the plug flow model time-space relation $t = \frac{\pi d^2(z-L_c)}{4Q}$. The viscosity during evolution time may be written as an exponential function of time with boundary conditions $\eta(t_c) = \eta_{in}$ and $\eta(t_c + t_e) = \eta_f$ as

$$\eta(t) = \eta_{in}e^{\ln\left(\frac{\eta_f}{\eta_{in}}\right)\left(\frac{t-t_c}{t_e}\right)}, \tag{5.5}$$

and may be expressed in terms of position z with boundary conditions $\eta(L_c) = \eta_{in}$ and $\eta(L_c + L_e) = \eta_f$ as

$$\eta(z) = \eta_{in}e^{\ln\left(\frac{\eta_f}{\eta_{in}}\right)\left(\frac{\pi d^2 z - 4Qt_c}{4Qt_e}\right)}. \tag{5.6}$$

Therefore the total drop in pressure at a distance z where $L_c \leq z \leq L_c + L_e$ is $-\Delta P = -\Delta P_c + \int_{L_c}^{z} \frac{128Q\eta(z)dz}{\pi d^4}$ and after solving for integral it may be written as

$$-\Delta P(z) = \frac{512Q^2\eta_{in}}{\pi^2 d^6}\left(t_c + \frac{t_e}{\ln\left(\frac{\eta_f}{\eta_{in}}\right)}\left(\left(\frac{\eta_f}{\eta_{in}}\right)^{\left(\frac{\pi d^2 z - 4Qt_c}{4Qt_e}\right)} - 1\right)\right). \tag{5.7}$$

At length $z = L_c + L_e$, the total drop in pressure is

$$-\Delta P_{c+e} = \frac{512Q^2\eta_{in}}{\pi^2 d^6}\left(t_c + \frac{t_e}{\ln\left(\frac{\eta_f}{\eta_{in}}\right)}\left(\frac{\eta_f}{\eta_{in}} - 1\right)\right). \tag{5.8}$$

As depicted in figure 5.1, following viscosity evolution section of the pipe (L_e), the length where viscosity is equal to final viscosity ($\eta(z) = \eta_f$) is $L_f = L - L_c - L_e$, where

L is the total length of the pipe. The total drop in pressure at distance $z \geq L_c + L_e$ is

$$-\Delta P(z) = \frac{512Q^2\eta_{in}}{\pi^2 d^6}\left(t_c + \frac{t_e}{\ln\left(\frac{\eta_f}{\eta_{in}}\right)}\left(\frac{\eta_f}{\eta_{in}} - 1\right) + \frac{\eta_f}{\eta_{in}}\left(\frac{\pi d^2 z}{4Q} - t_c - t_e\right)\right). \tag{5.9}$$

Thus, the total pressure drop at total length of a pipe $z = L$ where $L > L_c + L_e$ is

$$-\Delta P_L = \frac{512Q^2\eta_{in}}{\pi^2 d^6}\left(t_c + \frac{t_e}{\ln\left(\frac{\eta_f}{\eta_{in}}\right)}\left(\frac{\eta_f}{\eta_{in}} - 1\right) + \frac{\eta_f}{\eta_{in}}\left(\frac{\pi d^2 L}{4Q} - t_c - t_e\right)\right). \tag{5.10}$$

Equation 5.10 directly estimates total pressure drop in a pipe with a length $L > L_c + L_e$ utilizing viscosity evolution parameters discussed in this thesis.

In figure 5.2, the lower and upper bound of pressure drop in a pipe are plotted along with the pressure drop predicted by equations 5.2, 5.7 and 5.9. The lower bound of pressure drop represents the hypothetical case in which the hydrate-forming emulsion critical time is infinite, thus the viscosity throughout the whole length of the pipe is equal to initial viscosity ($\eta(z) = \eta_{in} = 0.01$ Pa s). The upper bound of pressure drop represents the case of the hydrate-forming emulsion in which critical and evolution time is equal to zero, thus the viscosity throughout the whole length of the pipe is equal to the final viscosity ($\eta(z) = \eta_f = 1$ Pa s). Initial and final viscosity values are taken from figure 2.8. As shown in figure 5.2, based on the plug flow equations 5.2, 5.7 and 5.9, the evolution of total pressure drop is equal to the lower bound estimate for $z \leq L_c$; at $z = L_c$, pressure drop starts deviating from the lower bound, thus increasing at higher rates; at $L_c \leq z \leq L_c + L_e$, as total pressure drop deviates from lower bound, its value comes closer to upper bound pressure drop; at $z \geq L_c + L_e$, pressure drop closely approaches the upper bound pressure drop with increasing distance z.

The effect of average velocity, i.e. the ratio of volumetric flowrate to the square of the diameter ($v_{avg} = \frac{4Q}{\pi d^2}$) on total pressure drop evolution in a pipe is shown in figure 5.3. At larger average velocity (i.e., larger volumetric flow rates or lower pipe diameters), the

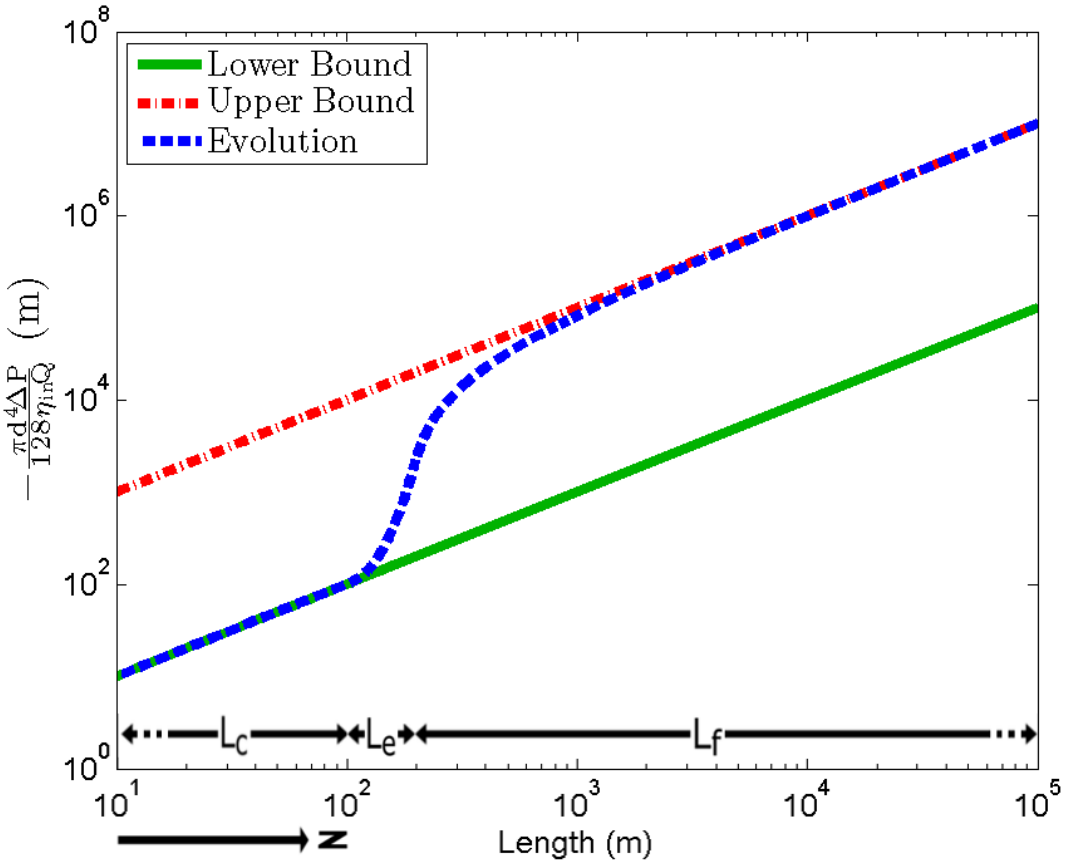

Figure 5.2: Plug flow model pressure drop evolution in a pipe. Initial viscosity is $\eta_{in} = 0.01$ Pa s; final viscosity is $\eta_f = 1$ Pa s; critical time is $t_c = 100$ s; evolution time is $t_e = 100$ s; average velocity is $v_{avg} = 1$ m s^{-1}; critical length is $L_c = 100$ m; and evolution length is $L_e = 100$ m.

transition starts at a longer distance ($z = L_c$) and the evolution from lower to upper pressure drop bound occurs at a longer evolution length (L_e).

The effect of critical time in a pipe is shown in figure 5.4. At larger critical time, the transition from lower to upper starts at longer distance ($z = L_c$). The evolution length (L_e) from lower to upper pressure drop bound remains the same.

The effect of evolution time in a pipe is shown in figure 5.5. At larger evolution time, the transition from lower to upper starts at same distance ($z = L_c$) but the evolution from lower to upper pressure drop bound occurs at a larger length (L_e).

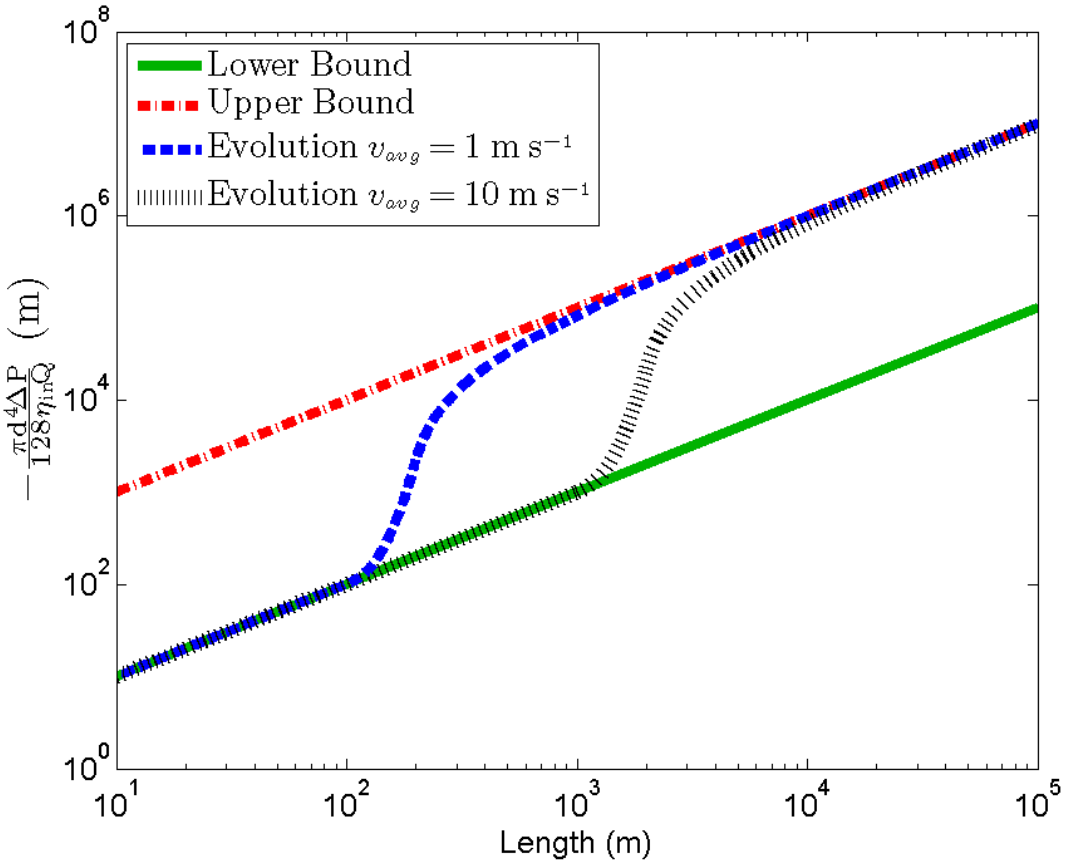

Figure 5.3: The effect of average velocity $v_{avg} = \frac{4Q}{\pi d^2}$ on pressure drop evolution. Initial viscosity is $\eta_{in} = 0.01$ Pa s; final viscosity is $\eta_f = 1$ Pa s; critical time is $t_c = 100$ s; and evolution time is $t_e = 100$ s.

Thus, in order to minimize the drop in pressure in a pipe, flowline needs to be run at conditions which favor higher average velocities (i.e. higher volumetric flow rates) and longer critical and evolution times.

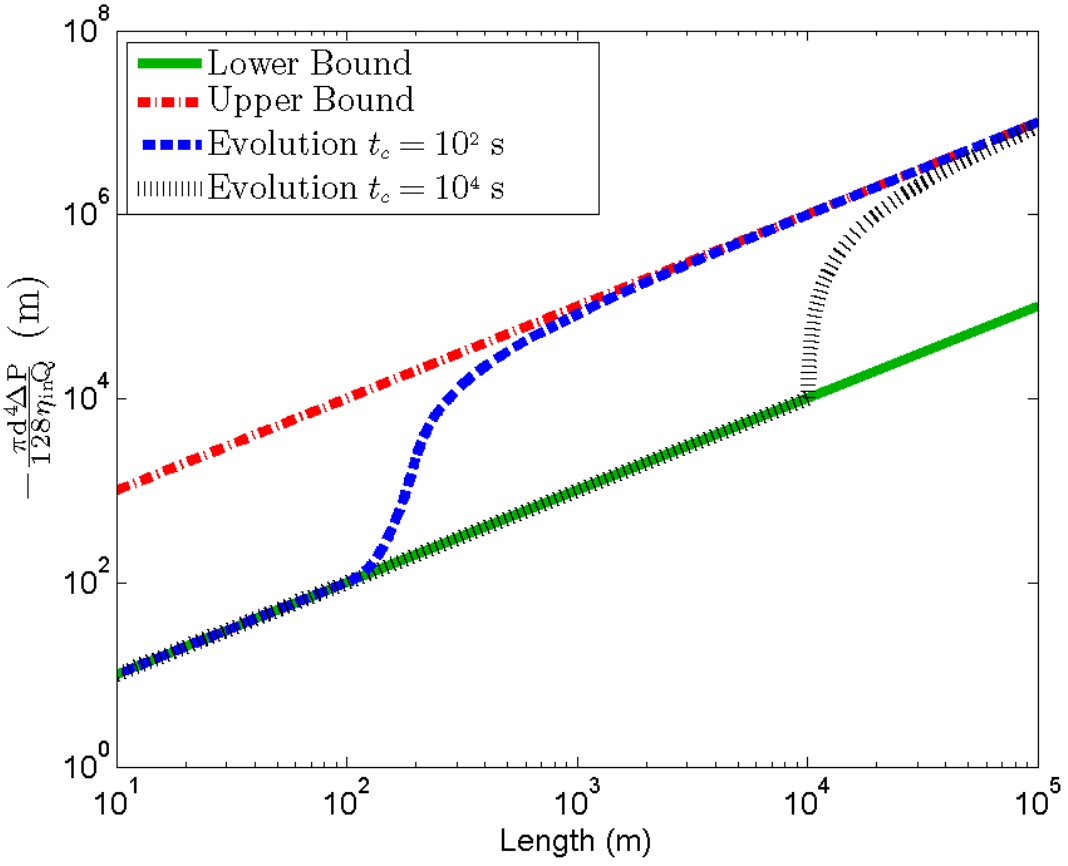

Figure 5.4: The effect of critical time t_c on pressure drop evolution. Initial viscosity is η_{in} = 0.01 Pa s; final viscosity is η_f = 1 Pa s; evolution time is t_e = 100 s; and average velocity is v_{avg} = 1 m s^{-1}.

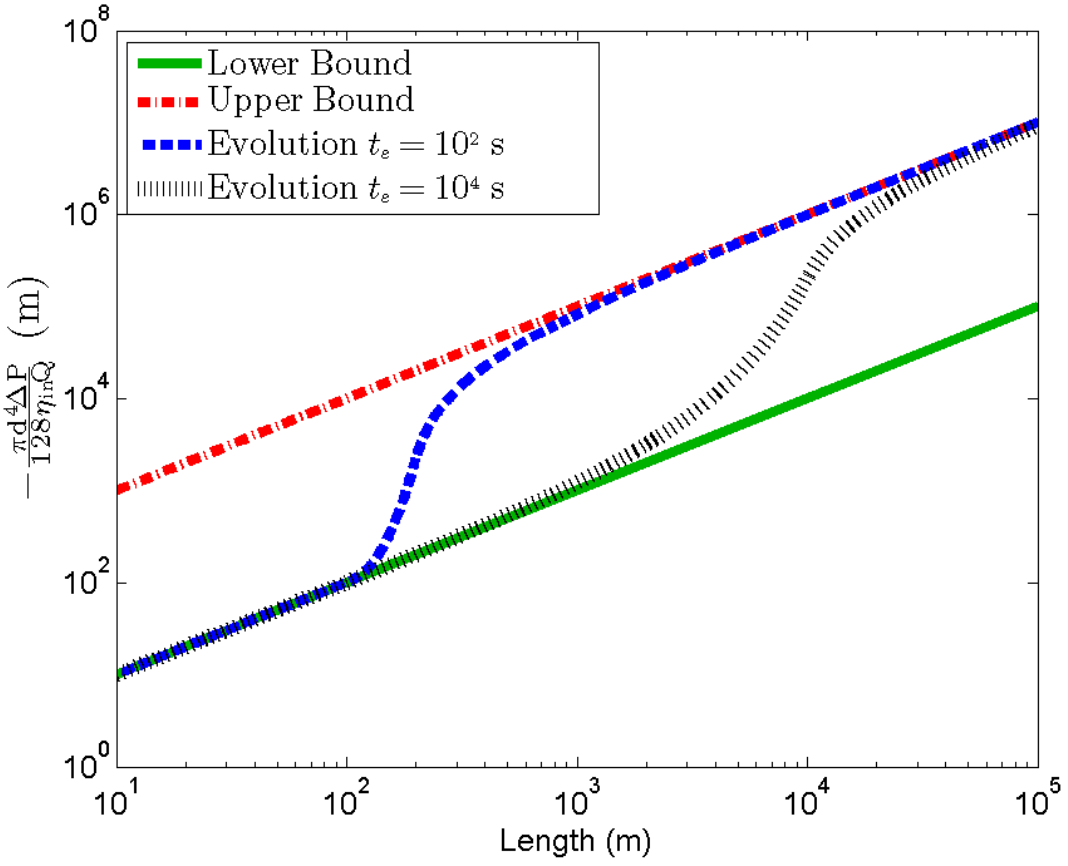

Figure 5.5: The effect of evolution time t_e on pressure drop evolution. Initial viscosity is $\eta_{in} = 0.01$ Pa s; final viscosity is $\eta_f = 1$ Pa s; critical time is $t_c = 100$ s; and average velocity is $v_{avg} = 1$ m s^{-1}.

Bibliography

[1] H. Stephen and T. Stephen. *Solubilities of inorganic and organic compounds.*, volume I. Macmillan, New York, 1963.

[2] P. J. Rensing, M. W. Liberatore, A. K. Sum, C. A. Koh, and E. D. Sloan. Viscosity and yield stresses of ice slurries formed in water-in-oil emulsions. *J. Non-Newtonian Fluid Mech.*, 166:859–866, 2011.

[3] E. G. Hammerschmidt. Formation of gas hydrates in natural gas transmission lines. *Ind. Eng. Chem.*, 26(8):851–855, 1934.

[4] E. D. Sloan. A changing hydrate paradigm-from apprehension to avoidance to risk management. *Fluid Phase Equilib.*, 228–229:67–74, 2005.

[5] E. D. Sloan, C. A. Koh, A. K. Sum, N. D. McMullen, G. Shoup, A. L. Ballard, and T. Palermo. *Natural gas hydrates in flow assurance.* Gulf Professional Publishing, Elsevier Inc., 2011.

[6] E. D. Sloan and C. A. Koh. *Clathrate hydrates of natural gases.* CRC Press, Taylor & Francis Group, 3rd edition, 2008.

[7] I. Chatti, A. Delahaye, L. Fournaison, and J. -P Petitet. Benefits and drawbacks of clathrate hydrates: a review of their areas of interest. *Energy Convers. Manage.*, 46:1333–1343, 2005.

[8] P. R. Bishnoi and P. D. Dholabhai. Equilibrium conditions for hydrate formation for a ternary mixture of methane, propane and carbon dioxide, and a natural gas mixture in the presence of electrolytes and methanol. *Fluid Phase Equilib.*, 158–160:821–827, 1999.

[9] M. D. Jager, C. J. Peters, and E. D. Sloan. Experimental determination of methane hydrate stability in methanol and electrolyte solutions. *Fluid Phase Equilib.*, 193:17–28, 2002.

[10] F. Dong, X. Zang, D. Li, and S. Fan amd D. Liang. Experimental investigation on propane hydrate dissociation by high concentration methanol and ethylene glycol solution injection. *Energy Fuels*, 23:1563–1567, 2009.

[11] X. Li, H. Wu, and P. Englezos. Prediction of gas hydrate formation conditions in the presence of methanol, glycerol, ethylene glycol, and triethylene glycol with the statistical associating fluid theory equation of state. *Ind. Eng. Chem. Res.*, 45:2131–2137, 2006.

[12] J. Y. Zuo, D. Zhang, and H.-J. Ng. Representation of hydrate phase equilibria in aqueous solutions of methanol and electrolytes using an equation of state. *Energy Fuels*, 14:19–24, 2000.

[13] Z. G. Sun, S. S. Fan, L. Shi, Y. K. Guo, and K. H. Guo. Equilibrium conditions hydrate dissociation for a ternary mixture of methane, ethane, and propane in aqueous solutions of ethylene glycol and electrolytes. *J. Chem. Eng. Data*, 46:927–929, 2001.

[14] E. Mahmoodaghdam and P. R. Bishnoi. Equilibrium data for methane, ethane, and propane incipient hydrate formation in aqueous solutions of ethylene glycol and diethylene glycol. *J. Chem. Eng. Data*, 47:278–281, 2002.

[15] Q. Yuan, C. Sun, X. Yang, P. Ma, Z. Ma, Q. Li, and G. Chen. Gas production from methane-hydrate-bearing sands by ethylene glycol injection using a three-dimensional reactor. *Energy Fuels*, 25:3108–3115, 2011.

[16] L. D. Villano, M. A. Kelland, G. M. Miyake, and E. Y.-X. Chen. Effect of polymer tacticity on the performance of poly(n,n-dialkylacrylamide)s as kinetic hydrate inhibitors. *Energy Fuels*, 24:2554–2562, 2010.

[17] H. Ajiro, Y. Takemoto, M. Akashi, P. C. Chua, and M. A. Kelland. Study of the kinetic hydrate inhibitor performance of a series of poly-(N-alkyl-N-vinylacetamide)s. *Energy Fuels*, 24:6400–6410, 2010.

[18] M. A. Kelland. History of the development of low dosage hydrate inhibitors. *Energy Fuels*, 20:825–847, 2006.

[19] P. Englezos. Clathrate hydrates. *Ind. Eng. Chem. Res.*, 32:1251–1274, 1993.

[20] A. K. Sum, C. A. Koh, and E. D. Sloan. Clathrate hydrates: from laboratory science to engineering practice. *Ind. Eng. Chem. Res.*, 48:7457–7465, 2009.

[21] S. Yang, D. M. Kleehammer, Z. Huo, E. D. Sloan, and K. T. Miller. Temperature dependence of particle-particle adherence forces in ice and clathrate hydrates. *J. Colloid Interface Sci.*, 277:335–341, 2004.

[22] Z. M. Aman, S. E. Joshi, E. D. Sloan, A. K. Sum, and C. A. Koh. Micromechanical cohesion force measurements to determine cyclopentane hydrate interfacial properties. *J. Colloid Interface Sci.*, 376:283–288, 2012.

[23] E. D. Sloan. Introductory overview: hydrate knowledge development. *Am. Mineral.*, 89:1155–1161, 2004.

[24] K. A. Udachin, C. I. Ratcliffe, and J. A. Ripmeester. A dense and efficient clathrate hydrate structure with unusual cages. *Angew. Chem.*, 40:1303–1305, 2001.

[25] C. A. Koh, E. D. Sloan, A. K. Sum, and D. T. Wu. Fundamentals and applications of gas hydrates. *Annu. Rev. Chem. Biomol. Eng.*, 2:237–257, 2011.

[26] A. V. Milkov. Global estimates of hydrate-bound gas in marine sediments: how much is really out there? *Earth-Sci. Rev.*, 66:183–197, 2004.

[27] P. G. Brewer. Gas hydrates and global climate change. *Ann. N. Y. Acad. Sci.*, 912:195–199, 2000.

[28] J. Bohannon. Weighing the climate risks of an untapped fossil fuel. *Science*, 319:1753, 2008.

[29] D. J. Wuebbles and K. Hayhoe. Atmospheric methane and global change. *Earth-Sci. Rev.*, 57:177–210, 2002.

[30] H. K. Srivastava and G. N. Sastry. Viability of clathrate hydrates as co_2 capturing agents: a theoretical study. *J. Phys. Chem. A*, 115:7633–7637, 2011.

[31] N. Goel. In situ methane hydrate dissociation with carbon dioxide sequestration: Current knowledge and issues. *J. Pet. Sci. Eng.*, 51:169–184, 2006.

[32] R. Kumar, H. Wu, and P. Englezos. Incipient hydrate phase equilibrium for gas mixtures containing hydrogen, carbon dioxide and propane. *Fluid Phase Equilib.*, 244:167–171, 2006.

[33] J. S. Zhang and J. W. Lee. Equilibrium of hydrogen + cyclopentane and carbon dioxide + cyclopentane binary hydrates. *J. Chem. Eng. Data*, 54:659–661, 2009.

[34] T. J. Frankcombe and G.-J. Kroes. A new method for screening potential sii and sh hydrogen clathrate hydrate promoters with model potentials. *Phys. Chem. Chem. Phys.*, 13:13410–13420, 2011.

[35] K. M. Sabil, G.-J. Witkamp, and C. J. Peters. Phase equilibria in ternary (carbon dioxide + tetrahydrofuran + water) system in hydrate-forming region: Effects of carbon dioxide concentration and the occurrence of pseudo-retrograde hydrate phenomenon. *J. Chem. Thermodyn.*, 42:8–16, 2010.

[36] D. Denderen, E. Ineke, and M. Golombok. Co_2 removal from contaminated natural gas mixtures by hydrate formation. *Ind. Eng. Chem. Res.*, 48:5802–5807, 2009.

[37] L. A. Stern, S. Circone, and S. H. Kirby. Anomalous preservation of pure methane hydrate at 1 atm. *J. Phys. Chem. B*, 105:1756–1762, 2001.

[38] G. M. von Medeaz. Water desalination as a long-term sustainable solution to alleviate global freshwater scarcity? A North-South approach. *Desalination*, 169:287–301, 2004.

[39] K. Park, S. Y. Hong, J. W. Lee, K. C. Kang, Y. C. Lee, M.-G. Ha, and J. D. Lee. A new apparatus for seawater desalination by gas hydrate process and removal characteristics of dissolved minerals (na^+, mg^{+2}, ca^{+2}, k^+, b^{+3}). *Desalination*, 274:91–96, 2011.

[40] T. Ogawa, T. Ito, K. Watanabe, K. Tahara, R. Hiraoka, J. Ochiai, R. Ohmura, and Y. H. Mori. Development of a novel hydrate-based refrigeration system: A preliminary overview. *Appl. Therm. Eng.*, 26:2157–2167, 2006.

[41] A. Delahaye, L. Fournaison, S. Jerbi, and N. Mayoufi. Rheological properties of co_2 hydrate slurry flow in the presence of additives. *Ind. Eng. Chem. Res.*, 50:8344–8353, 2011.

[42] G. Li, D. Liu, and Y. Xie. Study on thermal properties of TBAB-THF hydrate mixture for cold storage by DSC. *Chem. Eng. Sci.*, 102:819–826, 2010.

[43] P. Zhang, Z. W. Ma, and R. Z. Wang. An overview of phase change material slurries: MPCS and CHS. *Renew. Sust. Energ. Rev.*, 14:598–614, 2010.

[44] F. Takeuchi, R. Ohmura, and K. Yasuoka. Statistical-thermodynamics modeling of clathrate-hydrate-forming systems suitable as working media of a hydrate-based refrigeration system. *Int. J. Thermophys.*, 30:1838–1852, 2009.

[45] A. Delahaye, L. Fournaison, S. Marinhas, and M. C. Martinez. Rheological study of CO_2 hydrate slurry in a dynamic loop applied to secondary refrigeration. *Chem. Eng. Sci.*, 63:3551–3559, 2008.

[46] S. Marinhas, A. Delahaye, and L. Fournaison. Solid fraction modelling for CO_2 and CO_2-thf hydrate slurries used as secondary refrigerants. *Int. J. Refrig.*, 30:758–766, 2007.

[47] L. Fournaison, A. Delahaye, and I. Chatti. CO_2 hydrates in refrigeration processes. *Ind. Eng. Chem. Res.*, 43:6521–6526, 2004.

[48] G. Zylyftari, J. W. Lee, and J. F. Morris. Salt effects on thermodynamic and rheological properties of hydrate forming emulsions. *Chem. Eng. Sci.*, 95:148–160, 2013.

[49] R. Sun and Z. Duan. An accurate model to predict the thermodynamic stability of methane hydrate and methane solubility in marine environments. *Chem. Geol.*, 244:248–262, 2007.

[50] A. H. Mohammadi and D. Richon. Thermodynamic modeling of salt precipitation and gas hydrate inhibition effect of salt aqueous solution. *Ind. Eng. Chem. Res.*, 46:5074–5079, 2007.

[51] H. T. Nguyen, N. Kommareddi, and V. T. John. A thermodynamic model to

predict clathrate hydrate formation in water-in-oi microemulsion systems. *J. Colloid Interface Sci.*, 155:428–487, 1993.

[52] W. R. Parrish and J. M. Prausnitz. Dissociation pressures of gas hydrates formed by gas mixtures. *Ind. Eng. Chem. Process Des. Dev.*, 11(1):26–35, 1972.

[53] R. Sakemoto, H. Sakamoto, K. Shiraiwa, R. Ohmura, and T. Uchida. Clathrate hydrate crystal growth at the seawater/hydrophobic-guest-liquid interface. *Cryst. Growth Des.*, 10(3):1296–1300, 2010.

[54] M. Kishimoto, S. Iijima, and R. Ohmura. Crystal growth of clathrate hydrate at the interface between seawater and hydrophobic-guest liquid: effect of elevated salt concentration. *Ind. Eng. Chem. Res.*, 51:5224–5229, 2012.

[55] K. Maeda, Y. Katsura, Y. Asakuma, and K. Fukui. Concentration of sodium chloride in aqueous solution by chlorodifluoromethane gas hydrate. *Chem. Eng. Process.*, 47:2281–2286, 2008.

[56] T. Uchida, I. Y. Ikeda, S. Takeya, T. Ebinuma, J. Nagao, and H. Narita. CO_2 hydrate film formation at the boundary between CO_2 and water: effects of temperature, pressure and additives on the formation rate. *J. Cryst. Growth*, 237–239:383–387, 2002.

[57] E. Colombel, P. Gateau, L. Barre, F. Gruy, and T. Palermo. Discussion of agglomeration mechanisms between hydrate particles in water in oil emulsions. *Oil Gas Sci. Technol.*, 64(5):629–636, 2009.

[58] A. Sinquin, T. Palermo, and Y. Peysson. Rheological and flow properties of gas hydrate suspensions. *Oil Gas Sci. Technol.*, 59(1):41–57, 2004.

[59] P. Mills. Non-Newtonian behaviour of flocculated suspensions. *J. Physique Lett.*, 46:L–301–L–309, 1985.

[60] T. Yoshioka, B. Sternbergb, and A. T. Florence. Preparation and properties of vesicles (niosomes) of sorbitan monoesters (Span 20, 40, 60 and 80) and a sorbitan triester (Span 85). *Drug Dev. Ind. Pharm.*, 24:1049–1054, 1998.

[61] K. Kato, P. Walde, N. Koine, S. Ichikawa, T. Ishikawa, R. Nagahama, T. Ishihara, T. Tsujii, M. Shudou, Y. Omokawa, and T. Kuroiwa. Temperature-sensitive nonionic vesicles prepared from Span 80 (sorbitan monooleate). *Langmuir*, 24:10762–10770, 2008.

[62] J. Peixinho, P. U. Karanjkar, J. W. Lee, and J. F. Morris. Rheology of hydrate forming emulsions. *Langmuir*, 26(14):11699–11704, 2010.

[63] P. Le Parlouër, C. Dalmazzone, B. Herzhaft, L. Rousseau, and C. Mathonat. Characterisation of gas hydrates formation using a new high pressure micro-DSC. *J. Therm. Anal. Calorim.*, 78:165–172, 2004.

[64] P. U. Karanjkar, J. W. Lee, and J. F. Morris. Calorimetric investigation of cyclopentane hydrate formation in an emulsion. *Chem. Eng. Sci.*, 68:481–491, 2012.

[65] F. O. Opawale and D. J. Burgess. Influence of interfacial properties of lipophilic surfactants on water-in-oil emulsion stability. *J. Colloid Interface Sci.*, 197:142–150, 1998.

[66] A. -M O. Mohamed, M. El Gamal, and A. Y. Zekri. Effect of salinity and temperature on water cut determination in oil reservoirs. *J. Petrol. Sci. Eng.*, 40:177–188, 2003.

[67] S. H. Standal, A. M. Blokhus, J. Haavik, A. Skauge, and T. Barth. Partition coefficients and interfacial activity for polar components in oil/water model systems. *J. Colloid Interface Sci.*, 212:33–41, 1999.

[68] Y. Levin and J. E. Flores-Mena. Surface tension of strong electrolytes. *Europhys. Lett.*, 56(2):187–192, 2001.

[69] H. A. Stone. Dynamics of drop deformation and breakup in viscous fluids. *Annu. Rev. Fluid Mech.*, 26:65–102, 1994.

[70] R. Pal. Shear viscosity behavior of emulsions of two immiscible liquids. *J. Colloid Interface Sci.*, 225:359–366, 2000.

[71] J. F. Richardson and W. N. Zaki. Sedimentation and fluidisation. Part 1. *Trans. Inst. Chem. Eng.*, 32:35–53, 1954.

[72] R. H. Davis and A. Acrivos. Sedimentation of noncolloidal particles at low Reynolds numbers. *Annu. Rev. Fluid Mech.*, 17:91–118, 1985.

[73] S. Koo. Estimation of hindered settling velocity of suspensions. *J. Ind. Eng. Chem.*, 15:45–49, 2009.

[74] M. -C Yang, L. E. Scriven, and C. W. Macosko. Some rheological measurements on magnetic iron oxide suspensions in silicone oil. *J. Rheol.*, 30(5):1015–1029, 1986.

[75] L. Ballard and E. D. Sloan. The next generation of hydrate prediction IV. A comparison of available hydrate prediction programs. *Fluid Phase Equilib.*, 216:257–270, 2004.

[76] A. Peneloux, E. Rauzy, and R. Freeze. A consistent correction for Redlich-Kwong-Soave volumes. *Fluid Phase Equilib.*, 8(1):7–23, 1982.

[77] Y. Zhang, P. G. Debenedetti, R. K. Prud'homme, and B. A. Pethica. Differential scanning calorimetry studies of clathrate hydrate formation. *J. Phys. Chem. B*, 108:16717–16722, 2004.

[78] J. W. Mullin. *Crystallization.* Butterworth-Heinemann, Oxford, U.K., 3rd edition, 1993.

[79] D. Clausse. Differential thermal analysis, differential scanning calorimetry, and emulsions. *J. Therm. Anal. Calorim.*, 101:1071–1077, 2010.

[80] M. Matsumoto, S. Saito, and I. Ohmine. Molecular dynamics simulation of the ice nucleation and growth process leading to water freezing. *Nature*, 416:409–413, 2002.

[81] R. Ohmura, M. Ogawa, K. Yasuoka, and Y. H. Mori. Statistical study of clathrate-hydrate nucleation in a water/hydrochlorofluorocarbon system: search for the nature of the "memory effect". *J. Phys. Chem. B*, 107:5289–5293, 2003.

[82] M. Nakajima, R. Ohmura, and Y. H. Mori. Clathrate hydrate formation from cyclopentane-in-water emulsions. *Ind. Eng. Chem. Res.*, 47:8933–8939, 2008.

[83] S. S. Fan, D. Q. Liang, and K. H. Guo. Hydrate equilibrium conditions for cyclopentane and a quaternary cyclopentane-rich mixture. *J. Chem. Eng. Data*, 46:930–932, 2001.

[84] J. G. Dash, F. Haiying, and J. S. Wettlaufer. The premelting of ice and its environmental consequences. *Rep. Prog. Phys.*, 58:115–167, 1995.

[85] J. G. Dash, A. W. Rempel, and J. S. Wettlaufer. The physics of premelted ice and its geophysical consequences. *Rev. Mod. Phys.*, 78:695–741, 2006.

[86] S. Davis. *Theory of solidification.* Cambridge University Press, Cambridge, U. K., 2001.

[87] B. Chalmers. *Principles of solidification.* John Wiley & Sons, Inc., New York, 1964.

[88] Y. H. Mori. Estimating the thickness of hydrate films from their lateral growth rates: application of a simplified heat transfer model. *J. Cryst. Growth*, 223:206–212, 2001.

[89] A. Zaccone, H. Wu, D. Gentili, and M. Morbidelli. Theory of activated-rate processes under shear with application to shear-induced aggregation of colloids. *Phys. Rev. E*, 80:051404–1–051404–8, 2009.

[90] J. Guery, E. Bertrand, C. Rouzeau, P. Levitz, D. A. Weitz, and J. Bibette. Irreversible shear-activated aggregation in non-Brownian suspensions. *Phys. Rev. Lett.*, 96:198301–1–198301–4, 2006.

[91] P. U. Karanjkar, J. W. Lee, and J. F. Morris. Surfactant effects on hydrate crystallization at the water-oil interface: hollow-conical crystals. *Cryst. Growth Des.*, 12:3817–3824, 2012.

[92] J. P. K. Seville, C. D. Willett, and P. C. Knight. Interparticle forces in fluidisation: a review. *Powder Technol.*, 113:261–268, 2000.

[93] E. Koos, J. Johannsmeier, L. Schwebler, and N. Willenbacher. Tuning suspension rheology using capillary forces. *Soft Matter*, 8:6620–6628, 2012.

[94] W. Wolthers, D. van den Ende, M. H. G. Duits, and J. Mellema. The viscosity and sedimentation of aggregating colloidal dispersions in a Couette flow. *J. Rheol.*, 40:55–67, 1996.

[95] J. McCulfor, P. Himes, and M. R. Anklam. The effects of capillary forces on the flow properties of glass particle suspensions in mineral oil. *AIChE J.*, 57:2334–2340, 2011.

[96] H. See, H. Tamura, and M. Doi. The role of water capillary forces in electrorheological fluids. *J. Phys. D: Appl. Phys.*, 26:746–752, 1993.

[97] R. B. Bird, W. E. Stewart, and E. N. Lightfoot. *Transport Phenomena.* John Wiley & Sons, Inc., revised 2nd edition, 2007.

[98] Z. B. Peng, E. Doroodchi, B. Moghtaderi, and G. M. Evans. A DEM-based analysis of the influence of aggregate structure on suspension shear yield stress. *Adv. Powder Technol.*, 23:437–444, 2012.

[99] R. J. Flatt and P. Bowen. Yodel: a yield stress model for suspensions. *J. Am. Ceram. Soc.*, 89:1244–1256, 2006.

[100] E. Koos and N. Willenbacher. Capillary forces in suspension rheology. *Science*, 331:897–900, 2011.

[101] G. Zylyftari, A. Ahuja, and J. F. Morris. Nucleation of cyclopentane hydrate by ice studied by morphology and rheology. *Chem. Eng. Sci.*, 116:497–507, 2014.

[102] D. Kashchiev and A. Firoozabadi. Driving force for crystallization of gas hydrates. *J. Cryst. Growth*, 241:220–230, 2002.

[103] D. Kashchiev and A. Firoozabadi. Nucleation of gas hydrates. *J. Cryst. Growth*, 243:476–489, 2002.

[104] D. Kashchiev and A. Firoozabadi. Induction time in crystallization of gas hydrates. *J. Cryst. Growth*, 250:449–515, 2003.

[105] D. Kashchiev and G. M. van Rosmalen. Review: Nucleation in solutions revisited. *Cryst. Res. Technol.*, 7–8:555–574, 2003.

[106] L. C. Jacobson, W. Hujo, and V. Molinero. Nucleation pathways of clathrate hydrates: effect of guest size and solubility. *J. Phys. Chem. B*, 114:13796–13807, 2010.

[107] L. C. Jacobson, W. Hujo, and V. Molinero. Amorphous precursors in the nucleation of clathrate hydrates. *J. Am. Chem. Soc.*, 132:11806–11811, 2010.

[108] K. Saito, M. Kishimoto, R. Tanaka, and R. Ohmura. Crystal growth of clathrate hydrate at the interface between hydrocarbon gas mixture and liquid water. *Cryst. Growth Des.*, 11:295–301, 2011.

[109] E. M. Freer, M. S. Selim, and E. D. Sloan. Methane hydrate film growth kinetics. *Fluid Phase Equilib.*, 185:65–75, 2001.

[110] B. Z. Peng, A. Dandekar, C. Y. Sun, H. Luo, Q. L. Ma, W. X. Pang, and G. J. Chen. Hydrate film growth on the surface of a gas bubble suspended in water. *J. Phys. Chem. B*, 111:12485–12493, 2007.

[111] C. J. Taylor, K. T. Miller, C. A. Koh, and E. D. Sloan. Macroscopic investigation of hydrate film growth at the hydrocarbon/water interface. *Chem. Eng. Sci.*, 62:6524–6533, 2007.

[112] K. Saito, A. K. Sum, and R. Ohmura. Correlation of hydrate-film growth rate at the guest/liquid-water inteface to mass transfer resistance. *Ind. Eng. Chem. Res.*, 49:7102–7103, 2010.

[113] J. W. Mullin. *Crystallization.* Butterworth-Heinemann, Oxford, 2001.

[114] S. Takeya, A. Hori, T. Hondoh, and T. Uchida. Freezing-memory effect of water on nucleation of CO_2 hydrate crystals. *J. Phys. Chem. B*, 104:4164–4168, 2000.

[115] C. Moon, P. C. Taylor, and P. M. Rodger. Molecular dynamics study of gas hydrate formation. *J. Am. Chem. Soc.*, 125:4706–4707, 2003.

[116] P. W. Wilson, D. Lester, and A. D. J. Haymet. Heterogeneous nucleation of clathrates from supercooled tetrahydrofuran (THF)/water mixtures, and the effect of an added catalyst. *Chem. Eng. Sci.*, 60:2937–2941, 2005.

[117] N. Maeda, D. Wells, N. C. Becker, P. G. Hartley, P. W. Wilson, A. D. J. Haymet, and K. A. Kozielski. Development of a high pressure automated lag time apparatus for experimental studies and statistical analyses of nucleation and growth of gas hydrates. *Rev. Sci. Instrum.*, 82:065109–1–065109–7, 2011.

[118] S. D. McCallum, D. E. Riestenberg, O. Y. Zatsepina, and T. J. Phelps. Effect of pressure vessel size on the formation of gas hydrates. *J. Pet. Sci. Eng.*, 56:54–64, 2007.

[119] C. Duchateau, P. Glénat, T. -E Pou, M. Hidalgo, and C. Dicharry. Hydrate precursor test method for the laboratory evaluation of kinetic hydrate inhibitors. *Energy Fuels*, 24:616–623, 2010.

[120] P. R. Bishnoi and V. Natarajan. Formation and decomposition of gas hydrates. *Fluid Phase Equilib.*, 117:168–177, 1996.

[121] A. Vysniauskas and P. R. Bishnoi. A kinetic study of methane hydrate formation. *Chem. Eng. Sci.*, 38:1061–1072, 1983.

[122] J. S. Parent and P. R. Bishnoi. Investigation into the nucleation behavior of natural gas hydrates. *Chem. Eng. Commun.*, 144:51–64, 1996.

[123] H. Sefidroodi, E. Abrahamsen, and M. A. Kelland. Investigation into the strength and source of memory effect for cyclopentane hydrate. *Chem. Eng. Sci.*, 87:133–140, 2013.

[124] P. Buchanan, A. K. Soper, H. Thompson, R. E. Westacott, J. L. Creek, G. Hobson, and C. A. Koh. Search for memory effects in methane hydrate: structure of water before hydrate formation and after hydrate decomposition. *J. Chem. Phys.*, 123:164507–1–164507–7, 2005.

[125] E. D. Sloan, S. Subramanian, P. N. Matthews, J. P. Lederhos, and A. A. Khokhar. Quantifying hydrate formation and kinetic inhibition. *Ind. Eng. Chem. Res.*, 37:3124–3132, 1998.

[126] C. Duchateau, J. -L Peytavy, P. Glénat, T. -E Pou, M. Hidalgo, and C. Dicharry. Laboratory evaluation of kinetic hydrate inhibitors: a procedure for enhancing the repeatability of test results. *Energy Fuels*, 23:962–966, 2009.

[127] P. M. Rodger. Methane hydrate melting and memory. *Ann. N. Y. Acad. Sci.*, 912:474–482, 2000.

[128] S. Gao, W. G. Chapman, and W. House. NMR and viscoscity investigation of clathrate hydrate formation and dissociation. *Ind. Eng. Chem. Res.*, 44:7373–7379, 2005.

[129] P. W. Wilson and A. D. J. Haymet. Hydrate formation and re-formation in nucleating THF/water mixtures show no evidence to support a "memory" effect. *Chem. Eng. J.*, 161:146–150, 2010.

[130] L. Jensen, K. Thomsen, and N. von Solms. Inhibition of structure I and II gas hydrates using synthetic and biological kinetic inhibitors. *Energy Fuels*, 25:17–23, 2011.

[131] E. G. Dirdal, C. Arulanantham, H. Sefidroodi, and M. A. Kelland. Can cyclopentane hydrate formation be used to rank the performance of kinetic hydrate inhibitors? *Chem. Eng. Sci.*, 82:177–184, 2012.

[132] X. Yingming, G. Kaihua, L. Deqing, F. Shuanshi, G. Jianming, and C. Jinggui. Gas hydrates fast nucleation from melting ice and quiescent growth along vertical heat transfer tube. *Sci. China, Ser. B: Chem.*, 48:75–82, 2005.

[133] E. D. Sloan and F. Fleyfel. A molecular mechanism for gas hydrate nucleation from ice. *AIChE J.*, 37:1281–1292, 1991.

[134] R. Radhakrishnan and B. L. Trout. A new approach for studying nucleation phenomena using molecular simulations: application to CO_2 hydrate clathrates. *J. Chem. Phys.*, 117:1786–1796, 2002.

[135] B. C. Knott, V. Molinero, M. F. Doherty, and B. Peters. Homogeneous nucleation of methane hydrate: unrealistic under realistic conditions. *J. Am. Chem. Soc.*, 134:19544–19547, 2012.

[136] H. K. Abay and T. M. Svartaas. Multicomponent gas hydrate nucleation: the effect of the cooling rate and composition. *Energy Fuels*, 25:42–51, 2011.

[137] G. N. Werezak. Aqueous solution concentration by a clathrate type of gas hydrate formation. *Chem. Eng. Prog. Symp. Ser.*, 65:6–18, 1969.

[138] Y. F. Makogon, I. V. Melikhov, E. D. Kozlovskaya, and V. F. Bozhelov'nov. Secondary nucleation in the formation of methane crystal hydrate. *Russ. J. Phys. Chem. A*, 81:1645–1649, 2007.

[139] J. M. Herri, J. S. Pic, F. Gruy, and M. Cournil. Methane hydrate crystallization mechanism from in-situ particle sizing. *AIChE J.*, 45:590–602, 1999.

[140] P. Pirzadeh and P. G. Kusalik. Molecular insights into clathrate hydrate nucleation at an ice-solution interface. *J. Am. Chem. Soc.*, 135:7278–7287, 2013.

[141] P. Pirzadeh and P. G. Kusalik. On understanding stacking fault formation in ice. *J. Am. Chem. Soc.*, 133:704–707, 2011.

[142] A. Mączyński, B. Wiśniewska-Gocłowska, and M. Góral. Recommended liquid-liquid equilibrium data. Part 1. Binary alkane-water systems. *J. Phys. Chem. Ref. Data*, 33:549–577, 2004.

[143] A. Chapoy, H. Haghighi, and B. Tohidi. Development of a Henry's constant correlation and solubility measurements of n-pentane, i-pentane, cyclopentane, n-hexane, and toluene in water. *J. Chem. Thermodyn.*, 40:1030–1037, 2008.

[144] Y. Mikami, Y. Liang, T. Matsuoka, and E. S. Boek. Molecular dynamics simulations of asphaltenes at the oil-water interface: from nanoaggregation to thin-film formation. *Energy Fuels*, 27:1838–1845, 2013.

[145] J. Xu, Y. Zhang, H. Chen, P. Wang, Z. Xie, Y. Yao, Y. Yan, and J. Zhang. Effect of surfactant headgroups on the oil/water interface: an interfacial tension measurement and simulation study. *J. Mol. Struct.*, 1052:50–56, 2013.

[146] R. J. K. U. Ranatunga, C. T. Nguyen, B. A. Wilson, W. Shinoda, and S. O. Nielsen. Molecular dynamics study of nanoparticles and non-ionic surfactant at an oil-water interface. *Soft Matter*, 7:6942–6952, 2011.

[147] O. S. Subbotin, V. R. Belosludov, T. Ikeshoji, E. N. Brodskaya, E. M. Piotrovskaya, V. Sizov, R. V. Belosludov, and Y. Kawazoe. Modeling the self-preservation effect in gas hydrate/ice systems. *Mater. Trans.*, 48:2114–2118, 2007.

[148] C. Lo, J. S. Zhang, P. Somasundaran, S. Lu, A. Couzis, and J. W. Lee. Adsorption of surfactants on two different hydrates. *Langmuir*, 24:12723–12726, 2008.

[149] O. Salako, C. Lo, J. S. Zhang, A. Couzis, P. Somasundaran, and J. W. Lee. Adsorption of sodium dodecyl sulfate onto clathrate hydrates in the presence of salt. *J. Colloid Interface Sci.*, 386:333–337, 2012.

[150] W. L. Ryan and E. A. Hemmingsen. Bubble formation at porous hydrophobic surfaces. *J. Colloid Interface Sci.*, 197:101–107, 1998.

[151] W. L. Ryan and E. A. Hemmingsen. Bubble formation in water at smooth hydrophobic surfaces. *J. Colloid Interface Sci.*, 157:312–317, 1993.

[152] E. B. Webb, P. J. Rensing, C. A. Koh, E. D. Sloan, A. K. Sum, and M. W. Liberatore. High pressure rheometer for in situ formation and characterization of methane hydrates. *Rev. Sci. Instrum.*, 83:015106–1–015106–6, 2012.

[153] E. B. Webb, C. A. Koh, and M. W. Liberatore. Rheological properties of methane hydrate slurries formed from AOT + water + oil microemulsions. *Langmuir*, 29:10997–11004, 2013.

[154] E. B. Webb, C. A. Koh, and M. W. Liberatore. High pressure rheology of hydrate slurries formed from water-in-mineral oil emulsions. *Ind. Eng. Chem. Res.*, 53:6998–7007, 2014.

[155] R. B. Schüller, M. Tande, and Harald-Knut Kvandal. Rheological hydrate detection and characterization. *Ann. T. Nord. Rheol. Soc.*, 13:83–90, 2005.

[156] J. G. Delgado-Linares, A. A. A. Majid, E. D. Sloan, C. A. Koh, and A. K. Sum. Model water-in-oil emulsions for gas hydrate studies in oil continuous systems. *Energy Fuels*, 27:4564–4573, 2013.

[157] A. W. Saak, H. M. Jennings, and S. P. Shah. The influence of wall slip on yield stress and viscoelastic measurements of cement paste. *Cem. Concr. Res.*, 31:205–212, 2001.

[158] H. J. Walls, S. B. Caines, A. M. Sanchez, and S. A. Khan. Yield stress and wall slip phenomena in colloidal silica gels. *J. Rheol.*, 47:847–868, 2003.

[159] C. F. Chan Man Fong and D. De Kee. Yield stress and small amplitude oscillatory flow in transient networks. *Ind. Eng. Chem. Res.*, 33:2374–2376, 1994.

[160] D. J. Turner, K. T. Miller, and E. D. Sloan. Methane hydrate formation and an inward growing shell model in water-in-oil dispersion. *Chem. Eng. Sci.*, 64:3996–4004, 2009.